Fast Ewald Summation based on NFFT with Mixed Periodicity

Franziska Nestler, Michael Pippig and Daniel Potts

In this paper we develop new fast Fourier-based methods for the Coulomb problem. We combine the Ewald summation formulas and the fast summation approach based on the nonequispaced fast Fourier transform (NFFT) in order to develop efficient methods for calculating the Coulomb energies as well as the acting forces in charged particle systems subject to mixed periodic boundary conditions. Therewith, we extend the applicability of NFFT based methods, which already exist for open as well as for 3d-periodic boundary conditions, to arbitrary combinations of periodic and open boundary conditions. We reconsider the derivation of the Ewald formulas for 2d- and 1d-periodic systems, introduce the new algorithms and present high precision numerical results.

Key words and phrases : Ewald method, nonequispaced fast Fourier transform, particle methods, mixed periodicity, NFFT, FMM, P3M, P2NFFT, ScaFaCoS

2000 AMS Mathematics Subject Classification : 65T

1. Introduction

Let N charges $q_j \in \mathbb{R}$ at positions $\boldsymbol{x}_j \in \mathbb{R}^3$, $j = 1, \ldots, N$, be given, fulfilling the charge neutrality condition

$$\sum_{j=1}^{N} q_j = 0\,. \tag{1.1}$$

The total Coulomb energy of the particle system is basically a sum of the form

$$U_{\mathcal{S}} := \frac{1}{2} \sum_{j=1}^{N} q_j \phi_{\mathcal{S}}(\boldsymbol{x}_j), \tag{1.2}$$

franziska.nestler@mathematik.tu-chemnitz.de,
michael.pippig@mathematik.tu-chemnitz.de,
potts@mathematik.tu-chemnitz.de,
Technische Universität Chemnitz, Faculty of Mathematics, 09107 Chemnitz, Germany

where for each particle j the potential $\phi_{\mathcal{S}}(\boldsymbol{x}_j)$ is given by

$$\phi_{\mathcal{S}}(\boldsymbol{x}_j) := \sum_{\boldsymbol{n}\in\mathcal{S}} \sum_{i=1}^{N}{}' \frac{q_i}{\|\boldsymbol{x}_{ij} + L\boldsymbol{n}\|}. \tag{1.3}$$

Thereby, we denote by $\|\cdot\|$ the Euclidean norm and define the difference vectors $\boldsymbol{x}_{ij} := \boldsymbol{x}_i - \boldsymbol{x}_j$. The set of translation vectors $\mathcal{S} \subseteq \mathbb{Z}^3$ is defined according to the given boundary conditions and $L \in \mathbb{R}_+$ is the edge length of the simulation box in each dimension subject to periodic boundary conditions. The prime on the double sum indicates that for $\boldsymbol{n} = \boldsymbol{0}$ all terms with $i = j$ are omitted. For convenience we skipped the prefactor $\frac{1}{4\pi\varepsilon_0}$ which corresponds to Gaussian units. It is important to note that the sum (1.3) is, assuming charge neutrality (1.1), only conditionally convergent, i.e., the values of the potentials $\phi_{\mathcal{S}}(\boldsymbol{x}_j)$ depend on the order of summation. The energies of the single particles are defined by

$$U_{\mathcal{S}}(\boldsymbol{x}_j) := q_j \phi_{\mathcal{S}}(\boldsymbol{x}_j)$$

and are sometimes also taken into consideration. In addition to the calculation of the potentials $\phi_{\mathcal{S}}(\boldsymbol{x}_j)$ and the total energy $U_{\mathcal{S}}$ of the system, we are also interested in evaluating the forces acting on the particles, which are given by

$$\boldsymbol{F}_{\mathcal{S}}(\boldsymbol{x}_j) := q_j \boldsymbol{E}_{\mathcal{S}}(\boldsymbol{x}_j), \quad \text{with the fields} \quad \boldsymbol{E}_{\mathcal{S}}(\boldsymbol{x}_j) := -\nabla\phi_{\mathcal{S}}(\boldsymbol{x}_j). \tag{1.4}$$

The well known Ewald summation technique [19], which was originally developed for 3d-periodic systems, where we set $\mathcal{S} := \mathbb{Z}^3$ in our notation, is the main basis for a variety of fast algorithms for the evaluation of (1.2) under 3d-periodic boundary conditions, see [34, 14, 13, 18, 25]. The Ewald summation method [19] makes use of the trivial identity

$$\frac{1}{r} = \frac{\operatorname{erf}(\alpha r)}{r} + \frac{\operatorname{erfc}(\alpha r)}{r}, \tag{1.5}$$

where $\alpha > 0$ is generally known as the splitting parameter, $\operatorname{erf}(x) := \frac{2}{\sqrt{\pi}} \int_0^x \mathrm{e}^{-t^2} \mathrm{d}t$ is the well known error function and $\operatorname{erfc}(x) := 1 - \operatorname{erf}(x)$ is the complementary error function. If (1.5) is applied in (1.3) the potential $\phi_{\mathcal{S}}(\boldsymbol{x}_j)$ is split into two rapidly converging parts. Thereby, the erf-terms have the finite limit

$$\lim_{r\to 0} \frac{\operatorname{erf}(\alpha r)}{r} = \frac{2\alpha}{\sqrt{\pi}}, \tag{1.6}$$

so that this part can be transformed into a sum in Fourier space, which allows the application of fast Fourier methods in order to derive efficient algorithms. The second part, containing the complementary error function, is absolutely convergent and can be calculated by a direct summation after truncating the infinite sum.

We describe 2d-periodic boundary conditions by choosing $\mathcal{S} := \mathbb{Z}^2 \times \{0\}$ with $\boldsymbol{x}_j \in L\mathbb{T}^2 \times \mathbb{R}$ and 1d-periodic constraints by choosing $\mathcal{S} := \mathbb{Z} \times \{0\}^2$ with $\boldsymbol{x}_j \in L\mathbb{T} \times \mathbb{R}^2$. Thereby, we denote the torus $\mathbb{T}$ by $\mathbb{T} := \mathbb{R}/\mathbb{Z} \simeq [-1/2, 1/2)$. For a graphical illustration see Figure 1.1.

The Ewald formulas for 2d-periodic as well as for 1d-periodic geometries were already proposed in [23] and [43], respectively, and form the basis of the algorithms proposed in this paper. In contrast to the case of 3d-periodic boundary conditions, the application of the Ewald formulas for mixed periodic systems does not straightforwardly lead to fast algorithms.

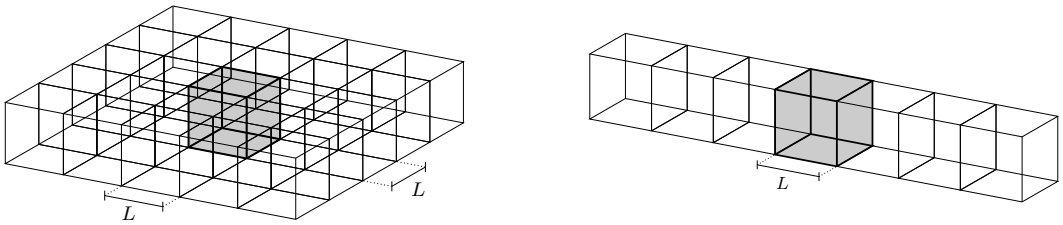

Figure 1.1: The simulation box is duplicated along two of three dimensions in the 2d-periodic case (left) and along one dimension in the 1d-periodic setting (right).

Some Fourier based algorithms, like MMM2D, MMM1D or ELC, see [6, 8, 7] and the fast and spectrally accurate Ewald summation in slab geometry [35], already exist, see also [51, 52, 11, 10] for algorithms with higher complexity.

We will later refer again to [35], which is the latest development for the 2d-periodic case, in order to discuss the differences to our method, see Section 4.1. Another approach for long range interactions on surfaces is proposed in [37]. The decrease of the underlying Fourier coefficients is rather slow, which may lead to a computational overhead. The same idea has also been discussed for the 1d-periodic case, see [36], see also Section 4.1 for the exact relation to our approach.

For open boundary conditions, i.e., $\mathcal{S} := \{0\}^3$ in (1.3), fast Fourier based methods [44, 45] were suggested, too. The relation of the Fourier based algorithms for open and 3d-periodic boundary conditions were already investigated in [41]. The proposed algorithms are very similar, where Fourier coefficients are computed from the continuous transform in the 3d-periodic case and from a discrete Fourier transform for open boundary conditions. In this paper we aim to close the gap and propose FFT based algorithms also for 2d- and 1d-periodic boundary conditions, i.e., we propose a method, such that the long range part can be evaluated by only one 3d-FFT, respectively 3d-NFFT, without further arithmetical cost. This approach was already proposed in the short paper [39]. In this paper we also present numerical results, show that the performance of the new algorithms is similar to the 3d-periodic case and go into detail about our implementation. Furthermore, we derive the Ewald formulas for 2d- and 1d-periodic systems, see Theorem 4.1 and Theorem 5.1, respectively. Thereby, we always start with the splitting (1.5) and then use the technique of convergence factors to derive the Fourier space representation of the long range part by applying the Poisson summation formula. We show that the obtained formulas can be used in order to derive the related algorithms, see Algorithm 4.3 and Algorithm 5.4. The main advantage of our approach is that the new algorithms are completely of the same structure as the well known algorithms for 3d-periodic and open boundary conditions, see [41]. That is that the short range parts of the potentials are computed directly and the long range parts are computed by an adjoint NFFT, followed by a multiplication in Fourier domain and again an NFFT in three dimensions, see Remark 4.4 and Remark 5.5.

The accuracy in molecular dynamics simulations is commonly measured in terms of root mean square (rms) errors. In general, the rms error in the forces is considered. We define the

rms force error by

$$\Delta F_{\mathcal{S}} := \left(\frac{1}{N} \sum_{j=1}^{N} \left\| \boldsymbol{F}_{\mathcal{S}}(\boldsymbol{x}_j) - \tilde{\boldsymbol{F}}_{\mathcal{S}}(\boldsymbol{x}_j) \right\|^2 \right)^{1/2}, \tag{1.7}$$

where $\tilde{\boldsymbol{F}}_{\mathcal{S}}(\boldsymbol{x}_j)$ is some approximation of the force $\boldsymbol{F}_{\mathcal{S}}(\boldsymbol{x}_j)$, as defined in (1.4). In this paper, we also use the rms energy error, which is analogously given by

$$\Delta U_{\mathcal{S}} := \left(\frac{1}{N} \sum_{j=1}^{N} \left| U_{\mathcal{S}}(\boldsymbol{x}_j) - \tilde{U}_{\mathcal{S}}(\boldsymbol{x}_j) \right|^2 \right)^{1/2}. \tag{1.8}$$

We remark that the fast multipole method can also handle all mentioned types of boundary conditions very efficiently, see [31]. In order to estimate the rms errors in our numerical tests we used reference data computed with an implementation [1] of the fast multipole method [28, 27] that allows mixed periodic constraints.

The outline of this paper is as follows. We start with a short introduction to the nonequispaced fast Fourier transform (NFFT) in Section 2 and review the idea of fast Ewald summation based on NFFTs for 3d-periodic systems in Section 3. In Section 4 we consider the case of periodic boundary conditions in two of three dimensions. To this end, we introduce (see Subsection 4.1) and prove (see Appendix A) the 2d-Ewald formulas and develop a new fast algorithm in Subsection 4.2. Furthermore, we present numerical results in Subsection 4.3, which show its efficiency. In order to rate the very good performance of the new algorithm, we compare the method to the particle-particle NFFT (P^2NFFT) method for 3d-periodic systems [42] as well as to the method proposed in [35] by considering similar numerical examples. Note that the P^2NFFT algorithm is highly optimized and recently compared with other methods, such as the particle-particle particle-mesh (P^3M) method, the fast multipole method or multigrid based methods, see [5]. The 1d-periodic case is considered in an analog manner in Section 5. We present the 1d-Ewald formulas, see Subsection 5.1, develop a new fast algorithm in Subsection 5.2 and present numerical results in Subsection 5.3. Finally, we conclude with a short summary.

2. Prerequisite and NFFT

A broad variety of mathematical algorithms and applications depend on the calculation of the nonequispaced discrete Fourier transform, which is a generalization of the discrete Fourier transform to nonequispaced nodes. Especially, its fast approximate realization called nonequispaced fast Fourier transform (NFFT) [17, 9, 48, 50, 46, 22, 29] led to the development of a large number of fast numerical algorithms. In this section we introduce the main notation and give a short introduction to the NFFT in three variables. To keep the notation short we define for some $\boldsymbol{M} = (M_1, \ldots, M_d) \in 2\mathbb{N}^d$ the index set $\mathcal{I}_{\boldsymbol{M}}$ by

$$\mathcal{I}_{\boldsymbol{M}} := \bigotimes_{j=1}^{d} \mathcal{I}_{M_j}, \text{ where } \mathcal{I}_{M_j} := \left\{ -\tfrac{M_j}{2}, \ldots, \tfrac{M_j}{2} - 1 \right\},$$

and the cardinality by $|\mathcal{I}_{\boldsymbol{M}}| := \prod_{j=1}^{d} M_j$. We do not distinguish between row and column vectors and denote by $\boldsymbol{x} \cdot \boldsymbol{y} := x_1 y_1 + x_2 y_2 + x_3 y_3$ the scalar product and by $\boldsymbol{x} \odot \boldsymbol{y} :=$

$(x_1y_1, x_2y_2, x_3y_3) \in \mathbb{R}^3$ the component wise product of two vectors $\boldsymbol{x}, \boldsymbol{y} \in \mathbb{R}^3$. For some $\boldsymbol{x} \in \mathbb{R}^3$ with non-vanishing components we further define the vector $\boldsymbol{x}^{-1} := (x_1^{-1}, x_2^{-1}, x_3^{-1}) \in \mathbb{R}^3$.

Let a trigonometric polynomial $f\colon \mathbb{T}^3 \to \mathbb{C}$ be given by

$$f(\boldsymbol{x}) = \sum_{\boldsymbol{k} \in \mathcal{I}_{\boldsymbol{M}}} \hat{f}_{\boldsymbol{k}} \mathrm{e}^{-2\pi \mathrm{i} \boldsymbol{k} \cdot \boldsymbol{x}}, \tag{2.1}$$

with the Fourier coefficients $\hat{f}_{\boldsymbol{k}} \in \mathbb{C}$, $\boldsymbol{k} \in \mathcal{I}_{\boldsymbol{M}}$. The fast evaluation of f at arbitrarily chosen nodes $\boldsymbol{x}_j \in \mathbb{T}^3$, $j = 1, \ldots, N \in \mathbb{N}$, i.e., the efficient computation of

$$f_j := f(\boldsymbol{x}_j) = \sum_{\boldsymbol{k} \in \mathcal{I}_{\boldsymbol{M}}} \hat{f}_{\boldsymbol{k}} \mathrm{e}^{-2\pi \mathrm{i} \boldsymbol{k} \cdot \boldsymbol{x}_j}, \quad j = 1, \ldots, N, \tag{2.2}$$

is known as three-dimensional NFFT. We take the approach from [44] and approximate the trigonometric polynomial f by a sum of translates of a one-periodic function $\tilde{\varphi}$, which is defined via a tensor product of the periodization of a univariate window function φ, i.e., we set $\tilde{\varphi}_1(x) := \sum_{j=-\infty}^{\infty} \varphi(x+j)$ and define the trivariate function $\tilde{\varphi}$ by $\tilde{\varphi}(\boldsymbol{x}) := \tilde{\varphi}_1(x_1) \cdot \tilde{\varphi}_1(x_2) \cdot \tilde{\varphi}_1(x_3)$. We obtain

$$f(\boldsymbol{x}) \approx \sum_{\boldsymbol{l} \in \mathcal{I}_{\boldsymbol{m}}} g_{\boldsymbol{l}} \tilde{\varphi}(\boldsymbol{x} - \boldsymbol{l} \odot \boldsymbol{m}^{-1}), \tag{2.3}$$

where we choose $\boldsymbol{M} \leq \boldsymbol{m} \in 2\mathbb{N}^3$ (component wise) and denote by $\boldsymbol{m} \odot \boldsymbol{M}^{-1}$ the vector valued oversampling factor. Furthermore, the function $\tilde{\varphi}$ is assumed to be well localized in spatial and frequency domain. Under these assumptions, it can be shown that

$$g_{\boldsymbol{l}} := \frac{1}{|\mathcal{I}_{\boldsymbol{m}}|} \sum_{\boldsymbol{k} \in \mathcal{I}_{\boldsymbol{M}}} \frac{\hat{f}_{\boldsymbol{k}}}{c_{\boldsymbol{k}}(\tilde{\varphi})} \mathrm{e}^{2\pi \mathrm{i} \boldsymbol{k} \cdot (\boldsymbol{l} \odot \boldsymbol{m}^{-1})}$$

is a reasonable choice of the unknown coefficients $g_{\boldsymbol{l}}$ in (2.3), where $c_{\boldsymbol{k}}(\tilde{\varphi})$ denotes the $\boldsymbol{k}$-th Fourier coefficient of $\tilde{\varphi}$. After calculating the coefficients $g_{\boldsymbol{l}}$ by an FFT the function values f_j are computed via (2.3), where the sums are short due to the good localization of $\tilde{\varphi}$ in spatial domain. The adjoint nonequispaced fast Fourier transform ($\mathrm{NFFT}^{\mathrm{H}}$) is an algorithm for the fast evaluation of

$$\hat{h}_{\boldsymbol{k}} = \sum_{j=1}^{N} f_j \mathrm{e}^{2\pi \mathrm{i} \boldsymbol{k} \cdot \boldsymbol{x}_j}, \qquad \boldsymbol{k} \in \mathcal{I}_{\boldsymbol{M}}, \tag{2.4}$$

where now the coefficients $f_j \in \mathbb{C}$ are given. Both algorithms have very similar structures and can be performed in $\mathcal{O}(|\mathcal{I}_{\boldsymbol{M}}| \log |\mathcal{I}_{\boldsymbol{M}}| + N)$ arithmetic operations, see [46, 29]. Thereby, the prefactors depend on the required accuracy as well as the properties of the window function. For many possible window functions error bounds in the ∞–norm have already been derived, see [44, 48] for instance.

3. Fast Ewald summation for 3d–periodic boundary conditions

For an electrical neutral system of N charges q_j distributed in a cubic box of edge length L we define the electrostatic potential subject to 3d–periodic boundary conditions by

$$\phi^{\mathrm{p3}}(\boldsymbol{x}_j) := \phi_{\mathbb{Z}^3}(\boldsymbol{x}_j) = \sum_{s=0}^{\infty} \sum_{\substack{\boldsymbol{n} \in \mathbb{Z}^3 \\ \|\boldsymbol{n}\|^2 = s}} {\sum_{i=1}^{N}}' \frac{q_i}{\|\boldsymbol{x}_{ij} + L\boldsymbol{n}\|}, \tag{3.1}$$

i.e., we set $\mathcal{S} := \mathbb{Z}^3$ within the definitions (1.2) – (1.4) and apply a spherical order of summation. We obtain [19, 32]

$$\phi^{\mathrm{p3}}(\boldsymbol{x}_j) = \phi^{\mathrm{p3,S}}(\boldsymbol{x}_j) + \phi^{\mathrm{p3,L}}(\boldsymbol{x}_j) + \phi^{\mathrm{p3,self}}(\boldsymbol{x}_j), \tag{3.2}$$

where for the splitting parameter $\alpha > 0$ we define the short range part

$$\phi^{\mathrm{p3,S}}(\boldsymbol{x}_j) := \sum_{\boldsymbol{n}\in\mathbb{Z}^3} {\sum_{i=1}^{N}}' q_i \frac{\operatorname{erfc}(\alpha\|\boldsymbol{x}_{ij} + L\boldsymbol{n}\|)}{\|\boldsymbol{x}_{ij} + L\boldsymbol{n}\|}, \tag{3.3}$$

the long range part

$$\phi^{\mathrm{p3,L}}(\boldsymbol{x}_j) := \frac{1}{\pi L} \sum_{\boldsymbol{k}\in\mathbb{Z}^3\setminus\{\boldsymbol{0}\}} \frac{\mathrm{e}^{-\pi^2\|\boldsymbol{k}\|^2/(\alpha^2L^2)}}{\|\boldsymbol{k}\|^2} \left(\sum_{i=1}^{N} q_i \mathrm{e}^{2\pi\mathrm{i}\boldsymbol{k}\cdot\boldsymbol{x}_i/L} \right) \mathrm{e}^{-2\pi\mathrm{i}\boldsymbol{k}\cdot\boldsymbol{x}_j/L}, \tag{3.4}$$

and the self potential

$$\phi^{\mathrm{p3,self}}(\boldsymbol{x}_j) := -\frac{2\alpha}{\sqrt{\pi}} q_j.$$

Often a fourth term, the so called dipole correction term, appears in the decomposition (3.2), cf. [14]. The dipole correction term is the only part depending on the order of summation. However, if a spherical summation order is applied, the dipole correction term depends only on the norm of the dipole moment $\sum_{j=1}^{N} q_j\boldsymbol{x}_j$ and, additionally, on the dielectric constant of the surrounding medium. Therefore, it can be computed efficiently in $\mathcal{O}(N)$ arithmetic operations. If the medium is assumed to be metallic, the dipole term vanishes and (3.2) applies. It should be mentioned that the formulas above can be generalized to non-cubic boxes and also non-orthogonal (triclinic) boxes, cf. [19, 13, 26].

As the complementary error function erfc rapidly tends to zero, the short range part of each potential $\phi^{\mathrm{p3,S}}(\boldsymbol{x}_j)$ can be obtained by direct evaluation, i.e., all distances $\|\boldsymbol{x}_{ij} + L\boldsymbol{n}\|$ larger than an appropriate cutoff radius r_{cut} are ignored. If we assume a sufficiently homogenous particle distribution, each particle only interacts with a fixed number of neighbors. Thus, the real space sum can be computed with a linked cell algorithm [21] in $\mathcal{O}(N)$ arithmetic operations for this case. In the case of a very heterogenous particle distribution, a combination with the FMM as pointed out in [16] is possible.

In order to compute the long range parts $\phi^{\mathrm{p3,L}}(\boldsymbol{x}_j)$ we truncate the infinite sum and compute approximations of the sums

$$\hat{S}(\boldsymbol{k}) := \sum_{i=1}^{N} q_i \mathrm{e}^{2\pi\mathrm{i}\boldsymbol{k}\cdot\boldsymbol{x}_i/L}, \quad \boldsymbol{k} \in \mathcal{I}_{\boldsymbol{M}},$$

with an adjoint NFFT and evaluate

$$\phi^{\mathrm{p3,L}}(\boldsymbol{x}_j) \approx \sum_{\boldsymbol{k}\in\mathcal{I}_{\boldsymbol{M}}\setminus\{\boldsymbol{0}\}} \hat{b}_{\boldsymbol{k}} \hat{S}(\boldsymbol{k}) \mathrm{e}^{-2\pi\mathrm{i}\boldsymbol{k}\cdot\boldsymbol{x}_j/L}, \quad j = 1, \ldots, N,$$

where we define the Fourier coefficients

$$\hat{b}_{\boldsymbol{k}} := \frac{1}{\pi L} \frac{\mathrm{e}^{-\pi^2\|\boldsymbol{k}\|^2/(\alpha^2L^2)}}{\|\boldsymbol{k}\|^2}, \tag{3.5}$$

via the NFFT. In matrix vector notation we may write

$$\left(\phi^{\mathrm{p3,L}}(\boldsymbol{x}_j)\right)_{j=1}^{N} \approx \mathcal{A}\mathcal{D}\mathcal{A}^{\mathrm{H}}\boldsymbol{q}, \tag{3.6}$$

where $\mathcal{A}$ denotes the matrix representation of the NFFT in three dimensions, $\mathcal{D}$ is a diagonal matrix with entries $\hat{b}_{\boldsymbol{k}}$, $\boldsymbol{k} \in \mathcal{I}_{\boldsymbol{M}}$, and $\boldsymbol{q} = (q_1, \ldots, q_N)^{\top} \in \mathbb{R}^N$.

The force acting on a particle j can be written as

$$\boldsymbol{F}^{\mathrm{p3}}(\boldsymbol{x}_j) = \boldsymbol{F}^{\mathrm{p3,S}}(\boldsymbol{x}_j) + \boldsymbol{F}^{\mathrm{p3,L}}(\boldsymbol{x}_j) := -q_j \nabla \phi^{\mathrm{p3,S}}(\boldsymbol{x}_j) - q_j \nabla \phi^{\mathrm{p3,L}}(\boldsymbol{x}_j),$$

where the short range part $\boldsymbol{F}^{\mathrm{p3,S}}(\boldsymbol{x}_j)$ is given by

$$\boldsymbol{F}^{\mathrm{S}}_{\mathcal{S}}(\boldsymbol{x}_j) := -q_j \sum_{\boldsymbol{n}\in\mathcal{S}} {\sum_{i=1}^{N}}' q_i \left(\frac{2\alpha}{\sqrt{\pi}} \mathrm{e}^{-\alpha^2 \|\boldsymbol{x}_{ij}+L\boldsymbol{n}\|^2} + \frac{\operatorname{erfc}(\alpha\|\boldsymbol{x}_{ij}+L\boldsymbol{n}\|)}{\|\boldsymbol{x}_{ij}+L\boldsymbol{n}\|} \right) \frac{\boldsymbol{x}_{ij}+L\boldsymbol{n}}{\|\boldsymbol{x}_{ij}+L\boldsymbol{n}\|^2} \tag{3.7}$$

with $\mathcal{S} := \mathbb{Z}^3$ and can be evaluated by direct summation, too. The long range part can be obtained by differentiation in Fourier space, i.e., we write

$$\boldsymbol{F}^{\mathrm{p3,L}}(\boldsymbol{x}_j) = \frac{2\pi \mathrm{i} q_j}{L} \sum_{\boldsymbol{k}\in\mathbb{Z}^3\setminus\{\boldsymbol{0}\}} \hat{b}_{\boldsymbol{k}} \boldsymbol{k} \hat{S}(\boldsymbol{k}) \mathrm{e}^{-2\pi \mathrm{i} \boldsymbol{k}\cdot\boldsymbol{x}_j/L} \tag{3.8}$$

and use the NFFT in each dimension for an efficient evaluation. This approach is widely known as i$\boldsymbol{k}$ differentiation, see [14] for instance. An alternative is the so called analytic differentiation approach [13], where the ∇ operator is applied to the NFFT window function. In terms of (2.1) and (2.3) this means that we set

$$\hat{f}_{\boldsymbol{k}} := \begin{cases} \hat{b}_{\boldsymbol{k}} \hat{S}(\boldsymbol{k}) & : \boldsymbol{k} \neq \boldsymbol{0}, \\ 0 & : \boldsymbol{k} = \boldsymbol{0} \end{cases}$$

and compute the long range portion of the force $\boldsymbol{F}^{\mathrm{p3}}(\boldsymbol{x}_j)$ by

$$\boldsymbol{F}^{\mathrm{p3,L}}(\boldsymbol{x}_j) \approx -q_j \sum_{\boldsymbol{l}\in\mathcal{I}_{\boldsymbol{m}}} g_{\boldsymbol{l}} \nabla \tilde{\varphi}(\boldsymbol{x}_j - \boldsymbol{l} \odot \boldsymbol{m}^{-1}). \tag{3.9}$$

4. Fast Ewald summation for 2d-periodic boundary conditions

4.1. Ewald summation

We consider a system of N charges $q_j \in \mathbb{R}$ at positions $\boldsymbol{x}_j \in L\mathbb{T}^2 \times \mathbb{R}$. Under periodic boundary conditions in the first two dimensions we define the potential of each single particle by

$$\phi^{\mathrm{p2}}(\boldsymbol{x}_j) := \phi_{\mathbb{Z}^2\times\{0\}}(\boldsymbol{x}_j) = \sum_{s=0}^{\infty} \sum_{\substack{\boldsymbol{n}\in\mathbb{Z}^2\times\{0\} \\ \|\boldsymbol{n}\|^2=s}} {\sum_{i=1}^{N}}' \frac{q_i}{\|\boldsymbol{x}_{ij}+L\boldsymbol{n}\|} \tag{4.1}$$

and define the total Coulomb energy via

$$U^{\mathrm{p2}} := U_{\mathbb{Z}^2\times\{0\}} = \frac{1}{2} \sum_{j=1}^{N} q_j \phi^{\mathrm{p2}}(\boldsymbol{x}_j), \tag{4.2}$$

i.e., we set $\mathcal{S} := \mathbb{Z}^2 \times \{0\}$ in (1.2) – (1.4) and use the spherical limit as in (3.1).

In the following theorem we consider the 2d-Ewald formula, see [23]. In Appendix A we give a proof using convergence factors, similar to [32], where the 3d-periodic case is treated. In this section we denote for $\boldsymbol{y} \in \mathbb{R}^3$ the vector of its first two components by $\tilde{\boldsymbol{y}} := (y_1, y_2) \in \mathbb{R}^2$.

Theorem 4.1. *Consider an electrical neutral system of N charges $q_j \in \mathbb{R}$ at positions $\boldsymbol{x}_j = (\tilde{\boldsymbol{x}}_j, x_{j,3}) \in L\mathbb{T}^2 \times \mathbb{R}$, $j = 1, \dots, N$. Under periodic boundary conditions in the first two variables the potentials $\phi^{\mathrm{p2}}(\boldsymbol{x}_j)$, defined in* (4.1)*, can be written in the form*

$$\phi^{\mathrm{p2}}(\boldsymbol{x}_j) = \phi^{\mathrm{p2,S}}(\boldsymbol{x}_j) + \phi^{\mathrm{p2,L}}(\boldsymbol{x}_j) + \phi^{\mathrm{p2},\mathbf{0}}(\boldsymbol{x}_j) + \phi^{\mathrm{p2,self}}(\boldsymbol{x}_j),$$

where for some $\alpha > 0$ we define the short range part

$$\phi^{\mathrm{p2,S}}(\boldsymbol{x}_j) := \sum_{\boldsymbol{n} \in \mathbb{Z}^2 \times \{0\}} {\sum_{i=1}^{N}}' q_i \frac{\operatorname{erfc}(\alpha \|\boldsymbol{x}_{ij} + L\boldsymbol{n}\|)}{\|\boldsymbol{x}_{ij} + L\boldsymbol{n}\|}, \tag{4.3}$$

the long range parts

$$\phi^{\mathrm{p2,L}}(\boldsymbol{x}_j) := \frac{1}{2L} \sum_{\boldsymbol{k} \in \mathbb{Z}^2 \setminus \{\mathbf{0}\}} \sum_{i=1}^{N} q_i \, \mathrm{e}^{2\pi i \boldsymbol{k} \cdot \tilde{\boldsymbol{x}}_{ij}/L} \cdot \Theta^{\mathrm{p2}}(\|\boldsymbol{k}\|, x_{ij,3}), \tag{4.4}$$

$$\phi^{\mathrm{p2},\mathbf{0}}(\boldsymbol{x}_j) := -\frac{2\sqrt{\pi}}{L^2} \sum_{i=1}^{N} q_i \Theta_0^{\mathrm{p2}}(x_{ij,3}), \tag{4.5}$$

the self potential

$$\phi^{\mathrm{p2,self}}(\boldsymbol{x}_j) := -\frac{2\alpha}{\sqrt{\pi}} q_j \ ,$$

and the functions $\Theta^{\mathrm{p2}}(k, r)$, $\Theta_0^{\mathrm{p2}}(r)$ for $k, r \in \mathbb{R}$ are defined by

$$\Theta^{\mathrm{p2}}(k, r) := \frac{1}{k} \left[\mathrm{e}^{2\pi k r/L} \operatorname{erfc}\left(\frac{\pi k}{\alpha L} + \alpha r \right) + \mathrm{e}^{-2\pi k r/L} \operatorname{erfc}\left(\frac{\pi k}{\alpha L} - \alpha r \right) \right], \tag{4.6}$$

$$\Theta_0^{\mathrm{p2}}(r) := \frac{\mathrm{e}^{-\alpha^2 r^2}}{\alpha} + \sqrt{\pi} r \operatorname{erf}(\alpha r).$$

Proof. See Appendix A. ∎

With the following lemma we show that the function $\Theta^{\mathrm{p2}}(k, r)$ tends to zero exponentially fast with respect to k, i.e., truncation of the infinite sum in $\phi^{\mathrm{p2,L}}(\boldsymbol{x}_j)$ is reasonable.

Lemma 4.2. *For arbitrary $r \in \mathbb{R}$ we have for the function Θ^{p2} given in* (4.6)

$$\Theta^{\mathrm{p2}}(k, r) \to 0 \text{ with } \Theta^{\mathrm{p2}}(k, r) = o(k^{-2} \mathrm{e}^{-k^2}) \text{ for } k \to \infty.$$

Proof. The function Θ^{p2} has the integral representation

$$\Theta^{\mathrm{p2}}(k, r) = \frac{4\sqrt{\pi}}{L} \int_0^{\alpha} \frac{1}{t^2} \exp\left(-\frac{\pi^2 k^2}{L^2 t^2} - r^2 t^2 \right) \mathrm{d}t, \tag{4.7}$$

as it is shown in the proof of Theorem 4.1 (Appendix A). Now, we easily see

$$\Theta^{\mathrm{p2}}(k,r) \le \Theta^{\mathrm{p2}}(k,0) = \frac{2}{k}\,\mathrm{erfc}\left(\frac{\pi k}{\alpha L}\right) \approx \frac{2\alpha L}{k^2\pi^{3/2}}\mathrm{e}^{-\frac{\pi^2k^2}{\alpha^2L^2}},$$

which is valid for large k, cf. [2, number 7.1.23]. ■

The short range part $\phi^{\mathrm{p2,S}}(\boldsymbol{x}_j)$ can be treated analogously to the 3d-periodic case. However, the efficient computation of the long range part $\phi^{\mathrm{p2,L}}(\boldsymbol{x}_j) + \phi^{\mathrm{p2},\mathbf{0}}(\boldsymbol{x}_j)$ is more intricate. In contrast to the 3d-periodic case, we do not have a Fourier space representation regarding all three dimensions. In order to obtain for each $k = \|\boldsymbol{k}\|$ a separation of $x_{i,3}$ and $x_{j,3}$ in (4.4) we want to approximate the function $\Theta^{\mathrm{p2}}(k,\cdot)$ by a finite Fourier series and then use an FFT based method. In the following, we discuss three different approaches to compute such an approximation and point out the relation to existing methods.

Variant I (Periodization): The continuous Fourier transform of the function $\Theta^{\mathrm{p2}}(k,\cdot)$ is given by

$$\hat{\Theta}^{\mathrm{p2}}(k,\xi) = \frac{2L}{\pi(k^2+L^2\xi^2)}\mathrm{e}^{-\pi^2k^2/(\alpha^2L^2)-\pi^2\xi^2/\alpha^2}. \tag{4.8}$$

This can be derived easily by applying the integral representation (4.7) or utilizing (4.22). If $\Theta^{\mathrm{p2}}(k,\cdot)$ is sufficiently small outside the simulation box, we may approximate it by its h-periodic version $\sum_{n\in\mathbb{Z}}\Theta^{\mathrm{p2}}(k,\cdot+hn)$, where $h \ge 2L$, apply the Poisson summation formula and truncate the resulting infinite sum in order to obtain an approximation of the form

$$\begin{aligned}\Theta^{\mathrm{p2}}(k,r) &\approx \sum_{n=-\infty}^{\infty}\Theta^{\mathrm{p2}}(k,r+hn) = \frac{1}{h}\sum_{l=-\infty}^{\infty}\hat{\Theta}^{\mathrm{p2}}(k,{}^{l}\!/_{h})\mathrm{e}^{2\pi\mathrm{i}lr/h}\\ &\approx \frac{1}{h}\sum_{l=-M_3/2}^{M_3/2-1}\hat{\Theta}^{\mathrm{p2}}(k,{}^{l}\!/_{h})\mathrm{e}^{2\pi\mathrm{i}lr/h},\end{aligned} \tag{4.9}$$

where $M_3 \in 2\mathbb{N}$ has to be chosen sufficiently large. In general, the functions $\Theta^{\mathrm{p2}}(k,\cdot)$ are sufficiently small outside the simulation box only for relatively large k. For small $k > 0$ we may have to choose a relatively large period $h \gg \max|x_{ij,3}|$, which implies the necessity of a large cutoff $M_3 \in 2\mathbb{N}$ in order to achieve a certain accuracy. Moreover, the $k = 0$ part has to be considered separately as $\lim_{|r|\to\infty}\Theta_0^{\mathrm{p2}}(r) = +\infty$.

Alternatively, we could proceed as follows. First, we truncate the Fourier integral and, second, we approximate the resulting finite integral via the trapezoidal quadrature rule

$$\begin{aligned}\Theta^{\mathrm{p2}}(k,r) &= \int_{\mathbb{R}}\hat{\Theta}^{\mathrm{p2}}(k,\xi)\mathrm{e}^{2\pi\mathrm{i}r\xi}\mathrm{d}\xi \approx \int_{-K/2}^{K/2}\hat{\Theta}^{\mathrm{p2}}(k,\xi)\mathrm{e}^{2\pi\mathrm{i}r\xi}\mathrm{d}\xi\\ &\approx \frac{K}{M_3}\sum_{l=-M_3/2}^{M_3/2-1}\hat{\Theta}^{\mathrm{p2}}(k,\tfrac{lK}{M_3})\mathrm{e}^{2\pi\mathrm{i}rlK/M_3}.\end{aligned} \tag{4.10}$$

Now, the coefficients of the trigonometric sum can be computed via an FFT. Comparision of (4.9) and (4.10) shows that this approach is equivalent to considering a $h = {}^{M_3}\!/_{K}$ periodization of $\Theta^{\mathrm{p2}}(k,\cdot)$, as described above.

We remark that this method is used in [35]. As pointed out in [35, page 12] this approach is limited to functions that decay sufficiently fast in the interval $[-{}^{h}\!/_{2}, {}^{h}\!/_{2})$. In other words,

whenever $\Theta^{\mathrm{p2}}(k, \max|x_{ij,3}|)$ is not sufficiently small we need to choose a relatively large period $h \gg 2L$, which may also result in the choice of a large cutoff M_3. Indeed, the authors need an oversampling factor in this direction by a factor of 6, see [35, Section 4.1]. Nevertheless we stress that the accuracy of the method depends on this oversampling parameter, but the convergence rate, see [34, Theorem 3.1], does not, cf. the discussion in [33, Section 3.2.1]. Obviously, for the non-decreasing function $\phi^{\mathrm{p2},\mathbf{0}}$ another approximation has to be used.

Variant II (Truncation): Another approach is taken in [37, 49]. The infinite Fourier integral regarding the periodic dimensions is computed using the Poisson summation formula and truncated Fourier integrals are evaluated for the non-periodic dimension, cf. equation (2.7) in [37]. In other words, in the long range part of the Ewald sum we take a sufficiently large cutoff h and approximate the functions $\Theta^{\mathrm{p2}}(k,\cdot)$ on the interval $[-h/2, h/2]$ by a Fourier series

$$\Theta^{\mathrm{p2}}(k,r) \approx \sum_{l=M_3/2}^{M_3/2-1} c_l \mathrm{e}^{2\pi \mathrm{i} l r/h},$$

where we compute the coefficients c_l by

$$c_l := \frac{1}{h}\int_{-h/2}^{h/2} \Theta^{\mathrm{p2}}(k,r)\mathrm{e}^{2\pi \mathrm{i} l r/h}\mathrm{d}r.$$

The coefficients c_l are known analytically; cf. equation (2.9) in [37]. In our notation, we have

$$\begin{aligned} c_l \sim & \frac{h}{\pi(k^2h^2+l^2L^2)}\mathrm{e}^{-\pi^2k^2/(\alpha^2L^2)-\pi^2l^2/(\alpha^2h^2)}\mathrm{Re}\left[\mathrm{erfc}\left(\tfrac{\alpha h}{2}-\tfrac{\pi \mathrm{i} l}{\alpha h}\right)\right] \\ & - \frac{h\cos(\pi l)}{\pi(k^2h^2+l^2L^2)}\left(\mathrm{e}^{\pi kh/L}-\tfrac{1}{2}\mathrm{e}^{-\pi kh/L}\,\mathrm{erfc}\left(\tfrac{\alpha h}{2}-\tfrac{\pi k}{\alpha L}\right)-\tfrac{1}{2}\mathrm{e}^{\pi kh/L}\,\mathrm{erfc}\left(\tfrac{\alpha h}{2}+\tfrac{\pi k}{\alpha L}\right)\right), \end{aligned}$$

i.e., $c_l = \mathcal{O}(l^{-2})$ as $l \to \infty$. Note that the approximated h-periodic function is only smooth of order zero in $r = h/2$, which results in a rather slow second order convergence in Fourier space. Thus, one may have to choose M_3 very large in order to achieve a good approximation. In contrast to Variant I, this approximation approach can be used for $\phi^{\mathrm{p2},\mathbf{0}}$ as well.

Variant III (Regularization): In this paper we propose another approach how to obtain a Fourier space representation of the long range part. The key idea is to cutoff $\Theta^{\mathrm{p2}}(k,\cdot)$ outside the interval $[-L, L]$ but use a Fourier approximation on the slightly larger interval $[-h/2, h/2]$. In the resulting gap $[L, h-L]$ we construct a regularization function that interpolates the derivatives up to order $p-1 \in \mathbb{N}$ of $\Theta^{\mathrm{p2}}(k,\cdot)$ at $r = L$. Therefore, we get a Fourier approximation of a $(p-1)$-times differentiable function which means $(p+1)$-th order convergence in Fourier space. A detailed explanation of our regularization approach is given in the next section. In summary, we see some graphical illustrations of the three different approaches.

The main advantage of our approach is that we construct a function of a high smoothness while the period h can be chosen relatively small compared to the doubled box length $2L$. In contrast, when applying Variant I we may have to choose h very large, which has to be compensated by a larger number of sampling nodes M_3. On the other hand, the fact that the approximated functions are C^∞ makes this approach spectrally accurate. Using Variant II allows us to choose h relatively small. But, the functions are only continuous and of no higher smoothness. Thus, the Fourier coefficients only decrease rather slow, which also results in the choice of a large cutoff M_3.

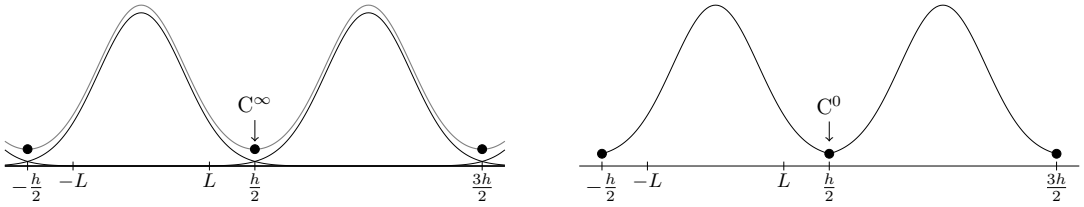

Figure 4.1: Variant I (periodization) on the left and Variant II (truncation) on the right side.

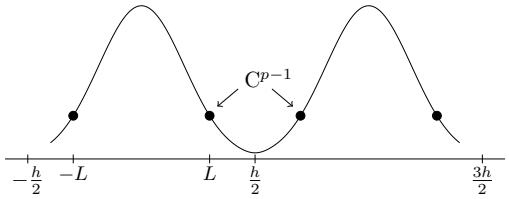

Figure 4.2: Variant III (regularization).

4.2. Fast NFFT based algorithm for 2d-periodic systems

Based on Theorem 4.1 we derive a fast algorithm. The evaluation of the short range part $\phi^{\mathrm{p2,S}}(\boldsymbol{x}_j)$ is done by a direct evaluation. For the computation of the long range part we apply the fast summation method [44] to the functions $\Theta^{\mathrm{p2}}(k,\cdot)$.

4.2.1. Computational approach

Due to Lemma 4.2 we can truncate the infinite sum in $\phi^{\mathrm{p2,L}}(\boldsymbol{x}_j)$, i.e., for some appropriate $\tilde{\boldsymbol{M}} = (M_1, M_2) \in 2\mathbb{N}^2$ we set

$$\phi^{\mathrm{p2,L}}(\boldsymbol{x}_j) \approx \frac{1}{2L} \sum_{\boldsymbol{k}\in\mathcal{I}_{\tilde{\boldsymbol{M}}}\setminus\{\boldsymbol{0}\}} \sum_{i=1}^{N} q_i \mathrm{e}^{2\pi\mathrm{i}\boldsymbol{k}\cdot\tilde{\boldsymbol{x}}_{ij}/L} \Theta^{\mathrm{p2}}(\|\boldsymbol{k}\|, x_{ij,3}). \tag{4.11}$$

Without loss of generality we can assume $x_{j,3} \in [-L_3/2, L_3/2]$, i.e., the particle coordinates are bounded also in the non-periodic dimension. Thus, all the functions $\Theta^{\mathrm{p2}}(\|\boldsymbol{k}\|,\cdot)$ have to be evaluated only within the finite interval $[-L_3, L_3]$. Note that we have to double the interval length since we do not have periodicity in the last dimension. The main idea is to approximate the functions $\Theta^{\mathrm{p2}}(\|\boldsymbol{k}\|,\cdot)$ on this interval by a truncated Fourier series. However, the odd derivatives of $\Theta^{\mathrm{p2}}(\|\boldsymbol{k}\|,\cdot)$ at the points $-L_3$ and L_3 do not match, which yields a bad convergence rate of the Fourier series. Therefore, we extend the interval at both ends, where we construct a smooth transition. The same approximation idea is applied to the kernel function $\Theta_0^{\mathrm{p2}}(r)$ in (4.5). Note that $\lim_{x\to\pm\infty}[\mathrm{e}^{-x^2} + \sqrt{\pi}x\ \mathrm{erf}(x)] = \lim_{x\to\pm\infty}|x| = \infty$, i.e., the analytical Fourier transform does not exist. Anyway, the fast summation approach does not require any localization of the kernel function. In the following, we give the formal derivation of this idea.

At first, we choose $h > 2\cdot L_3$ and accordingly some $\varepsilon \in (0, 1/2)$ such that $|x_{ij,3}| \le L_3 =: h(1/2 - \varepsilon) < h/2$ for all $i, j = 1, \ldots, N$. This corresponds to a surrounding box that is large enough to hold all differences of particle coordinates in the last dimension. In addition, since

the strong inequality $h > 2L_3$ holds we have some extra space for constructing a regularization. In order to approximate the long range parts $\phi^{\mathrm{p2,L}}(\boldsymbol{x}_j) + \phi^{\mathrm{p2},\mathbf{0}}(\boldsymbol{x}_j)$ efficiently we consider for $k \in \{\|\boldsymbol{k}\| : \boldsymbol{k} \in \mathcal{I}_{\tilde{\boldsymbol{M}}}\}$ the regularizations

$$K_{\mathrm{R}}(k,r) := \begin{cases} \dfrac{1}{2L}\Theta^{\mathrm{p2}}(k,r) & : k \neq 0, |h^{-1}r| \leq 1/2 - \varepsilon, \\ -\dfrac{2\sqrt{\pi}}{L^2}\Theta_0^{\mathrm{p2}}(r) & : k = 0, |h^{-1}r| \leq 1/2 - \varepsilon, \\ K_{\mathrm{B}}(k,r) & : |h^{-1}r| \in (1/2 - \varepsilon, 1/2], \end{cases} \tag{4.12}$$

where we claim that each function $K_{\mathrm{B}}(k,\cdot) : [-h/2 + h\varepsilon, -h/2] \cup [h/2, h/2 - h\varepsilon] \to \mathbb{R}$ fulfills the Hermite interpolation conditions

$$\frac{\partial^j}{\partial r^j} K_{\mathrm{B}}(k, h/2 - h\varepsilon) = \begin{cases} \frac{1}{2L}\frac{\partial^j}{\partial r^j}\Theta^{\mathrm{p2}}(k, h/2 - h\varepsilon) & : k \neq 0 \\ -\frac{2\sqrt{\pi}}{L^2}\frac{\mathrm{d}^j}{\mathrm{d}r^j}\Theta_0^{\mathrm{p2}}(h/2 - h\varepsilon) & : k = 0 \end{cases}, \tag{4.13}$$

$$\frac{\partial^j}{\partial r^j} K_{\mathrm{B}}(k, -h/2 + h\varepsilon) = \begin{cases} \frac{1}{2L}\frac{\partial^j}{\partial r^j}\Theta^{\mathrm{p2}}(k, -h/2 + h\varepsilon) & : k \neq 0 \\ -\frac{2\sqrt{\pi}}{L^2}\frac{\mathrm{d}^j}{\mathrm{d}r^j}\Theta_0^{\mathrm{p2}}(-h/2 + h\varepsilon) & : k = 0 \end{cases} \tag{4.14}$$

for all $j = 0, \ldots, p-1$. Hereby, we refer to $p \in \mathbb{N}$ as the degree of smoothness. In order to end up with h-periodic, smooth functions $K_{\mathrm{R}}(k,\cdot)$, the functions $K_{\mathrm{B}}(k,\cdot)$ are constructed such that

$$\frac{\partial^j}{\partial r^j} K_{\mathrm{R}}(k, h/2) = \frac{\partial^j}{\partial r^j} K_{\mathrm{R}}(k, -h/2), \quad j = 0, \ldots, p-1$$

is also fulfilled. In Section 4.2.2 we show that the functions $K_{\mathrm{B}}(k,.)$ can be constructed as polynomials of degree $2p-1$ by two point Taylor interpolation. Figure 4.3 shows an example of such a regularization $K_{\mathrm{R}}(k,\cdot)$.

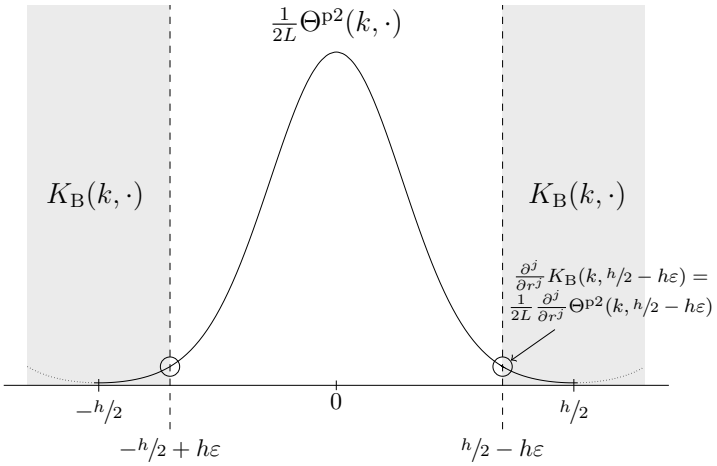

Figure 4.3: Example for $K_{\mathrm{R}}(k,\cdot)$ for $k \geq 1$. At the boundaries (gray area) the regularization adopts the values of the boundary function $K_{\mathrm{B}}(k,\cdot)$. We also marked the points, where the conditions (4.13) and (4.14) are fulfilled. In our implementation, the function in the gray area is a polynomial of degree $2p-1$ constructed by two-point Taylor interpolation.

In summary, the functions $K_{\mathrm{R}}(k,\cdot)$ are h-periodic and smooth, i.e., $K_{\mathrm{R}}(k,\cdot) \in \mathrm{C}^{p-1}(h\mathbb{T})$. Therefore, they can be approximated by a truncated Fourier series up to a prescribed error. To this end, we approximate for each $k \in \{\|\boldsymbol{k}\| \neq 0 : \boldsymbol{k} \in \mathcal{I}_{\tilde{\boldsymbol{M}}}\}$ the function

$$\frac{1}{2L}\Theta^{\mathrm{p2}}(k,r) \approx \sum_{l\in\mathcal{I}_{M_3}} \hat{b}_{k,l}\mathrm{e}^{2\pi\mathrm{i}lr/h} \tag{4.15}$$

for $|r| \leq {}^{h}\!/_{2} - h\varepsilon = L_3$ by the truncated Fourier series of its regularization $K_{\mathrm{R}}(k,\cdot)$. Analogously, for $k = 0$ we have

$$-\frac{2\sqrt{\pi}}{L^2}\Theta_0^{\mathrm{p2}}(r) \approx \sum_{l\in\mathcal{I}_{M_3}} \hat{b}_{0,l}\mathrm{e}^{2\pi\mathrm{i}lr/h}. \tag{4.16}$$

Thereby, we choose the frequency cutoff $M_3 \in 2\mathbb{N}$ large enough and compute the Fourier coefficients $\hat{b}_{k,l}$ in (4.15) as well as $\hat{b}_{0,l}$ in (4.16) by the discrete Fourier transform

$$\hat{b}_{k,l} := \frac{1}{M_3}\sum_{j\in\mathcal{I}_{M_3}} K_{\mathrm{R}}\left(k, \tfrac{jh}{M_3}\right)\mathrm{e}^{-2\pi\mathrm{i}jl/M_3}, \qquad l = -{}^{M_3}\!/_{2},\dots,{}^{M_3}\!/_{2}-1. \tag{4.17}$$

This ansatz is closely related to the fast summation method described in [44]. Due to the fact that we have $\Theta_0^{\mathrm{p2}}(\cdot), \Theta^{\mathrm{p2}}(k,\cdot) \in \mathrm{C}^\infty(\mathbb{R})$ $(k \geq 1)$ we are not restricted in the choice of the parameter p. By choosing M_3 large enough we can construct approximations (4.15) of a required accuracy.

In summary, we obtain the following approximation for the long range parts,

$$\begin{aligned}\phi^{\mathrm{p2,L}}(\boldsymbol{x}_j) + \phi^{\mathrm{p2},\mathbf{0}}(\boldsymbol{x}_j) &\approx \sum_{\boldsymbol{k}\in\mathcal{I}_{\tilde{\boldsymbol{M}}}}\sum_{l\in\mathcal{I}_{M_3}} \hat{b}_{\|\boldsymbol{k}\|,l}\sum_{i=1}^{N} q_i\mathrm{e}^{2\pi\mathrm{i}\boldsymbol{k}\cdot\tilde{\boldsymbol{x}}_{ij}/L}\mathrm{e}^{2\pi\mathrm{i}lx_{ij,3}/h}\\ &= \sum_{(\boldsymbol{k},l)\in\mathcal{I}_{\boldsymbol{M}}} \hat{b}_{\|\boldsymbol{k}\|,l}\left(\sum_{i=1}^{N} q_i\mathrm{e}^{2\pi\mathrm{i}\boldsymbol{v}(\boldsymbol{k},l)\cdot\boldsymbol{x}_i}\right)\mathrm{e}^{-2\pi\mathrm{i}\boldsymbol{v}(\boldsymbol{k},l)\cdot\boldsymbol{x}_j},\end{aligned} \tag{4.18}$$

where we substitute the truncated Fourier series (4.15), (4.16) into Theorem 4.1 and define $\boldsymbol{M} := (\tilde{\boldsymbol{M}}, M_3) \in 2\mathbb{N}^3$ as well as the vectors $\boldsymbol{v}(\boldsymbol{k},l) := (\boldsymbol{k}/L, l/h) \in L^{-1}\mathbb{Z}^2 \times h^{-1}\mathbb{Z}$. The expressions in the inner brackets

$$\hat{S}(\boldsymbol{k},l) := \sum_{i=1}^{N} q_i\mathrm{e}^{2\pi\mathrm{i}\boldsymbol{v}(\boldsymbol{k},l)\cdot\boldsymbol{x}_i}, \quad (\boldsymbol{k},l) \in \mathcal{I}_{\boldsymbol{M}} \tag{4.19}$$

can be computed by an NFFT$^{\mathrm{H}}$. This will be followed by $|\mathcal{I}_{\boldsymbol{M}}|$ multiplications with $\hat{b}_{\|\boldsymbol{k}\|,l}$ and completed by an NFFT to compute the outer summation with the complex exponentials. Therefore, the proposed evaluation of $\phi^{\mathrm{p2,L}}(\boldsymbol{x}_j) + \phi^{\mathrm{p2},\mathbf{0}}(\boldsymbol{x}_j)$ at the points $\boldsymbol{x}_j$, $j = 1,\dots,N$, requires $\mathcal{O}(N + |\mathcal{I}_{\boldsymbol{M}}|\log|\mathcal{I}_{\boldsymbol{M}}|)$ arithmetic operations.

The calculation of the forces is done analogously to the 3d-periodic case. We set $\mathcal{S} := \mathbb{Z}^2\times\{0\}$, define $\boldsymbol{F}^{\mathrm{p2}}(\boldsymbol{x}_j) := \boldsymbol{F}_{\mathcal{S}}(\boldsymbol{x}_j)$ via (1.4) and calculate the short range portions $\boldsymbol{F}^{\mathrm{p2,S}}(\boldsymbol{x}_j)$ given by (3.7) via a direct summation. In the long range part we can either use the i$\boldsymbol{k}$ approach, i.e., we set

$$\boldsymbol{F}^{\mathrm{p2,L}}(\boldsymbol{x}_j) + \boldsymbol{F}^{\mathrm{p2},\mathbf{0}}(\boldsymbol{x}_j) \approx 2\pi\mathrm{i}q_j\sum_{(\boldsymbol{k},l)\in\mathcal{I}_{\boldsymbol{M}}} \hat{b}_{\|\boldsymbol{k}\|,l}\left(\sum_{i=1}^{N} q_i\mathrm{e}^{2\pi\mathrm{i}\boldsymbol{v}(\boldsymbol{k},l)\cdot\boldsymbol{x}_i}\right)\boldsymbol{v}(\boldsymbol{k},l)\mathrm{e}^{-2\pi\mathrm{i}\boldsymbol{v}(\boldsymbol{k},l)\cdot\boldsymbol{x}_j}, \tag{4.20}$$

or the analytic differentiation, where the ∇ operator is applied to the window function $\tilde{\varphi}$ in (2.3) within the NFFT, cf. (3.9).

In summary, we obtain Algorithm 4.3 for the fast computation of 2d-periodic Coulomb interactions. As it can be seen, we compute the regularizations $K_{\mathrm{R}}(k,\cdot)$ and the discrete Fourier coefficients $\hat{b}_{k,l}$ in a precomputation step. Note, that these coefficients only depend on L, α and ε or rather h. In a simulation, where these parameters are fixed and only the particle positions $\boldsymbol{x}_j$ are changing such that $|x_{ij,3}| \leq L_3$ always holds, we only need to do these precomputation step once.

Algorithm 4.3 (2d-periodic P^{2}NFFT)**.**

Input: *Positions $\boldsymbol{x}_j \in L\mathbb{T}^2 \times [-L_3/2, L_3/2]$, charges $q_j \in \mathbb{R}$ $(j = 1,\dots,N)$, splitting parameter $\alpha > 0$, short range cutoff $r_{\mathrm{cut}} > 0$, long range cutoff $\boldsymbol{M} = (\tilde{\boldsymbol{M}}, M_3) \in 2\mathbb{N}^3$, regularization parameter $\varepsilon > 0$, degree of smoothness $p \in \mathbb{N}$.*

0.) Precomputations:
- *a) Set $h := (1/2 - \varepsilon)^{-1} L_3$.*
- *b) Construct the regularization* (4.12) *for each $k \in \{\|\boldsymbol{k}\| : \boldsymbol{k} \in \mathcal{I}_{\tilde{\boldsymbol{M}}}\}$.*
- *c) Compute the Fourier coefficients* (4.17)*.*

1.) Compute the short range parts of the potentials $\phi^{\mathrm{p2,S}}(\boldsymbol{x}_j)$ and the short range parts of the forces $\boldsymbol{F}^{\mathrm{p2,S}}(\boldsymbol{x}_j)$ by direct evaluation, i.e., restrict the summation in (4.3) *and* (3.7)*, where $\mathcal{S} := \mathbb{Z}^2 \times \{0\}$, to all $\|\boldsymbol{x}_{ij} + L\boldsymbol{n}\| \leq r_{\mathrm{cut}}$.*

2.) Compute the sums $\hat{S}(\boldsymbol{k}, l)$ in (4.19) *by the adjoint NFFT* (2.4)*.*

3.) Apply the NFFT (2.2) *to compute the long range parts of the potentials $\phi^{\mathrm{p2,L}}(\boldsymbol{x}_j) + \phi^{\mathrm{p2},\mathbf{0}}(\boldsymbol{x}_j)$ by* (4.18)*.*

4.) Compute the long range parts of the forces $\boldsymbol{F}^{\mathrm{p2,L}}(\boldsymbol{x}_j) + \boldsymbol{F}^{\mathrm{p2},\mathbf{0}}(\boldsymbol{x}_j)$ via the $i\boldsymbol{k}$ differentiation approach (4.20) *or the analytic differentiation, cf.* (3.9)*.*

5.) For all $j = 1,\dots,N$ compute

$$\phi^{\mathrm{p2}}(\boldsymbol{x}_j) = \phi^{\mathrm{p2,S}}(\boldsymbol{x}_j) + \phi^{\mathrm{p2,L}}(\boldsymbol{x}_j) + \phi^{\mathrm{p2},\mathbf{0}}(\boldsymbol{x}_j) + \phi^{\mathrm{p2,self}}(\boldsymbol{x}_j)$$
$$\boldsymbol{F}^{\mathrm{p2}}(\boldsymbol{x}_j) = \boldsymbol{F}^{\mathrm{p2,S}}(\boldsymbol{x}_j) + \boldsymbol{F}^{\mathrm{p2,L}}(\boldsymbol{x}_j) + \boldsymbol{F}^{\mathrm{p2},\mathbf{0}}(\boldsymbol{x}_j).$$

6.) Compute the total energy (4.2) *and set $U^{\mathrm{p2}}(\boldsymbol{x}_j) := q_j \phi^{\mathrm{p2}}(\boldsymbol{x}_j)$.*

Output: *Total energy U^{p2}, single energies $U^{\mathrm{p2}}(\boldsymbol{x}_j)$ and forces $\boldsymbol{F}^{\mathrm{p2}}(\boldsymbol{x}_j)$.*

Remark 4.4. Algorithm 4.3 has the same structure as the NFFT based method for 3d-periodic systems, cf. Section 3. Thus, we also obtain a matrix vector notation of the form (3.6) for the approximation of $\phi^{\mathrm{p2,L}}(\boldsymbol{x}_j) + \phi^{\mathrm{p2},\mathbf{0}}(\boldsymbol{x}_j)$. In other words, we use the same algorithm, where we replace the Fourier coefficients $\hat{b}_{\boldsymbol{k}}$ from (3.5) by the new coefficients $\hat{b}_{\|\boldsymbol{k}\|,l}$ in (4.17) and insert the nodes $(\tilde{\boldsymbol{x}}_{ij}/L, x_{ij,3}/h) \in \mathbb{T}^3$ instead of $\boldsymbol{x}_{ij}/L \in \mathbb{T}^3$ into the NFFT algorithms. □

4.2.2. Implementation details

The precomputation step of Algorithm 4.3 includes the construction of the regularizations (4.12). Thereby, we obtain $K_{\mathrm{B}}(k,\cdot)$ by the unique polynomial of degree $2p-1$ that fulfills the $2p$ Hermite interpolation conditions (4.13) – (4.14) in two points. An explicit representation of this polynomial is given by Theorem C.1 in the appendix, where we set $m = h/2$ and $r = h\varepsilon$ and a_j, b_j equal to the right hand sides of the interpolation conditions (4.13) – (4.14), respectively.

In order to compute the derivatives in (4.13) – (4.14) we use the following relations. We define the function

$$\Theta_1(k,r) := \mathrm{e}^{2\pi kr/L}\operatorname{erfc}\left(\frac{\pi k}{\alpha L}+\alpha r\right) \tag{4.21}$$

and let $\Theta_\pm(k,r) := \Theta_1(k,r) \pm \Theta_1(k,-r)$. Note that we have $\Theta^{\mathrm{p2}}(k,r) = \frac{1}{k}\Theta_+(k,r)$. We immediately see that

$$\begin{aligned}\frac{\partial}{\partial r}\Theta_+(k,r) &= \frac{2\pi k}{L}\Theta_-(k,r),\\ \frac{\partial}{\partial r}\Theta_-(k,r) &= \frac{2\pi k}{L}\Theta_+(k,r) - \frac{4\alpha}{\sqrt{\pi}}\mathrm{e}^{-\alpha^2r^2-\pi^2k^2/(\alpha^2L^2)},\end{aligned}$$

and, therefore,

$$\frac{\partial^2}{\partial r^2}\Theta_+(k,r) = \frac{4\pi^2k^2}{L^2}\Theta_+(k,r) - \frac{8\alpha\sqrt{\pi}k}{L}\mathrm{e}^{-\alpha^2r^2-\pi^2k^2/(\alpha^2L^2)}. \tag{4.22}$$

For the computation of the derivatives of order $n \geq 2$ we use the following recursive formula

$$\frac{\partial^n}{\partial r^n}\Theta_+(k,r) = \frac{4\pi^2k^2}{L^2}\frac{\partial^{(n-2)}}{\partial r^{(n-2)}}\Theta_+(k,r) - \frac{\partial^{(n-2)}}{\partial r^{(n-2)}}\frac{8\alpha\sqrt{\pi}k}{L}\mathrm{e}^{-\alpha^2r^2-\pi^2k^2/(\alpha^2L^2)}.$$

The second term can be computed easily with the derivatives of the Gaussian window function

$$\frac{\partial^{(n-2)}}{\partial r^{(n-2)}}\frac{8\alpha\sqrt{\pi}k}{L}\mathrm{e}^{-\alpha^2r^2-\pi^2k^2/(\alpha^2L^2)} = \frac{8\alpha\sqrt{\pi}k}{L}\mathrm{e}^{-\pi^2k^2/(\alpha^2L^2)}\frac{\partial^{(n-2)}}{\partial r^{(n-2)}}\mathrm{e}^{-\alpha^2r^2}.$$

We remark that the numerical evaluation of the function (4.21) for large $k, r > 0$ is important in order to obtain a regularization of the 2d-periodic Ewald splitting. This can be done straight forward for $r \leq 0$, since we have the trivial upper bound $\Theta_1(k,r) \leq 2$. In contrast, for large values of $r > 0$ the exponential tends to infinity and exceeds rapidly the range of representable floating point numbers in double precision. However, since the complementary error function tends much faster to zero, we expect that the function $\Theta(k,r)$ can be considered numerically equal to zero for $kr > 0$ large enough. More precisely, for the substitutions $l = \frac{\pi k}{L\alpha} > 0$ and $t = lr\alpha = \frac{\pi kr}{L} > 0$ we can use the standard estimate $0 \leq (l-\sqrt{t})^2$ that yields $2\sqrt{t} \leq l + t/l$ and, finally, we obtain

$$\Theta_1(k,r) = \Theta_1\left(\frac{lL\alpha}{\pi}, \frac{tL}{\pi k}\right) = \mathrm{e}^{2t}\operatorname{erfc}\left(l+\tfrac{t}{l}\right) \leq \mathrm{e}^{2t}\operatorname{erfc}\left(2\sqrt{t}\right).$$

The right hand side holds $\mathrm{e}^{2t}\operatorname{erfc}\left(2\sqrt{t}\right) < 10^{-16}$ for $t \geq 18$, i.e., whenever $t := \frac{\pi kr}{L} \geq 18$ we can assume $\Theta_1(k,r)$ to be numerically equal to zero.

Moreover, for $t = \frac{\pi kr}{L} \geq 19$ we have $\Theta_1(k,r) < \mathrm{e}^{2t}\operatorname{erfc}\left(2\sqrt{t}\right) < 3\cdot 10^{-18}$ and $\Theta_1(k,-r) \leq 2\mathrm{e}^{-2t} < 6.3\cdot 10^{-17}$. Altogether, we get

$$\Theta^{\mathrm{p2}}(k,r) = \frac{1}{k}\Theta_+(k,r) \leq \Theta_1(k,r) + \Theta_1(k,-r) < 10^{-16} \quad \text{for} \quad \frac{\pi kr}{L} \geq 19.$$

In this case we do not need to compute the regularization (4.12), since we can assume that it is equal to zero up to double precision in the whole regularization interval.

4.3. Numerical results

In this section we present numerical results of our algorithm for 2d-periodic boundary conditions. We implemented this algorithm as a part of the P^{2}NFFT solver [42] within the Scalable Fast Coulomb Solver (ScaFaCoS) library [1], i.e., our implementation is publicly available at [1] and can be compared to various other well established methods with respect to accuracy and runtime. Recently, this library has been used for a broad comparison of various fast Coulomb solvers for 3d-periodic boundary conditions [5]. In the following, we show that our 2d-periodic algorithm can be tuned to high accuracy and offers a runtime comparable to the well established P^{3}M algorithm for 3d-periodic systems.

For all tests the calculation of the forces was performed using the i$\boldsymbol{k}$ differentiation approach, cf. (3.8). Whenever rms errors are examined, the comparative data were computed with the fast multipole method [12, 28, 27] within ScaFaCoS tuned to sufficient accuracy.

Our runtime measurements have been performed on an Intel i5-2400 single core processor that runs on 3.10 GHz with 8 GB main memory. The software was built with the Gnu C Compiler at version 4.7.1 and optimization flags "-O3".

4.3.1. Parameter Choice

In our numerical experiments, see section 4.3.2, we will only consider test cases, where the charges are located in a cubic box $[-L/2, L/2]^3$. Based on this, we suggest the following heuristic parameter choice.

In comparision to the 3d-periodic case, we introduced several new parameters in order to characterize the regularization in the non-periodic dimension. Now, we give a heuristic approach how to determine the new parameters in dependence on the parameters of the 3d-periodic case. The key idea of our approach is to keep the number of grid points per box length at a constant level. Our numerical examples show that this heuristic yields comparable accuracy for the 3d- and 2d-periodic case.

Assume that the parameters of the 3d-periodic case that are the short range cutoff r_{cut}, the Ewald splitting parameter α, the (cubic) FFT grid size $\boldsymbol{M} = (M, M, M) \in 2\mathbb{N}^3$, the oversampled grid size $\boldsymbol{m} = (m, m, m) \in 2\mathbb{N}^3$ and the B-Spline order are given such that the short range part is computationally tractable and the 3d-periodic P^{2}NFFT reaches a prescribed accuracy goal. In our numerical examples we will use two different approaches in order to get a suitable parameter set for the 3d-periodic case. The first one is to use the error estimates of [15] and the second one is based on an adaption of the error estimates [30] for the 3d-periodic Ewald sum; see Examples 4.5 and 4.8 for details. We use most of these parameters directly for the 2d-periodic case. The only difference is the FFT grid size corresponding to non-periodic dimensions that is determined as follows. At first, we set the cutoff length of the periodic dimensions in the long range part of the Ewald formula (4.11) to $\tilde{\boldsymbol{M}} := (M, M)$. The box size regarding the non periodic dimension can be implicitly expressed by $h = 2L + 2h\varepsilon$, where $2h\varepsilon$ is the sum of the lengths of the two segments at the boundaries, which are added for the regularization. Based on this, we set M_3 in (4.15) and (4.16) to

$$M_3 := 2M + P \text{ with } P \in 2\mathbb{N}, \tag{4.23}$$

i.e., we fix the number of grid points located in the interval of length $2L$ to $2M$ and spend some extra P grid points for the regularization domain. For a graphical illustration of the grid point distribution see Figure 4.4.

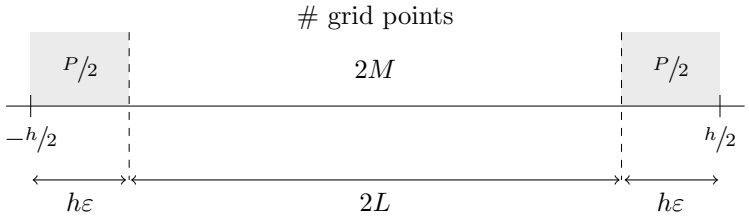

Figure 4.4: Distribution of the grid points over $[-h/2, h/2]$.

Having defined P, the corresponding value for ε is given by

$$\frac{2h\varepsilon}{h} = \frac{P}{2M+P} \iff \varepsilon = \frac{1}{2}\frac{P}{2M+P} = \frac{P}{2M_3}$$

and $h = (1/2 - \varepsilon)^{-1}L = \frac{2M+P}{M} \cdot L$. Finally, we apply the same oversampling factor as for the periodic dimensions, i.e., we set $m_3 = \frac{m}{M}M_3$.

Note that our heuristic parameter selection substitutes the problem of finding the regularization parameter ε into the problem of finding the number of extra grid points P spent for regularization. The optimal value P will depend on the required accuracy and the smoothness p of the regularization function. However, it is reasonable that we can achieve the same accuracy level for increasing system size at constant P and p, i.e., the amount of extra work for regularization does not depend on the system size, cf. Example 4.7. Therefore, good values for P and p can be computed for small test systems.

Furthermore, we can see that the asymptotic increase of grid points for large L does not depend on the regularization. The same accuracy is reached for larger box sizes at a constant amount of extra work for the regularization. This also means that the complexity of our algorithm is not sensitive to an optimal choice of the number of grid points P in the regularization domain and the degree of smoothness p. While p does only influences the precomputation time, the constant P gets less important for large M. Especially, we see that the asymptotic runtime of the 2d-periodic case is equal to the 3d-periodic case, i.e., $\mathcal{O}(N \log N)$. However, we stress that a proof of this error behavior is still missing and gives raise to future research.

The parameter selection can be summarized in the following three easy steps:

i) Determine the near field cutoff r_{cut}, the Ewald splitting parameter α, the grid size $\boldsymbol{M}$, the oversampled grid size $\boldsymbol{m}$, and the B-Spline order by any parameter estimates suitable for the 3d-periodic case, e.g., [15].

ii) Set the degree of smoothness p not too small (in our tests $p := 10$ is sufficient) and tune the regularization grid size P for a small test case with a low number of particles N.

iii) Compute the grid size M_3 according to (4.23) and apply the periodic oversampling factor to the non-periodic dimension, i.e., $\boldsymbol{m} = m_1/M_1 \cdot \boldsymbol{M}$.

Note that only the regularization grid size P needs some tuning, while all other parameters are either known from the 3d-periodic case or can be computed easily.

4.3.2. Examples

Example 4.5. We consider a so called cloud wall system consisting of $N = 300$ charges in a cubic box of edge length $L = 10$ (see Figure 4.5). The system consists of a diffusive particle cloud surrounding two oppositely charged walls and was proposed in [5] because of

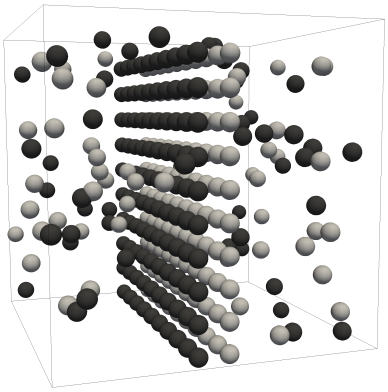

Figure 4.5: Cloud wall system with $N = 300$ charges $q_j = \pm 1$ in a cubic box, see [5].

its significant long range part. The following tests will give an idea on how the error depends on the different parameters. In order to get an impression of the involved functions in (4.12) we plot these functions over the interval $[-L, L]$ for different values of α, see Figure 4.6.

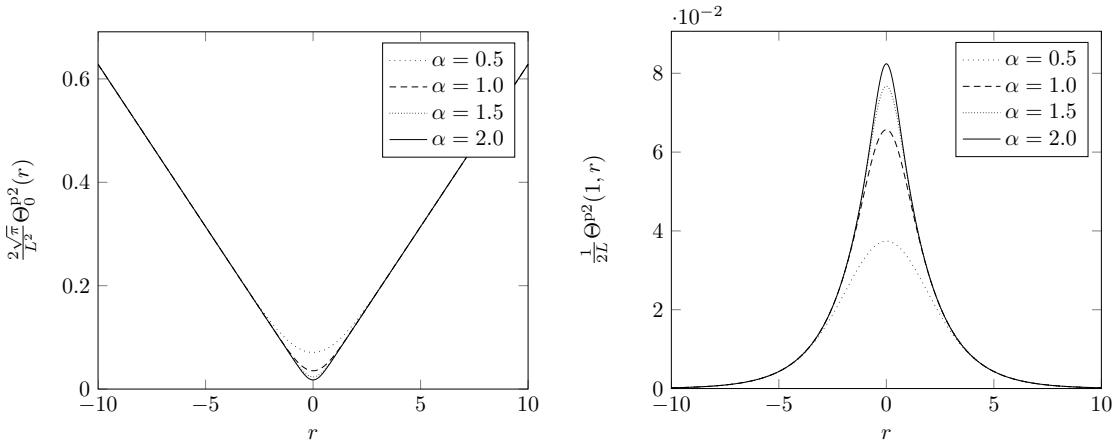

Figure 4.6: $\Theta_0^{\mathrm{p2}}(r)$ and $\Theta^{\mathrm{p2}}(1, r)$ with $L = 10$ for different splitting parameters α.

In the following we choose the degree of smoothness $p = 10$, i.e., we construct regularizations which are 9 times continuously differentiable. To get an idea on how the number of grid points P used for the regularization influences the accuracy of our approximations we set $M = 128$ and define M_3 with the above described approach using different values for P, see Figure 4.7.

It can be seen that we obtain a better approximation if P is increased. In order to achieve a required accuracy we have to choose P large enough. Of course, for very large values of P the error will only decrease insignificantly. In our example, the optimal rms errors stay at an almost constant level for $P \geq 44$ ($\Delta F_{\mathbb{Z}^2 \times \{0\}} \approx 2 \cdot 10^{-11}$). See also Appendix E for the influence of P on the per particle error distribution within the box.

In Figure 4.8, we choose $M = 64$ and plot the rms force error over α, where we choose $P \geq 22$. We see that the simple ansatz just to use $P = 22$ would lead to an unsatisfactory result as not until $P \approx 30$ the best possible rms force error ($\Delta F_{\mathbb{Z}^2 \times \{0\}} \approx 2 \cdot 10^{-9}$) is obtained. This shows that the task of choosing P large enough is quite complex.

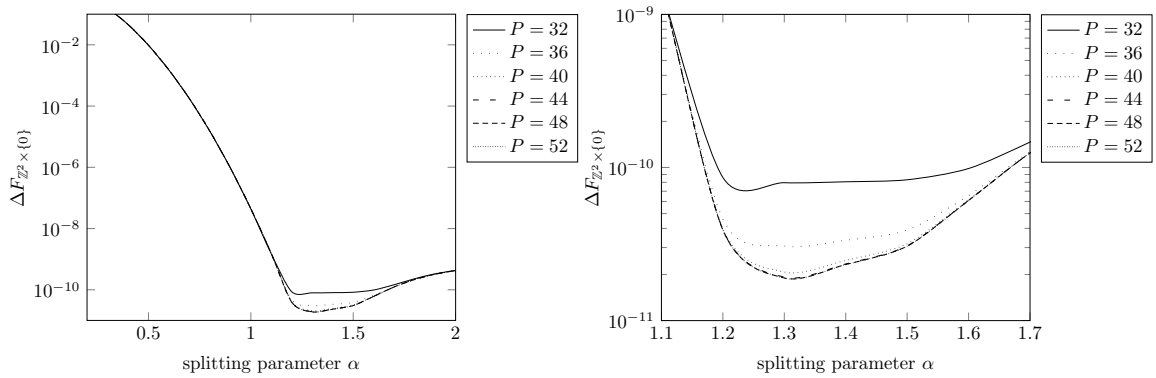

Figure 4.7: Rms force error (1.7) over α for different values of $P \in 2\mathbb{N}$. We choose the short range cutoff $r_{\text{cut}} = 4$, the smoothness $p = 10$, $\boldsymbol{M} = (128, 128, 256 + P) = \boldsymbol{m}$ and the B-Spline of order 8 as NFFT window function φ in Algorithm 4.3.

Obviously, the determination of the sufficiently large value for P also depends on how the near field cutoff r_{cut} is chosen, on the splitting parameter α and also the NFFT specific parameters, which influence the errors in the long range part. A complete error analysis has to be done in order to derive an automatic tuning of this parameter. In our example, we keep the cutoff radius in the near field r_{cut} fixed, while the far field parameters are changing. Thus, also the optimal splitting parameter α adopts different values. In Example 4.6 we give some concrete examples how the choice of P is influenced by other parameters.

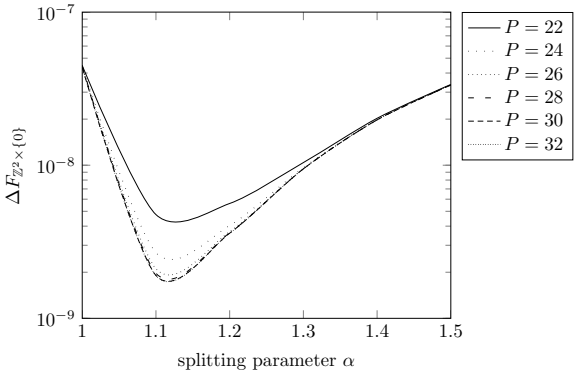

Figure 4.8: Rms force error (1.7) over α for different values of $P \in 2\mathbb{N}$. We choose the short range cutoff $r_{\text{cut}} = 4$, the smoothness $p = 10$, $\boldsymbol{M} = (64, 64, 128 + P) = \boldsymbol{m}$ grid points and the B-Spline of order 8 as NFFT window function φ in Algorithm 4.3.

In Figure 4.9 (left hand side) we plot the rms force error $\triangle F_{\mathbb{Z}^2\times\{0\}}$ with respect to the splitting parameter α for different FFT sizes $\boldsymbol{M} = (M, M, M_3)$, where M_3 is defined as in (4.23). In the case $M = 128$ we set $P := 44$, for $M = 64$ we add $P = 30$ grid points for the regularization. For the other values of M we also tuned P such that the best possible rms

force error is almost reached.

On the right hand side of Figure 4.9 we see the corresponding errors of the same particle system treated under 3d-periodic boundary conditions. It can be seen, that we achieve almost the same optimal rms force errors for both systems, which illustrates the reasonability of our approach to set the involved parameters. The corresponding values for P as well as for $h \geq 2L = 20$ can be found in the legend. □

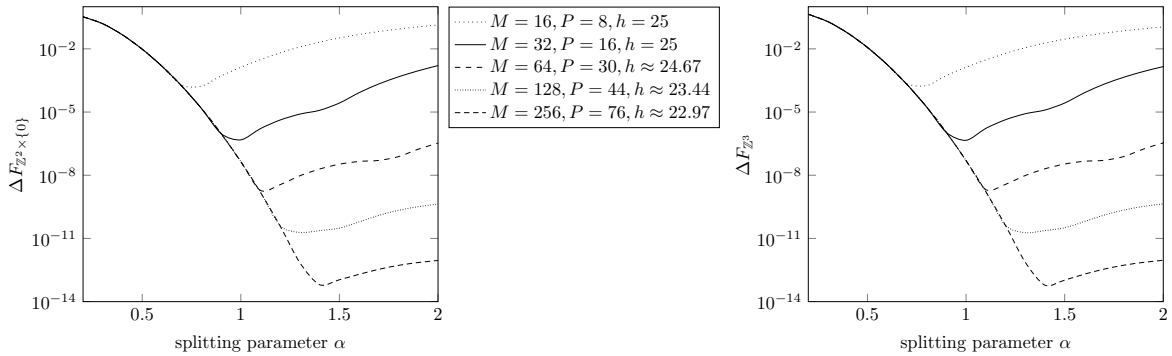

Figure 4.9: The rms force error (1.7) over α for different FFT sizes. We choose the short range cutoff $r_{\text{cut}} = 4$, the smoothness $p = 10$, $\boldsymbol{m} = \boldsymbol{M} = (M, M, M_3)$, where M_3 is defined by (4.23), and the B-Spline of order 8 as NFFT window function φ in Algorithm 4.3. We plot the results of the 2d-periodic (left) as well as of the 3d-periodic computation (right). (Test case: cloud wall system, $N = 300$.)

Example 4.6. With the following example we aim to give an idea on how other involved parameters have an influence on how large we have to choose the parameter $P \in 2\mathbb{N}$.

In Figure 4.10 we reconsider the behavior of the rms force error with respect to α, where we set $M = 64$ and choose different values for P, cf. Figure 4.8. We now compare the obtained results for the degree of smoothness $p = 10$ with those obtained setting $p = 12$. Obviously, constructing regularizations of a higher smoothness, which may make the precomputation step more expensive, allows us to spend less grid points P for the regularization intervals in order to achieve a certain accuracy.

In Figure 4.11 we compare the results for the near field cutoffs $r_{\text{cut}} = 4$ and $r_{\text{cut}} = 3.5$. The choice of a smaller cutoff radius r_{cut} produces larger errors regarding the near field. The optimal rms force error increases and is adopted for some larger splitting parameter α. Thus, for $r_{\text{cut}} = 3.5$ we do not need to spend that many grid points P for the regularization as in the case $r_{\text{cut}} = 4$. For a larger near field cutoff r_{cut} we would have to further increase P in order to reach the best possible rms error. □

Example 4.7. We compute the energies $U^{\text{p2}}(\boldsymbol{x}_j)$ as well as the forces $F^{\text{p2}}(\boldsymbol{x}_j)$ in cloud wall systems of different size, where the particles are distributed in a cubic box of edge length L.

It can be seen from the data in Table 4.1 that the systems have the same particle density. Therefore, the computations in the near field with fixed values of the short range cutoff r_{cut} and the splitting parameter α are comparable. Within the long range part computations (4.18) we choose $\boldsymbol{M} = (M, M, M_3) \in 2\mathbb{N}^3$, where M_3 is defined by (4.23), and apply the

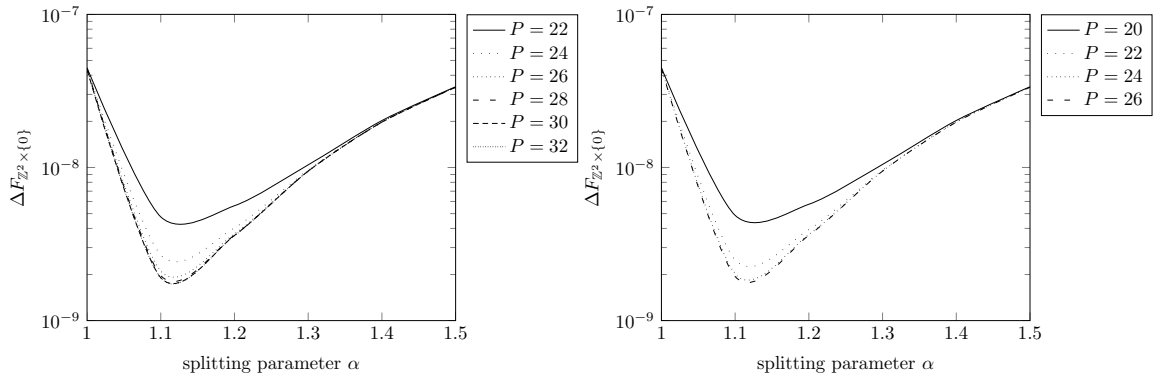

Figure 4.10: Rms force error (1.7) over α for different values of $P \in 2\mathbb{N}$. We choose the short range cutoff $r_{\text{cut}} = 4$, $\boldsymbol{M} = (64, 64, 128 + P) = \boldsymbol{m}$ and the B-Spline of order 8 as NFFT window function φ in Algorithm 4.3. The degree of smoothness p is set to $p := 10$ (left) and to $p := 12$ (right), respectively.

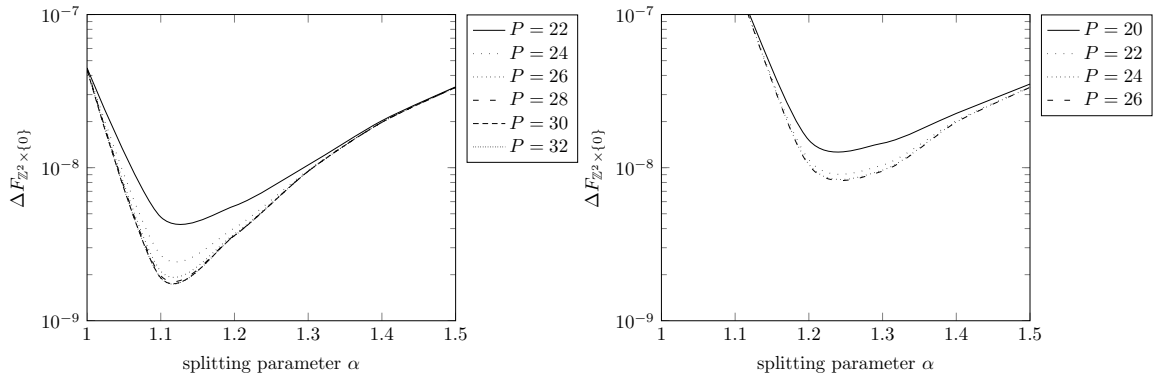

Figure 4.11: Rms force error (1.7) over α for different values of $P \in 2\mathbb{N}$. We choose the degree of smoothness $p = 10$, $\boldsymbol{M} = (64, 64, 128 + P) = \boldsymbol{m}$ and the B-Spline of order 8 as NFFT window function φ in Algorithm 4.3. The short range cutoff is set to $r_{\text{cut}} = 4$ (left) and to $r_{\text{cut}} = 3.5$ (right), respectively.

NFFT without oversampling, i.e., we set $\boldsymbol{m} := \boldsymbol{M}$ in (2.3). In addition, we did the same calculation also with an oversampling factor 2 regarding the non periodic dimension, i.e., we set $\boldsymbol{m} = (M, M, 2 \cdot M_3)$.

For the P^{3}M method, estimates for the rms force error, which also involve the order of the B-spline, have already been derived, see [15]. If no oversampling factor is applied and the cardinal B-spline is chosen as NFFT window function, the structure as well as the performance of the P^{3}M and the P^{2}NFFT method are very similar, see [5]. Thus, within the ScaFaCoS library [1], the same parameter tuning is applied. Setting $r_{\text{cut}} := 4.0$, $M := 16$, choosing the B-spline of order 8 as NFFT window function, as in the last example, and claiming an rms force accuracy of $\approx 2 \cdot 10^{-4}$, the splitting parameter is tuned to $\alpha \approx 0.7186$ in correspondence to [15].

For the cloud wall system of size $N = 300$ we obtained an optimal rms force error of the size $\approx 2 \cdot 10^{-4}$ for 3d- as well as for 2d-periodic boundary conditions choosing $M = 16$ and $P = 8$ (see Figure 4.9). Thus, in the case $N = 300$ we again use the parameters $M = 16$ as well as $P = 8$ and set $r_{\text{cut}} = 4$ in combination with the proposed optimal splitting parameter $\alpha \approx 0.7186$. For the larger systems we also choose larger values of M, where we assume a linear dependence between N and M. The number $P = 8$ of grid points spent for the regularization is kept constant. As already mentioned above, the values for r_{cut} and α are also kept constant, which is reasonable since the different systems have the same particle density.

Note the difference to Example 4.5, where we also increased P with growing M in order to achieve very high accuracies. In the current example we want to keep the accuracy at a constant level, where the number of particles grows. We give numerical evidence that this can be achieved by only increasing the grid size M linearly in N, while the number P of grid points added for the regularization is set to a constant value.

In Table 4.1 it can be seen that we achieve approximation errors of comparable size among all systems, which shows that the parameters were chosen appropriately. For comparison to the 3d-periodic method, we also treated the same particle system under 3d-periodic boundary conditions, where we set $\boldsymbol{M} = \boldsymbol{m} := (M, M, M)$. Thereby, we chose the cardinal B-spline of order 8 and construct regularizations of smoothness $p = 10$. Note that in [5] one can see that the dependency of runtime and accuracy in the P^{3}M method and the non-oversampled P^{2}NFFT with B-Spline window function can be considered as equal.

					$\Delta F_{\mathbb{Z}^2\times\{0\}}$		$\Delta F_{\mathbb{Z}^3}$
N	L	h	M	M_3	$m_3 = 2M_3$	$m_3 = M_3$	
300	10	25	16	40	1.3755e-04	1.3771e-04	1.6261e-04
2400	20	45	32	72	1.5042e-04	1.5115e-04	1.6261e-04
19200	40	85	64	136	1.5674e-04	1.5815e-04	1.6261e-04
153600	80	165	128	264	1.5973e-04	1.6192e-04	1.6261e-04
1228800	160	325	256	520	1.6125e-04	1.6415e-04	1.6261e-04

Table 4.1: Rms force errors in the cloud wall systems under 2d-periodic boundary conditions (with oversampling factor 2 and without oversampling in the third dimension) as well as under 3d-periodic boundary conditions. These errors have been obtained with short range cutoff $r_{\text{cut}} = 4$ and splitting parameter $\alpha \approx 0.7186$. In all computations we spent $P = 8$ grid points for the regularization.

Note that using oversampling in the non periodic dimension only produces insignificantly smaller rms force errors. This is remarkable since the existing error estimates for NFFT based fast summation methods are only valid for oversampling factors greater than 1. This shows the necessity of a new error analysis custom-built for the application discussed in this paper.

In Figure 4.12 we plot the corresponding runtimes. We see that the oversampling slightly increases the runtime and that the 3d-periodic computation requires less computational effort than the 2d-periodic calculation without oversampling, which is due to the differing mesh size regarding the third dimension.

Note that the unexpectedly small increase of runtime due to oversampling results from the optimized support of pruned FFTs of the PFFT software library, see [40] for details. Furthermore, the increased box size h implies that the NFFT can handle the non-periodic

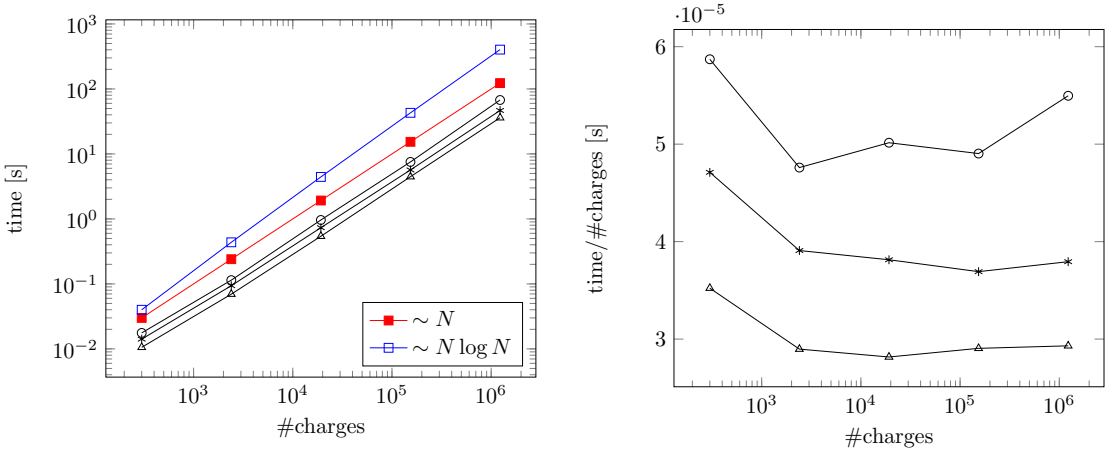

Figure 4.12: Computation times with oversampling factor 2 regarding the non periodic dimension (○) and without oversampling (∗) for the 2d-periodic case as well as for the 3d-periodic computation (△).
left: Attended times for the total computation. We also plot exemplary behaviors where the runtime grows proportional to N (red ■) and $N \log N$ (blue □).
right: Computation time scaled by the number of particles.
We achieved rms force errors of the size $\approx 1.6 \cdot 10^{-4}$.

dimensions more efficiently, which gives an explanation for the unexpectedly small difference in runtime between the 3d-periodic computation and the 2d-periodic calculation without oversampling. However, we skip the details of this NFFT specific optimization and refer to [42, Appendix A] for more details.

In summary, we remark that in contrast to the 3d-periodic case, where the Fourier coefficients are given analytically by (3.5), we have to precompute all the coefficients $\hat{b}_{\boldsymbol{k},l}$ in (4.17). Of course, this leads to a huge amount of precomputation steps for large values of M, which is not included in the stated runtimes. However, if one is interested in doing a large simulation with fixed parameters, where only the particles are moving within a fixed box, all precomputations have to be done only once. □

Example 4.8. This example serves as a comparison between our proposed method and the 2d-periodic spectrally accurate Ewald method [35]. Therefore, we chose the test system given in [35, Sect. 4.3.], i.e., we start with $N = 1000$ uniformly randomly distributed particles $\boldsymbol{x}_j \in [0,1]^3$ located in a cubic box of edge length $L = 1$. The charges are chosen oppositely $q_j = (-1)^j$ such that $\sum_{j=1}^{N} q_j = 0$ and $Q = \sum_{j=1}^{N} q_j^2 = N$. Afterward, we scale up the number of particles in the steps $N = 1000 + 11000n, n = 0, \ldots, 9$. Thereby, we increase the box size at the rate $L = \sqrt[3]{N}$, i.e., we keep the particle density at a constant level. Note that [35, Sect. 4.3.] chose a constant box size $L = 1$ for their tests. However, this only implies a rescaling of the real space cutoff r_{cut} and the Ewald splitting parameter α at rate $\sqrt[3]{N}$ in order to get equivalent numerical results.

In the following, we compute the parameters, achieved rms errors and runtimes of Algorithm 4.3 in order to achieve an rms energy error $\Delta U_{\mathbb{Z}^2 \times \{0\}} \approx 10^{-9}$. Since we have $|q_j| = 1$ the rms energy error as defined in (4.2) coincides with the rms potential error used in [35]. In order to get comparable runtimes we set the real space cutoff $r_{\text{cut}} = 0.62$ as given in [35,

Sect. 4.3.].

At first, we must determine the appropriate Ewald splitting parameter α and a suitable grid size $\boldsymbol{M}$. Therefore, we adopt the parameter tuning given in [35] such that it works with our 3d-periodic NFFT based Ewald summation; see Appendix D for details. Note, that the tuning in Appendix D also gives an easy way to determine the oversampled grid size $\boldsymbol{m}$ and the order of the B-Spline. In essence we can apply the error estimates of [30] if the order of the B-Spline is large enough and we apply a moderate amount of oversampling. Note that the B-Spline order and the oversampling factor $\boldsymbol{m} \odot \boldsymbol{M}^{-1}$ only depend on the accuracy but not on the system size. We found out that the B-spline order 14 in combination with the oversampled grid size $\boldsymbol{m} = 1.23 \cdot \boldsymbol{M}$ is appropriate for the given test case.

Once the parameter set for the 3d-periodic case is given, we can apply the heuristic given in Section 4.3.1 in order to determine the grid size parameters corresponding to the non-periodic dimension. Finally, we must figure out the two parameters that determine the approximation error of the regularization. Hereby, we choose the degree of smoothness p not too small and tune the regularization grid size P such that the rms energy error is well converged. Again, p and P depend only on the accuracy but not on the system size. Therefore we can tune both parameters for the smallest system with $N = 1000$ particles, which results in sufficient accuracy for, e.g., $p = 10$ and $P = 32$.

In summary, the parameter selection scheme presented in Section 4.3.1 becomes:

i) Determine the near field cutoff r_{cut}, the Ewald splitting parameter α, the grid size $\boldsymbol{M}$, the oversampled grid size $\boldsymbol{m}$, and the B-Spline order by the parameter estimates given in Appendix D.
ii) Set the degree of smoothness $p := 10$ and tune the regularization grid size P for the smallest test case with $N = 1000$ particles,
iii) Adjust the grid size M_3 according to (4.23) and apply the periodic oversampling factor to the non-periodic dimension $\boldsymbol{m} = m_1/M_1 \cdot \boldsymbol{M}$.

Table 4.2 shows the parameter sets and the resulting numerical errors for increasing box length L. Compare also to the parameter sets of the 3d-periodic Ewald summation given in Table D.1 in the appendix. We see that the rms potential error $\Delta U_{\mathbb{Z}^2 \times \{0\}}$ is below 10^{-9} as expected. Furthermore, the errors of the 2d-periodic case are comparable to the errors of the 3d-periodic case given in Table D.1. Note that [35] proposed to use 4 times the grid size of the periodic dimension for the non-periodic dimension in order to reach accuracies up to 10 digits. In contrast, our algorithm starts with $m_3/M_1 \approx 3.69$ and converges to $2m_1/M_1 \approx 2.5$ for increasing system size. In addition, we need a small oversampling factor of 1.23 in the periodic dimensions. We stress that the support of the Gaussian window used in [35, Sect. 4.3.] is set to 15. I.e., we get an slightly better localization of our window function although our algorithm does not provide spectral accuracy.

The corresponding runtimes are given in Figure 4.13. In contrast to [35, Sect. 4.3] our measurement include the computation of the short range part and the force computations. We stress that we showed in Table 4.2 that these runtimes are sufficient to reach the required accuracy, while [35, Sect. 4.3] measured the runtimes based on a theoretic parameter selection. We see that the overall run time is almost equal for 2d- and 3d-periodic boundary conditions. In agreement with [35] the run time is dominated by the $\mathcal{O}(N)$ terms in the considered range of system size. The near field computation is slightly faster for the 2d-periodic case. In fact particles at the boundary of the third simulation box dimension have less interacting neighbors due to the open boundary condition. In contrast, the long range part computations are slightly slower of the 2d-periodic case, since the have to spent additional mesh points for

N	L	h	$\boldsymbol{M}$	$\boldsymbol{m}$	$\Delta U_{\mathbb{Z}^2\times\{0\}}$	$\Delta F_{\mathbb{Z}^2\times\{0\}}$
1000	1.0	3.0	(26,26,78)	(32,32,96)	8.59e-10	6.05e-08
12000	2.29	5.68	(54,54,134)	(68,68,166)	4.82e-10	3.45e-08
23000	2.84	6.81	(66,66,158)	(82,82,196)	5.06e-10	3.62e-08
34000	3.24	7.62	(74,74,174)	(92,92,216)	5.14e-10	3.63e-08
45000	3.56	8.15	(82,82,188)	(102,102,232)	5.22e-10	3.69e-08
56000	3.83	8.7	(88,88,200)	(110,110,246)	5.11e-10	3.59e-08
67000	4.06	9.27	(92,92,210)	(114,114,260)	5.11e-10	3.57e-08
78000	4.27	9.5	(98,98,218)	(122,122,270)	5.19e-10	3.95e-08
89000	4.46	9.98	(102,102,228)	(126,126,282)	5.13e-10	4.33e-08
100000	4.64	10.2	(106,106,234)	(132,132,288)	5.23e-10	4.92e-08

Table 4.2: List of parameters and achieved accuracies for randomly distributed particles under 2d-periodic boundary conditions with target accuracy $\Delta U_{\mathbb{Z}^2\times\{0\}} = 10^{-9}$, real space cutoff $r_{\text{cut}} = 0.62$, Ewald splitting parameter $\alpha = 7.489225$, oversampled grid size $\boldsymbol{m} \approx 1.23\boldsymbol{M}$, B-spline order 14, degree of smoothness $p = 10$, and regularization grid size $P = 32$.

regularization and oversampling. Again, the FFT and NFFT are optimized in a way that they ignore unnecessary FFT inputs and outputs that occur in the non-periodic dimensions and due to oversampling; see [40] and [42, Appendix A] for more details. Therefore, the runtimes of the 2d-periodic long range part is less than one may expect from parameter Table 4.2. □

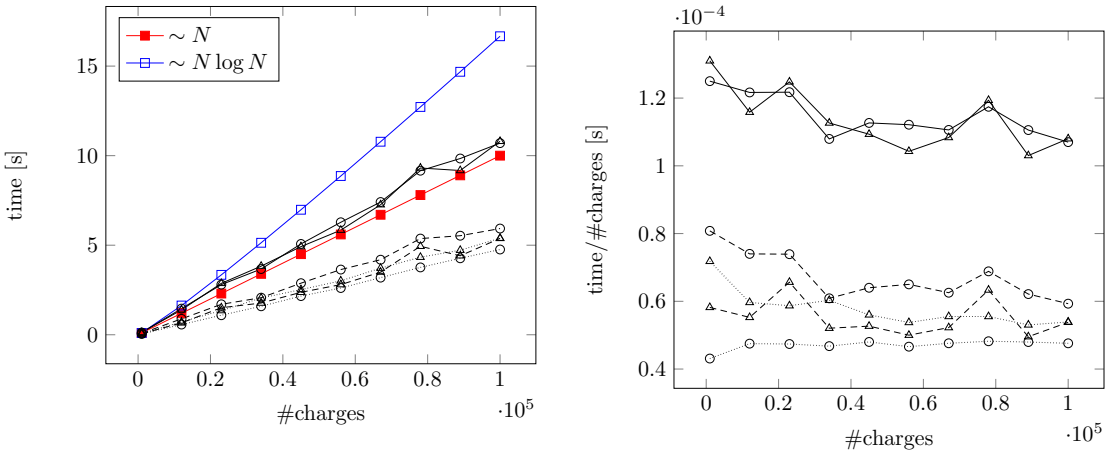

Figure 4.13: Total computation times (solid), as well as computation times of short range parts (dotted), and long range parts (dashed) for the 2d-periodic case (○) and 3d-periodic case (△).
left: Attended times for the total computation. We also plot exemplary behaviors where the runtime grows proportional to N (red ■) and $N \log N$ (blue □).
right: Computation time scaled by the number of particles.
We achieved rms energy errors of the size $\approx 5 \cdot 10^{-10}$ and rms force errors of the size $\approx 4 \cdot 10^{-8}$.

5. Fast Ewald summation for 1d-periodic boundary conditions

5.1. Ewald summation

We consider a system of N charges $q_j \in \mathbb{R}$ at positions $\boldsymbol{x}_j \in L\mathbb{T} \times \mathbb{R}^2$. If periodic boundary conditions are assumed only in the first coordinate we define the potential of each single particle j by

$$\phi^{\mathrm{p1}}(\boldsymbol{x}_j) := \phi_{\mathbb{Z}\times\{0\}^2}(\boldsymbol{x}_j) = \sum_{s=0}^{\infty} \sum_{\substack{\boldsymbol{n}\in\mathbb{Z}\times\{0\}^2 \\ |n_1|=s}} \sum_{i=1}^{N}{}' \frac{q_i}{\|\boldsymbol{x}_{ij} + L\boldsymbol{n}\|} \tag{5.1}$$

and define the Coulomb energy

$$U^{\mathrm{p1}} := U_{\mathbb{Z}\times\{0\}^2} = \frac{1}{2}\sum_{j=1}^{N} q_j \phi^{\mathrm{p1}}(\boldsymbol{x}_j), \tag{5.2}$$

i.e., we set $\mathcal{S} := \mathbb{Z}\times\{0\}^2$ in (1.2) – (1.4) and consider the spherical limit analogously to (3.1). In this section we denote for some $\boldsymbol{y} = (y_1, y_2, y_3) \in \mathbb{R}^3$ the vector of its last two components by $\tilde{\boldsymbol{y}} := (y_2, y_3) \in \mathbb{R}^2$. In the following we denote by

$$\Gamma(s, x) := \int_x^{\infty} t^{s-1}\mathrm{e}^{-t}\mathrm{d}t \tag{5.3}$$

the upper incomplete gamma function. For the case $s = 0$ the well known identity

$$\Gamma(0, x) = -\gamma - \ln x - \sum_{k=1}^{\infty}(-1)^k \frac{x^k}{k!k} \tag{5.4}$$

holds for all positive x, see [2, number 5.1.11]. Thereby, γ is the Euler-Mascheroni constant. The function $\Gamma(0, \cdot)$ is also known as the exponential integral function. We easily see

$$\lim_{x\to 0} \Gamma(0, x) + \ln x + \gamma = 0. \tag{5.5}$$

In the following Theorem, we consider the 1d-Ewald formula, see [43]. In Appendix B we give a proof using convergence factors, analogously to the proof of Theorem 4.1 (see Appendix A).

Theorem 5.1. *Consider an electrical neutral system of N charges $q_j \in \mathbb{R}$ at positions $\boldsymbol{x}_j = (x_{j,1}, \tilde{\boldsymbol{x}}_j) \in L\mathbb{T}\times\mathbb{R}^2$, $j = 1, \ldots, N$. Under periodic boundary conditions in the first variable the potential $\phi^{\mathrm{p1}}(\boldsymbol{x}_j)$, defined in* (5.1)*, can be written as*

$$\phi^{\mathrm{p1}}(\boldsymbol{x}_j) = \phi^{\mathrm{p1,S}}(\boldsymbol{x}_j) + \phi^{\mathrm{p1,L}}(\boldsymbol{x}_j) + \phi^{\mathrm{p1},0}(\boldsymbol{x}_j) + \phi^{\mathrm{p1,self}}(\boldsymbol{x}_j),$$

where for the splitting parameter $\alpha > 0$ we define the short range part

$$\phi^{\mathrm{p1,S}}(\boldsymbol{x}_j) := \sum_{\boldsymbol{n}\in\mathbb{Z}\times\{0\}^2} \sum_{i=1}^{N}{}' q_i \frac{\operatorname{erfc}(\alpha\|\boldsymbol{x}_{ij} + L\boldsymbol{n}\|)}{\|\boldsymbol{x}_{ij} + L\boldsymbol{n}\|}, \tag{5.6}$$

the long range parts

$$\phi^{\mathrm{p1,L}}(\boldsymbol{x}_j) := \frac{2}{L} \sum_{k\in\mathbb{Z}\setminus\{0\}} \sum_{i=1}^{N} q_i \, \mathrm{e}^{2\pi i k(x_{i,1}-x_{j,1})/L} \cdot \Theta^{\mathrm{p1}}(k, \|\tilde{\boldsymbol{x}}_{ij}\|)$$

$$\phi^{\mathrm{p1,0}}(\boldsymbol{x}_j) := -\frac{1}{L} \sum_{\substack{i=1 \\ \|\tilde{\boldsymbol{x}}_{ij}\|\neq 0}}^{N} q_i \left[\gamma + \Gamma(0, \alpha^2\|\tilde{\boldsymbol{x}}_{ij}\|^2) + \ln(\alpha^2\|\tilde{\boldsymbol{x}}_{ij}\|^2)\right],$$

the self potential

$$\phi^{\mathrm{p1,self}}(\boldsymbol{x}_j) := -\frac{2\alpha}{\sqrt{\pi}} q_j \ ,$$

and the function $\Theta^{\mathrm{p1}}(k,r)$ *for* $k, r \in \mathbb{R}$ *is defined by*

$$\Theta^{\mathrm{p1}}(k,r) = \int_0^{\alpha} \frac{1}{z} \mathrm{e}^{\frac{-\pi^2 k^2}{L^2 z^2}} \mathrm{e}^{-r^2 z^2} \mathrm{d}z \,. \tag{5.7}$$

Proof. See Appendix B. ∎

The function $\Theta^{\mathrm{p1}}(k,r)$ can be expressed by the incomplete modified Bessel function of the second kind [24], see Section 5.2.2. This function is known to be infinitely continuously differentiable and, thus, we can construct regularizations of similar structure as (4.12) in order to construct a fast algorithm. In this case the final algorithm requires a smooth bivariate regularization, which can be obtained easily from a one dimensional construction as the Fourier coefficients are radial in $\tilde{\boldsymbol{x}}_{ij}$. Then, the evaluation is done with the multivariate fast summation method [45].

By the following Lemma 5.2 we show that the function $\Theta^{\mathrm{p1}}(k,r)$ for fixed r tends to zero exponentially fast for growing k, which allows the truncation of the infinite sum in $\phi^{\mathrm{p1,L}}(\boldsymbol{x}_j)$. Furthermore, Lemma 5.3 shows that also the kernel in $\phi^{\mathrm{p1,0}}(\boldsymbol{x}_j)$ is a smooth function, which allows the application of the fast summation method. Note that we have $\lim_{x\to\pm\infty} \gamma + \Gamma(0,x^2) + \ln(x^2) = \infty$. Thus, an analytical Fourier transform does not exist, equivalently to the kernel function in the $\boldsymbol{k} = \boldsymbol{0}$ term of the 2d-periodic Ewald sum. However, using the fast summation approach, the function is truncated and embedded in a smooth and periodic function, which does not require localization of the kernel function.

Lemma 5.2. *For arbitrary* $r \in \mathbb{R}$ *we have for the function* Θ^{p1} *given in* (5.7)

$$\Theta^{\mathrm{p1}}(k,r) \to 0 \text{ with } \Theta^{\mathrm{p1}}(k,r) = o(k^{-2}\mathrm{e}^{-k^2}) \text{ for } k \to \infty.$$

Proof. By the definition (5.7) we immediately see

$$\Theta^{\mathrm{p1}}(k,r) \leq \Theta^{\mathrm{p1}}(k,0) = \frac{1}{2}\Gamma\left(0, \frac{\pi^2 k^2}{\alpha^2 L^2}\right).$$

The claim follows by applying the asymptotic expansion $\Gamma(0,x) \approx \frac{\mathrm{e}^{-x}}{x}$, cf. [2, number 6.5.32], which holds for large $x := \frac{\pi^2 k^2}{\alpha^2 L^2}$. ∎

Lemma 5.3. *For the univariate function*

$$\vartheta(x) := \begin{cases} 0 & : x = 0, \\ \Gamma(0, x^2) + \ln(x^2) + \gamma & : \textit{else} \end{cases}$$

we have $\vartheta \in \mathrm{C}^\infty(\mathbb{R})$.

Proof. Since $\lim_{t\to 0} \Gamma(0,t) + \ln(t) + \gamma = 0$ the function is continuous. As (5.4) holds for all $x > 0$ we obtain

$$\gamma + \Gamma(0, x^2) + \ln(x^2) = \sum_{k=1}^{\infty} \frac{(-1)^{k+1} x^{2k}}{k!k}, \quad x \neq 0.$$

From this representation we easily conclude

$$\lim_{x\to+0} \frac{\mathrm{d}^n}{\mathrm{d}x^n} \left(\gamma + \Gamma(0, x^2) + \ln(x^2)\right) = \lim_{x\to-0} \frac{\mathrm{d}^n}{\mathrm{d}x^n} \left(\gamma + \Gamma(0, x^2) + \ln(x^2)\right) \neq \pm\infty.$$

■

5.2. Fast NFFT based algorithm for 1d-periodic systems

Similar as in the previous section we derive the fast algorithm now based on Theorem 5.1. The evaluation of the short range part $\phi^{\mathrm{p1,S}}(\boldsymbol{x}_j)$ is done by a direct evaluation again.

5.2.1. Computational approach

Due to Lemma 5.2 we can truncate the infinite sum in $\phi^{\mathrm{p1,L}}(\boldsymbol{x}_j)$, i.e., for some appropriate $M_1 \in 2\mathbb{N}$ we set

$$\phi^{\mathrm{p1,L}}(\boldsymbol{x}_j) \approx \frac{2}{L} \sum_{k \in \mathcal{I}_{M_1} \setminus \{0\}} \sum_{i=1}^{N} q_i \mathrm{e}^{2\pi \mathrm{i} k x_{ij,1}/L} \Theta^{\mathrm{p1}}(k, \|\tilde{\boldsymbol{x}}_{ij}\|). \tag{5.8}$$

In the following we assume that $\tilde{\boldsymbol{x}}_j \in [-L_2/2, L_2/2] \times [-L_3/2, L_3/2]$, i.e., $\tilde{\boldsymbol{x}}_{ij} \in [-L_2, L_2] \times [-L_3, L_3]$. Thus, the particle distances regarding the non-periodic dimensions $\|\tilde{\boldsymbol{x}}_{ij}\|$ are bounded above by $\sqrt{L_2^2 + L_3^2}$. In the following we choose some $h > 2\sqrt{L_2^2 + L_3^2}$ and accordingly some $\varepsilon \in (0, 1/2)$ such that $\|\tilde{\boldsymbol{x}}_{ij}\| \leq \sqrt{L_2^2 + L_3^2} =: h(1/2 - \varepsilon) < h/2$ for all $i, j = 1, \ldots, N$. For the $k = 0$ term we define

$$\Theta_0^{\mathrm{p1}}(r) := \gamma + \Gamma(0, \alpha^2 r^2) + \ln(\alpha^2 r^2).$$

In order to approximate the long range part $\phi^{\mathrm{p1,L}}(\boldsymbol{x}_j) + \phi^{\mathrm{p1,0}}(\boldsymbol{x}_j)$ efficiently we consider for $k \in \{0, \ldots, M_1/2\}$ the regularizations

$$K_{\mathrm{R}}(k, r) := \begin{cases} \frac{2}{L} \Theta^{\mathrm{p1}}(k, r) & : k \neq 0, |h^{-1} r| \leq 1/2 - \varepsilon, \\ -\frac{1}{L} \Theta_0^{\mathrm{p1}}(r) & : k = 0, |h^{-1} r| \leq 1/2 - \varepsilon, \\ K_{\mathrm{B}}(k, r) & : |h^{-1} r| \in (1/2 - \varepsilon, 1/2], \\ K_{\mathrm{B}}(k, h/2) & : |h^{-1} r| > 1/2, \end{cases}, \tag{5.9}$$

where each function $K_{\mathrm{B}}(k,\cdot):[h/2-h\varepsilon,h/2]\to\mathbb{R}$ is constructed such that $K_{\mathrm{R}}(k,\|\cdot\|):h\mathbb{T}^2\to\mathbb{R}$ is in the Sobolev space $\mathrm{C}^{p-1}(h\mathbb{T}^2)$, i.e., $K_{\mathrm{B}}(k,\cdot)$ fulfills the interpolation conditions

$$\frac{\partial^j}{\partial r^j}K_{\mathrm{B}}(k,h/2-h\varepsilon)=\begin{cases}\frac{2}{L}\frac{\partial^j}{\partial r^j}\Theta^{\mathrm{p1}}(k,h/2-h\varepsilon) & :k\neq 0\\ -\frac{1}{L}\frac{\mathrm{d}^j}{\mathrm{d}r^j}\Theta_0^{\mathrm{p1}}(h/2-h\varepsilon) & :k=0\end{cases}\quad\text{for } j=0,\dots,p-1 \tag{5.10}$$

as well as

$$\frac{\partial^j}{\partial r^j}K_{\mathrm{B}}(k,h/2)=0\quad\text{for } j=1,\dots,p-1. \tag{5.11}$$

Note that $K_{\mathrm{R}}(k,\|\cdot\|)$ is constant for all the points $\{\boldsymbol{y}\in h\mathbb{T}^2:\|\boldsymbol{y}\|\geq h/2\}$. Therefore, the conditions (5.11) ensure smoothness of $K_{\mathrm{R}}(k,\|\cdot\|)$ in the points $\{\boldsymbol{y}\in h\mathbb{T}^2:\|\boldsymbol{y}\|=h/2\}$. Furthermore, (5.11) does not include any restriction on the function value of $K_{\mathrm{R}}(k,h/2)$, since it does not influence the smoothness of $K_{\mathrm{R}}(k,\|\cdot\|)$. In Section C we show how functions $K_{\mathrm{B}}(k,\|.\|)$ can be constructed as polynomials of degree $2p-2$ by a specialized two point Taylor interpolation. By our construction the functions $K_{\mathrm{R}}(k,\|\cdot\|)$ are h-periodic in each direction and smooth, i.e., $K_{\mathrm{R}}(k,\|\cdot\|)\in\mathrm{C}^{p-1}(h\mathbb{T}^2)$. For a graphical illustration of a regularization $K_{\mathrm{R}}(k,\cdot)$ see Figure 5.1.

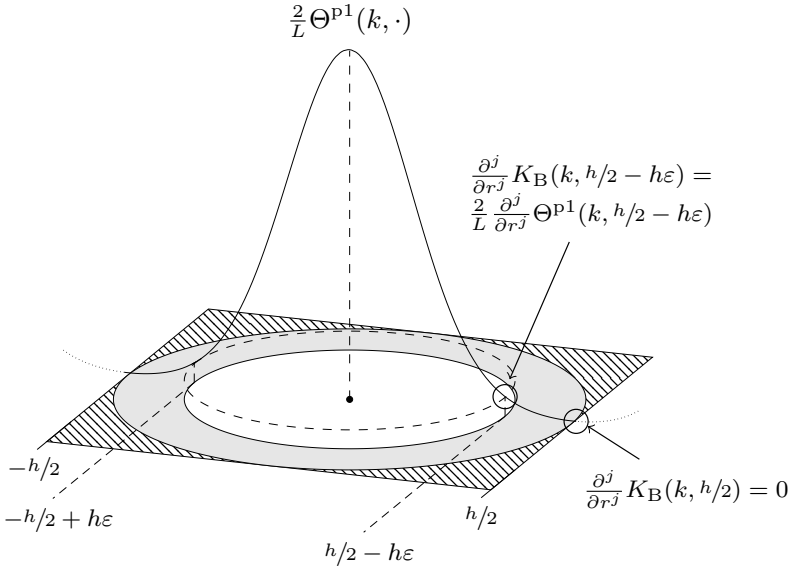

Figure 5.1: Example for $K_{\mathrm{R}}(k,\cdot)$ for $k\geq 1$. Over the gray area the regularization adopts the values of the boundary function $K_{\mathrm{B}}(k,\cdot)$, which we compute via a modified two point Taylor interpolation as derived in Theorem C.2. In the corners (striped area) $K_{\mathrm{R}}(k,\cdot)$ has the constant value $K_{\mathrm{B}}(k,h/2)$. We also marked the points, where the conditions (5.10) and (5.11) are fulfilled.

To this end, we approximate for each $k\in\mathcal{I}_{M_1}\setminus\{0\}$ the function

$$\frac{2}{L}\Theta^{\mathrm{p1}}(k,\|\boldsymbol{y}\|)\approx\sum_{\boldsymbol{l}\in\mathcal{I}_{\tilde{M}}}\hat{b}_{k,\boldsymbol{l}}\mathrm{e}^{2\pi\mathrm{i}\boldsymbol{l}\cdot\boldsymbol{y}/h} \tag{5.12}$$

for $\|\boldsymbol{y}\|\leq h/2-h\varepsilon$ by a trigonometric polynomial. In the case $k=0$ we use the approximation

$$-\frac{1}{L}\Theta_0^{\mathrm{p1}}(\alpha^2\|\boldsymbol{y}\|^2)\approx\sum_{\boldsymbol{l}\in\mathcal{I}_{\tilde{M}}}\hat{b}_{0,\boldsymbol{l}}\mathrm{e}^{2\pi\mathrm{i}\boldsymbol{l}\cdot\boldsymbol{y}/h}. \tag{5.13}$$

Thereby, we choose $\tilde{\boldsymbol{M}} = (M_2, M_3) \in 2\mathbb{N}^2$ large enough and compute the Fourier coefficients $\hat{b}_{k,\boldsymbol{l}}$ by

$$\hat{b}_{k,\boldsymbol{l}} := \frac{1}{|\mathcal{I}_{\tilde{\boldsymbol{M}}}|} \sum_{\boldsymbol{j} \in \mathcal{I}_{\tilde{\boldsymbol{M}}}} K_{\mathrm{R}}\left(k, \|\boldsymbol{j} \odot \tilde{\boldsymbol{M}}^{-1}\| h\right) \mathrm{e}^{-2\pi \mathrm{i} \boldsymbol{j} \cdot (\boldsymbol{l} \odot \tilde{\boldsymbol{M}}^{-1})} \tag{5.14}$$

for all $k \in \mathcal{I}_{M_1}$. In summary we obtain the following approximation for the long range parts

$$\begin{aligned} \phi^{\mathrm{p1,L}}(\boldsymbol{x}_j) + \phi^{\mathrm{p1,0}}(\boldsymbol{x}_j) &\approx \sum_{k \in \mathcal{I}_{M_1}} \sum_{\boldsymbol{l} \in \mathcal{I}_{\tilde{\boldsymbol{M}}}} \hat{b}_{|k|,\boldsymbol{l}} \sum_{i=1}^{N} q_i \mathrm{e}^{2\pi \mathrm{i} k x_{ij,1}/L} \mathrm{e}^{2\pi \mathrm{i} \boldsymbol{l} \cdot \tilde{\boldsymbol{x}}_{ij}/h} \\ &= \sum_{(k,\boldsymbol{l}) \in \mathcal{I}_{\boldsymbol{M}}} \hat{b}_{|k|,\boldsymbol{l}} \left(\sum_{i=1}^{N} q_i \mathrm{e}^{2\pi \mathrm{i} \boldsymbol{v}(k,\boldsymbol{l}) \cdot \boldsymbol{x}_i} \right) \mathrm{e}^{-2\pi \mathrm{i} \boldsymbol{v}(k,\boldsymbol{l}) \cdot \boldsymbol{x}_j}, \end{aligned} \tag{5.15}$$

where we use the truncated Fourier series (5.12), (5.13) in Theorem 5.1 and define $\boldsymbol{M} := (M_1, \tilde{\boldsymbol{M}}) \in 2\mathbb{N}^3$ as well as the vectors $\boldsymbol{v}(k,\boldsymbol{l}) := (k/L, \boldsymbol{l}/h) \in L^{-1}\mathbb{Z} \times h^{-1}\mathbb{Z}^2$.

The expressions in the inner brackets

$$\hat{S}(k,\boldsymbol{l}) := \sum_{i=1}^{N} q_i \mathrm{e}^{2\pi \mathrm{i} \boldsymbol{v}(k,\boldsymbol{l}) \cdot \boldsymbol{x}_i}, \quad (k,\boldsymbol{l}) \in \mathcal{I}_{\boldsymbol{M}} \tag{5.16}$$

can be computed by an NFFT$^{\mathrm{H}}$. This will be followed by $|\mathcal{I}_{\boldsymbol{M}}|$ multiplications with $\hat{b}_{|k|,\boldsymbol{l}}$ and completed by an NFFT to compute the outer summation with the complex exponentials. The proposed evaluation of $\phi^{\mathrm{p1,L}}(\boldsymbol{x}_j) + \phi^{\mathrm{p1,0}}(\boldsymbol{x}_j)$ at the points $\boldsymbol{x}_j$, $j = 1, \ldots, N$, requires $\mathcal{O}(N + |\mathcal{I}_{\boldsymbol{M}}| \log |\mathcal{I}_{\boldsymbol{M}}|)$ arithmetic operations.

For the calculation of the forces we set $\mathcal{S} := \mathbb{Z} \times \{0\}^2$, define $\boldsymbol{F}^{\mathrm{p1}}(\boldsymbol{x}_j) := \boldsymbol{F}_{\mathcal{S}}(\boldsymbol{x}_j)$ via (1.4) and calculate the short range portions $\boldsymbol{F}^{\mathrm{p1,S}}(\boldsymbol{x}_j)$, as defined in (3.7), by a direct summation. In the long range part we can either use the i$\boldsymbol{k}$ approach, i.e., we set

$$\boldsymbol{F}^{\mathrm{p1,L}}(\boldsymbol{x}_j) + \boldsymbol{F}^{\mathrm{p1,0}}(\boldsymbol{x}_j) \approx 2\pi \mathrm{i} q_j \sum_{(k,\boldsymbol{l}) \in \mathcal{I}_{\boldsymbol{M}}} \hat{b}_{|k|,\boldsymbol{l}} \left(\sum_{i=1}^{N} q_i \mathrm{e}^{2\pi \mathrm{i} \boldsymbol{v}(k,\boldsymbol{l}) \cdot \boldsymbol{x}_i} \right) \boldsymbol{v}(k,\boldsymbol{l}) \mathrm{e}^{-2\pi \mathrm{i} \boldsymbol{v}(k,\boldsymbol{l}) \cdot \boldsymbol{x}_j}, \tag{5.17}$$

or the analytic differentiation, cf. (3.9).

In summary, we obtain Algorithm 4.3 for the fast computation of 1d-periodic Coulomb interactions.

Algorithm 5.4 (1d-periodic P^{2}NFFT)**.**

Input: *Positions $\boldsymbol{x}_j \in L\mathbb{T} \times [-L_2/2, L_2/2] \times [-L_3/2, L_3/2]$, charges $q_j \in \mathbb{R}$ $(j = 1, \ldots, N)$, splitting parameter $\alpha > 0$, short range cutoff $r_{\mathrm{cut}} > 0$, long range cutoff $\boldsymbol{M} = (M_1, \tilde{\boldsymbol{M}}) \in 2\mathbb{N}^3$, regularization parameter $\varepsilon > 0$, degree of smoothness $p \in \mathbb{N}$.*

0.) Precomputations:

- *a) Set $h := (1/2 - \varepsilon)^{-1} \sqrt{L_2^2 + L_3^2}$.*
- *b) Construct the regularization* (5.9) *for each $k \in \{0, \ldots, M_1/2\}$.*
- *c) Compute the Fourier coefficients* (5.14)*.*

1.) Compute the short range parts of the potentials $\phi^{\mathrm{p1,S}}(\boldsymbol{x}_j)$ and the short range parts of the forces $\boldsymbol{F}^{\mathrm{p1,S}}(\boldsymbol{x}_j)$ by direct evaluation, i.e., restrict the summation in (5.6) *and* (3.7)*, where $\mathcal{S} := \mathbb{Z} \times \{0\}^2$, to all $\|\boldsymbol{x}_{ij} + L\boldsymbol{n}\| \leq r_{\mathrm{cut}}$.*

2.) Compute the sums $\hat{S}(k, \boldsymbol{l})$ *in* (5.16) *by the adjoint NFFT* (2.4).
3.) Apply the NFFT (2.2) *to compute the long range parts of the potentials* $\phi^{\mathrm{p1,L}}(\boldsymbol{x}_j) + \phi^{\mathrm{p1,0}}(\boldsymbol{x}_j)$ *by* (5.15).
4.) Compute the long range parts of the forces $\boldsymbol{F}^{\mathrm{p1,L}}(\boldsymbol{x}_j) + \boldsymbol{F}^{\mathrm{p1,0}}(\boldsymbol{x}_j)$ *via the* $i\boldsymbol{k}$ *differentiation approach* (5.17) *or the analytic differentiation, cf.* (3.9).
5.) For all $j = 1, \ldots, N$ *compute*

$$\begin{aligned}\phi^{\mathrm{p1}}(\boldsymbol{x}_j) &= \phi^{\mathrm{p1,S}}(\boldsymbol{x}_j) + \phi^{\mathrm{p1,L}}(\boldsymbol{x}_j) + \phi^{\mathrm{p1,0}}(\boldsymbol{x}_j) + \phi^{\mathrm{p1,self}}(\boldsymbol{x}_j)\\ \boldsymbol{F}^{\mathrm{p1}}(\boldsymbol{x}_j) &= \boldsymbol{F}^{\mathrm{p1,S}}(\boldsymbol{x}_j) + \boldsymbol{F}^{\mathrm{p1,L}}(\boldsymbol{x}_j) + \boldsymbol{F}^{\mathrm{p1,0}}(\boldsymbol{x}_j).\end{aligned}$$

6.) Compute the total energy (5.2) *and set* $U^{\mathrm{p1}}(\boldsymbol{x}_j) := q_j \phi^{\mathrm{p1}}(\boldsymbol{x}_j)$.
Output: *Total energy* U^{p1}*, single energies* $U^{\mathrm{p1}}(\boldsymbol{x}_j)$ *and forces* $\boldsymbol{F}^{\mathrm{p1}}(\boldsymbol{x}_j)$.

Remark 5.5. Algorithm 5.4 has the same structure as the NFFT based method for 3d-periodic systems, cf. Section 3. Thus, we also obtain a matrix vector notation of the form (3.6) for the approximation of $\phi^{\mathrm{p1,L}}(\boldsymbol{x}_j) + \phi^{\mathrm{p1,0}}(\boldsymbol{x}_j)$. In other words, we use the same algorithm, where we replace the Fourier coefficients $\hat{b}_{\boldsymbol{k}}$ from (3.5) by the new coefficients $\hat{b}_{|k|,\boldsymbol{l}}$ in (5.14) and insert the nodes $(x_{ij,1}/L, \tilde{\boldsymbol{x}}_{ij}/h) \in \mathbb{T}^3$ instead of $\boldsymbol{x}_{ij}/L \in \mathbb{T}^3$ into the NFFT algorithms. □

5.2.2. Implementation details

The precomputation step of Algorithm 5.4 includes the construction of the regularizations (5.9). Thereby, we obtain $K_{\mathrm{B}}(k, \cdot)$ by the unique polynomial of degree $2p-2$ that fulfills the $2p-1$ interpolation conditions (5.10) – (5.11). An explicit representation of this polynomial is given by Theorem C.2 in the appendix, where we set $m = h(1/2 - \varepsilon/2)$, $r = h\varepsilon/2$ and a_j, b_j equal to the right hand side of the interpolation conditions (5.10) – (5.11), respectively. In order to compute the derivatives in (5.10) – (5.11) we use the following relations. At first, we consider the function $\Theta^{\mathrm{p1}}(k, r)$ as defined in (5.7) and show that it can be expressed in terms of an incomplete modified Bessel function of the second kind [24] defined by

$$K_\nu(x, y) := \int_1^\infty t^{-\nu-1} \mathrm{e}^{-xt - y/t} \mathrm{d}t, \quad \nu \in \mathbb{R}, x \geq 0, y \geq 0.$$

Indeed, with the substitution $t = \alpha^2/z^2$ in (5.7) we get

$$\Theta^{\mathrm{p1}}(k, r) = \int_0^\alpha \frac{1}{z} \mathrm{e}^{\frac{-\pi^2 k^2}{L^2 z^2}} \mathrm{e}^{-r^2 z^2} \mathrm{d}z \overset{t=\alpha^2/z^2}{=} \frac{1}{2} \int_1^\infty t^{-1} \mathrm{e}^{-\frac{\pi^2 k^2}{\alpha^2 L^2} t - \alpha^2 r^2 t^{-1}} \mathrm{d}t = \frac{1}{2} K_0\left(\frac{\pi^2 k^2}{\alpha^2 L^2}, \alpha^2 r^2\right).$$

Note that the relation [24]

$$\frac{\partial K_\nu(x, y)}{\partial y} = -K_{\nu+1}(x, y) \tag{5.18}$$

gives an easy way to compute the necessary partial derivatives. In the following Lemma 5.6 we give a formula for the partial derivatives of $K_0(x, y^2)$ with respect to y, which are needed for the differentiation of the function $\Theta^{\mathrm{p2}}(k, \cdot)$.

Lemma 5.6. *For $x \in \mathbb{R}$ fixed and $k \in \mathbb{N}_0$ we have*

$$\frac{\partial^{2k}}{\partial y^{2k}} K_0(x, y^2) = \sum_{l=0}^{k} \alpha_{k,l} K_{k+l}(x, y^2) y^{2l} \tag{5.19}$$

$$\frac{\partial^{2k+1}}{\partial y^{2k+1}} K_0(x, y^2) = \sum_{l=0}^{k} \beta_{k,l} K_{k+1+l}(x, y^2) y^{2l+1}, \tag{5.20}$$

where the coefficients $\alpha_{k,l}$ and $\beta_{k,l}$ are given recursively by

$$\alpha_{0,0} = 1$$

$$\beta_{k,l} = \begin{cases} -2\alpha_{k,k} & : l = k \\ -2\alpha_{k,l} + 2(l+1)\alpha_{k,l+1} & : else \end{cases}$$

$$\alpha_{k,l} = \begin{cases} \beta_{k-1,0} & : k \geq 1, l = 0 \\ -2\beta_{k-1,l-1} & : k \geq 1, l = k \\ -2\beta_{k-1,l-1} + (2l+1)\beta_{k-1,l} & : k \geq 1, else. \end{cases}$$

Proof. Apply the chain rule and relation (5.18). The claim follows by induction in k. ∎

Note that we can precompute the expressions of the derivatives of the function $K_\nu(x, \cdot^2)$ with Lemma 5.6 up to a sufficiently high order. So, we do not have to compute them recursively, which is better in terms of cost of the precomputation step.

Unfortunately, the evaluation of the incomplete Bessel function K_ν poses several numerical difficulties and publicly available implementations are rare. In the following, we show how we accomplished the sufficiently accurate evaluation. We started with the iterative algorithm given in [47] for the computation of the incomplete modified Bessel function of the second kind $K_\nu(x, y)$ for arbitrary order $\nu \in \mathbb{R}$. In our algorithm, we evaluate this function with an absolute accuracy of $\epsilon = 10^{-15}$. However, this iteration gets numerical problems for large values of x and y due to the exponential damping within the integral. Therefore, we compute the following upper bounds on $K_\nu(x, y)$ and assume $K_\nu(x, y)$ to be numerically equal to zero whenever one of these bounds is already very small. A first upper bound is given by

$$K_\nu(x, y) \leq \int_1^\infty \frac{\mathrm{e}^{-xt}}{t^{\nu+1}} \mathrm{d}t = \frac{1}{x^\nu} \Gamma(-\nu, x). \tag{5.21}$$

For $x < y$ it was suggested [47] to evaluate the faster convergent complement integral

$$K_\nu(x, y) = 2(x/y)^{\nu/2} K_\nu(2\sqrt{xy}) - K_{-\nu}(y, x), \tag{5.22}$$

where the (complete) modified Bessel function of the second kind $K_\nu(\cdot)$ is defined by

$$K_\nu(z) := \frac{1}{2} \int_0^\infty \frac{\mathrm{e}^{-z/2(t+1/t)}}{t^{\nu+1}} \mathrm{d}t,$$

cf. [24]. By (5.22) we obtain another upper bound for $K_\nu(x, y)$ in the case $x < y$, namely,

$$K_\nu(x, y) < 2(x/y)^{\nu/2} K_\nu(2\sqrt{xy}) < 2K_\nu(2\sqrt{xy}) \tag{5.23}$$

This gives often a better estimate than (5.21) as it depends also on y.

Another numerical difficulty appears in (5.14) for $k \neq 0$ when K_{R} must be evaluated near the origin. This corresponds to the evaluation of $K_0(x, y)$ with small x and y, where the evaluation of the function is numerically demanding and the accuracy ϵ can not always be achieved. However, we have

$$\left.\frac{\partial^n K_0(x,y)}{\partial y^n}\right|_{y=0} = (-1)^n K_n(x,0) = (-1)^n x^n \int_x^\infty \mathrm{e}^{-t} t^{-n-1} \mathrm{d}t = (-1)^n x^n \Gamma(-n, x) \tag{5.24}$$

with the upper incomplete gamma function Γ, as defined in (5.3). Therewith, we obtain for fixed x and $m \in \mathbb{N}$

$$K_0(x,y) = \sum_{n=0}^{m} \frac{(-1)^n}{n!} x^n \Gamma(-n, x) y^n + R_m K_0(x, 0)$$

where for some $0 < \xi < 1$

$$R_m K_0(x,0) = \frac{(-1)^{m+1} K_{m+1}(x, \xi y)}{(m+1)!} y^{m+1}.$$

Applying (5.21) we compute the upper bound

$$|R_m K_0(x,0)| \leq \frac{K_{m+1}(x,0) y^{m+1}}{(m+1)!} \leq \frac{\mathrm{e}^{-x} y^{m+1}}{(m+1)! x}.$$

Thus, for x and y small we calculate the value of the truncated Taylor series in (5.24), where we choose m large enough to fulfill $|R_m K_0(x,0)| < \epsilon$.

In order to compute the Fourier coefficients $\hat{b}_{0,l}$, we also have to evaluate the functions $\Gamma(0, \alpha^2 r^2)$ and $\ln(\alpha^2 r^2)$ as well as their derivatives. In the following Lemma we show how the derivatives of $\Gamma(0, x^2)$ can be computed recursively.

Lemma 5.7. *For $k \in \mathbb{N}$ we have*

$$\frac{\mathrm{d}^{2k}}{\mathrm{d}x^{2k}} \Gamma(0, x^2) = 2\mathrm{e}^{-x^2} \left(\sum_{l=1}^{k} \frac{(2k-1)!}{(k-l)!} x^{-2l} + p_k(x) \right) \tag{5.25}$$

$$\frac{\mathrm{d}^{2k+1}}{\mathrm{d}x^{2k+1}} \Gamma(0, x^2) = -2\mathrm{e}^{-x^2} \left(\sum_{l=0}^{k} \frac{(2k)!}{(k-l)!} x^{-(2l+1)} + q_k(x) \right) \tag{5.26}$$

where p_k and q_k are polynomials of degree $2k-2$ and $2k-1$, respectively, fulfilling the recursion

$$\begin{aligned} p_1(x) &= 2 \\ q_k(x) &= 2x p_k(x) - \frac{\mathrm{d}}{\mathrm{d}x} p_k(x) \\ p_{k+1}(x) &= 2x q_k(x) - \frac{\mathrm{d}}{\mathrm{d}x} q_k(x) + \frac{2(2k)!}{k!}. \end{aligned}$$

Proof. Induction in $k \in \mathbb{N}$. ∎

Again, in order to save time within the precomputation step we can use this recursion in combination with a computer algebra system in order to precompute the analytic expressions of the derivatives of $\Gamma(0, \cdot^2)$ up to a sufficient order.

5.3. Numerical Results

In this section we present numerical results of our algorithm for 1d-periodic systems. We set up the tests analogously to the 2d-periodic case, see Section 4.3 for details.

5.3.1. Parameter Choice

In our numerical experiments in the 1d-periodic setting we will also only consider test cases, where the charges are located in a cubic box $[-L/2, L/2]^3$. The heuristic parameter choice from the 2d-periodic case from Section 4.3.1 is adapted as follows.

We denote by $M := M_1 \in 2\mathbb{N}$ the cutoff length in the long range part of the Ewald formulas, see (5.8). The box size regarding the non periodic dimension can be implicitly expressed by $h = 2\sqrt{2}L + 2h\varepsilon$, where $2h\varepsilon$ is the sum of the lengths of the two segments at the boundaries, which are added for the regularization. Based on this, we set $\tilde{\boldsymbol{M}} = (M_2, M_3) \in 2\mathbb{N}$ in (5.12) and (5.13) to

$$M_2 = M_3 := 2\left\lceil \sqrt{2}M \right\rceil + P \text{ with } P \in 2\mathbb{N}, \tag{5.27}$$

where the brackets denote that we round to the next integer value. Having defined P, the corresponding value for ε is given by

$$\varepsilon = \frac{1}{2}\frac{P}{2\left\lceil \sqrt{2}M \right\rceil + P} = \frac{P}{2M_3}$$

and $h = (1/2 - \varepsilon)^{-1}\sqrt{2}L = \frac{2\lceil \sqrt{2}M \rceil + P}{M} \cdot L$. Finally, we apply the same oversampling factor as for the periodic dimensions, i.e., we set $m_2 = m_3 = \frac{m}{M} M_3$.

The parameter selection can be summarized in the following three easy steps:

i) Determine the near field cutoff r_{cut}, the Ewald splitting parameter α, the grid size $\boldsymbol{M}$, the oversampled grid size $\boldsymbol{m}$, and the B-Spline order by any parameter estimates suitable for the 3d-periodic case, e.g., [15].

ii) Set the degree of smoothness p not too small (in our tests $p := 10$ is sufficient) and tune the regularization grid size P for a small test case with a low number of particles N.

iii) Compute the grid size (M_2, M_3) according to (5.27) and apply the periodic oversampling factor to the non-periodic dimensions, i.e., $\boldsymbol{m} = m_1/M_1 \cdot \boldsymbol{M}$.

Again, only the regularization grid size P needs some tuning, while all other parameters are either known from the 3d-periodic case or can be computed easily.

5.3.2. Examples

Example 5.8. As in Example 4.5 we consider the cloud wall system with $N = 300$ charged particles and compute the energies as well as the forces subject to 1d-periodic boundary conditions. Again, in order to get an impression of the involved functions we plot $\Theta^{\text{p1}}(1, \cdot)$ as well as $\Theta_0^{\text{p1}}(\cdot)$ over the interval $[-L, L]$ for different splitting parameters α, see Figure 5.2.

The number of grid points P, which are spent for the regularization domain are set according to the corresponding 2d-periodic example, see Figure 4.9 for the results. In this example, we choose the parameter P as follows.

$$P := 2\left\lceil \sqrt{2} \cdot \tfrac{P_{\text{p2}}}{2} \right\rceil \approx \sqrt{2} \cdot P_{\text{p2}}, \tag{5.28}$$

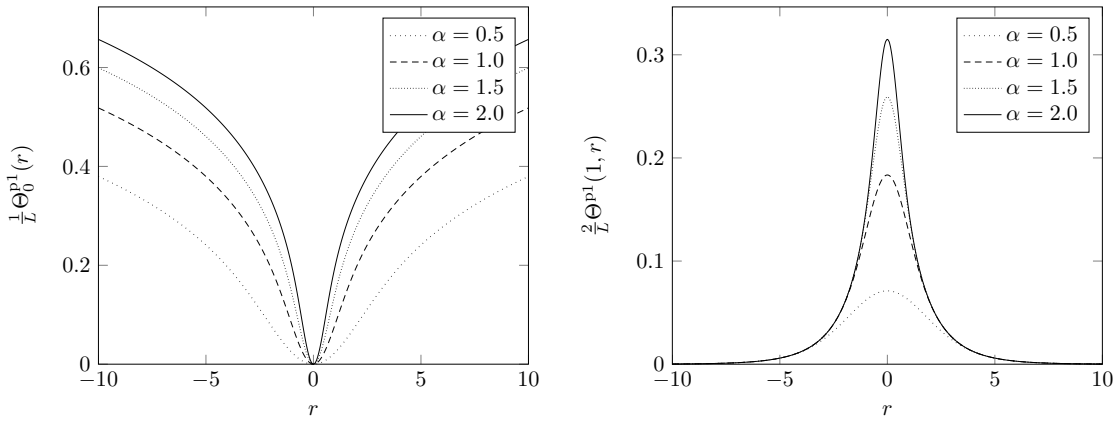

Figure 5.2: $\Theta_0^{\mathrm{p1}}(r)$ and $\Theta^{\mathrm{p1}}(1, r)$ with $L = 10$ for different splitting parameters α.

where we denote by P_{p2} the corresponding value for P, which we used for the 2d-periodic computation. In the 2d-periodic case we set $P = 30$ in the case $M = 64$, where we constructed regularizations of smoothness $p = 10$. For the 1d-periodic computations we set

$$P := 2\left\lceil \sqrt{2} \cdot \tfrac{30}{2} \right\rceil = 42 \text{ and } M_2 = M_3 := 224.$$

In Figure 5.3 we compare the corresponding rms force error for some values of P. Indeed, we see that for the 1d-periodic setting the optimal rms force error is achieved for $P \approx 42$. Thus, the proposed choice of $M_2 = M_3$ as well as P seems reasonable.

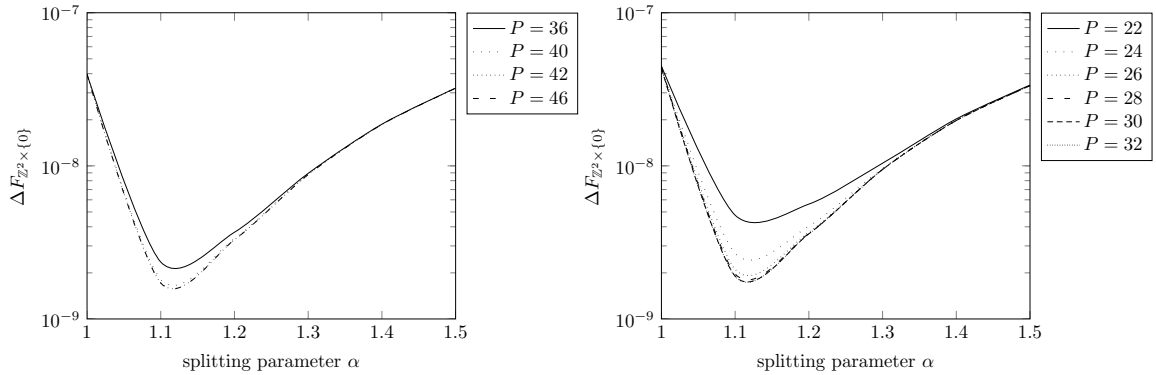

Figure 5.3: The rms force error (1.7) over α for different values of $P \in 2\mathbb{N}$. We choose the short range cutoff $r_{\mathrm{cut}} = 4$, the smoothness $p = 10$ and the B-Spline of order 8 as NFFT window function φ. We plot the results of the 1d-periodic case, where we set $\boldsymbol{m} = \boldsymbol{M} = (64, M_2, M_3)$ via (5.27), (left) as well as of the 2d-periodic computation, where we set $\boldsymbol{m} = \boldsymbol{M} = (64, 64, M_3)$ via (4.23) (right). (Test case: cloud wall system, $N = 300$.)

In Figure 5.4 we plot the rms force error $\triangle F_{\mathbb{Z}\times\{0\}^2}$ with respect to the splitting parameter α for different long range cutoffs $\boldsymbol{M} = (M, M_2, M_3) \in 2\mathbb{N}^3$, where we define M_2 and M_3 by (5.27) as well as P by (5.28) based on our results for the 2d-periodic case.

On the right hand side we see the corresponding errors produced by the 3d-periodic computation. With the chosen parameters we obtain rms errors comparable to the 3d-periodic case for $M \in \{16, 32, 64, 128\}$, where we do not need an oversampling in the non periodic dimensions. Unfortunately, for $M = 256$ we could not reach the accuracy of the 3d-periodic algorithm. This may be due to the numerically complicated evaluation of the incomplete modified Bessel function in the precomputation step. □

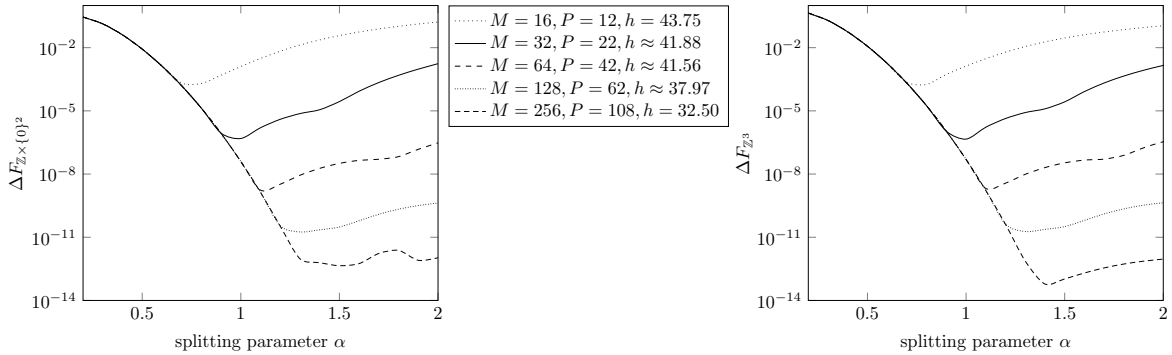

Figure 5.4: The rms force error (1.7) over α for different FFT sizes. We choose the short range cutoff $r_{\text{cut}} = 4$, $p = 10$, $\boldsymbol{m} = \boldsymbol{M} = (M, M_2, M_3)$ via (5.27) and the B-Spline of order 8 as NFFT window function φ in Algorithm 5.4. We plot the results of the 1d-periodic (left) as well as of the 3d-periodic computation (right).

Example 5.9. We apply our Algorithm to the particle systems we already considered in Example 4.7. Equivalently, we set $r_{\text{cut}} = 4$ and $\alpha \approx 0.7186$ in correspondence to [15]. For the computation with $N = 300$ particles we set $M = 16$ and use $P = 12$ grid points for the regularization, which corresponds to setting $\varepsilon \approx 0.103448$.

As the particle systems have the same particle density we keep the short range cutoff r_{cut} and the splitting parameter α fixed and again increase the value of M linearly in N. The parameter $P = 12$ is used for all particle systems.

The obtained errors can be found in Table 5.1. Again, we computed the errors produced by Algorithm 5.4 without as well as with oversampling in the non-periodic dimensions, where we set the oversampling factor to 2, i.e., $\boldsymbol{m} := (M, 2M_2, 2M_3)$. In Figure 5.5 we plot the corresponding runtimes. Note that the number of grid points depends linearly on N. Since the regularization grid size P is kept constant and the rms errors stay at a constant level, our method scales like $\mathcal{O}(N \log N)$. The unexpected increase of runtime for $N = 256$ results from the limitation to 8 GB main memory of the test machine. Again, the FFT and NFFT are optimized in a way that they ignore unnecessary FFT inputs and outputs that occur in the non-periodic dimensions; see [40] and [42, Appendix A] for more details. Therefore, the runtimes of the 1d-periodic P^{2}NFFT is less than one may expect. □

Example 5.10. As in Example 4.8 we consider a set of increasing systems of randomly distributed particles with charges $q_j \in \{-1, 1\}$ and compute the energies as well as the forces subject to 1d-periodic boundary conditions.

In the following, we compute the parameters, achieved rms errors and runtimes of Algorithm 4.3 in order to achieve an rms energy error $\Delta U_{\mathbb{Z}^2\times\{0\}} \approx 10^{-9}$. Since we have $|q_j| = 1$

N	L	$2\sqrt{2}L$	h	M	$M_{2/3}$	$\Delta F_{\mathbb{Z}\times\{0\}^2}$ $m_{2/3}=2M_{2/3}$	$\Delta F_{\mathbb{Z}\times\{0\}^2}$ $m_{2/3}=M_{2/3}$	$\Delta F_{\mathbb{Z}^3}$
300	10	28.28	36.25	16	58	1.2979e-04	1.7382e-04	1.6261e-04
2400	20	56.57	63.75	32	102	1.4587e-04	1.6804e-04	1.6261e-04
19200	40	113.14	121.25	64	194	1.5229e-04	1.5873e-04	1.6261e-04
153600	80	226.27	233.75	128	374	1.5757e-04	1.6269e-04	1.6261e-04
1228800	160	452.55	460.00	256	736	1.5951e-04	1.6242e-04	1.6261e-04

Table 5.1: Rms force errors in the cloud wall systems under 1d-periodic boundary conditions (with oversampling factor 2 and without oversampling in the two non periodic dimensions) as well as under 3d-periodic boundary conditions. These errors have been obtained with short range cutoff $r_{\text{cut}} = 4$ and splitting parameter $\alpha \approx 0.7186$. In all computations we spent $P = 12$ grid points for the regularization.

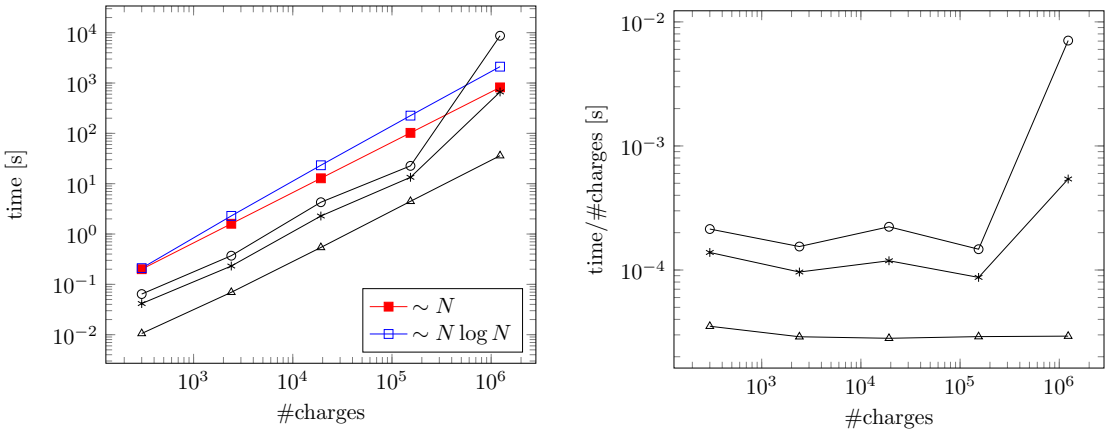

Figure 5.5: Computation times with oversampling factor 2 regarding the non periodic dimensions (○) and without oversampling (∗) for the 1d-periodic case as well as for the 3d-periodic computation (△).
left: Attended times for the total computation. We also plot exemplary behaviors where the runtime grows proportional to N (red ■) and $N \log N$ (blue □).
right: Computation time scaled by the number of particles.
We achieved rms force errors of the size $\approx 1.6 \cdot 10^{-4}$.

the rms energy error as defined in (4.2) coincides with the rms potential error used in [35]. In order to get comparable runtimes we set the real space cutoff $r_{\text{cut}} = 0.62$ as given in [35, Sect. 4.3.].

Now, the parameter selection scheme presented in Section 5.3.1 becomes:

i) Determine the near field cutoff r_{cut}, the Ewald splitting parameter α, the grid size $\boldsymbol{M}$, the oversampled grid size $\boldsymbol{m}$, and the B-Spline order by the parameter estimates given in Appendix D.

ii) Set the degree of smoothness $p := 10$ and tune the regularization grid size P for the smallest test case with $N = 1000$ particles,

iii) Adjust the grid size (M_2, M_3) according to (5.27) and apply the periodic oversampling factor to the non-periodic dimensions $\boldsymbol{m} = m_1/M_1 \cdot \boldsymbol{M}$.

N	L	h	$\boldsymbol{M}$	$\boldsymbol{m}$	$\Delta U_{\mathbb{Z}\times\{0\}^2}$	$\Delta F_{\mathbb{Z}\times\{0\}^2}$
1000	1.0	4.15	(26,108,108)	(32,134,134)	8.41e-10	5.94e-08
12000	2.29	7.8	(54,184,184)	(68,228,228)	6.11e-10	4.08e-08
23000	2.84	9.39	(66,218,218)	(82,270,270)	5.72e-10	3.81e-08
34000	3.24	10.6	(74,242,242)	(92,298,298)	5.95e-10	3.85e-08
45000	3.56	11.3	(82,260,260)	(102,320,320)	6.48e-10	4.17e-08
56000	3.83	12.0	(88,276,276)	(110,340,340)	6.59e-10	4.23e-08
67000	4.06	12.8	(92,290,290)	(114,358,358)	6.52e-10	4.17e-08
78000	4.27	13.3	(98,304,304)	(122,374,374)	6.30e-10	4.34e-08
89000	4.46	13.8	(102,316,316)	(126,390,390)	6.24e-10	4.72e-08
100000	4.64	14.3	(106,326,326)	(132,402,402)	6.32e-10	5.26e-08

Table 5.2: List of parameters and achieved accuracies for randomly distributed particles under 1d-periodic boundary conditions with target accuracy $\Delta U_{\mathbb{Z}\times\{0\}^2} = 10^{-9}$, real space cutoff $r_{\text{cut}} = 0.62$, Ewald splitting parameter $\alpha = 7.489225$, and oversampled grid size $\boldsymbol{m} \approx 1.23\boldsymbol{M}$, B-spline order 14, degree of smoothness $p = 10$, and regularization grid size $P = 44$.

Table 5.2 shows the parameter sets and the resulting numerical errors for increasing box length L. Compare also to the parameter sets of the 3d-periodic Ewald summation given in Table D.1 in the appendix. We see that the rms potential error $\Delta U_{\mathbb{Z}^2\times\{0\}}$ is below 10^{-9} as expected. Furthermore, the errors of the 1d-periodic case are comparable to the errors of the 3d-periodic case given in Table D.1. In contrast to the 2d-periodic case, our algorithm starts with larger $m_3/M_1 \approx 5.15$ and converges to $2\sqrt{2}m_1/M_1 \approx 3.5$ for increasing system size. Again, we need a small oversampling factor of 1.23 in the periodic dimension.

The corresponding runtimes are given in Figure 5.6. Again our measurement include the computation of the short range part and the force computations. We see that the overall run time is comparable for 1d- and 3d-periodic boundary conditions. However, the 1d-periodic run time is dominated by the $\mathcal{O}(N \log N)$ long range computations. Note that the jumps in the run time of the long range computations is due to the increased FFT run time (but still $\mathcal{O}(N \log N)$) whenever $\boldsymbol{m}$ is not factorizable into small prime factors. The near field computation is slightly faster for the 1d-periodic case. In fact particles at the boundary of the second and third simulation box dimension have less interacting neighbors due to the open boundary conditions. In contrast, the long range part computations are more demanding for the 1d-periodic case, since the have to spent additional mesh points for regularization and oversampling. Again, the FFT and NFFT are optimized in a way that they ignore unnecessary FFT inputs and outputs that occur in the non-periodic dimensions and due to oversampling; see [40] and [42, Appendix A] for more details. Therefore, the runtimes of the 1d-periodic long range part is less than one may expect from parameter Table 5.2. □

6. Conclusion

In this paper we proposed new fast algorithms for the computation of the energies and the forces in three-dimensional particle systems subject to 2d- and 1d-periodic boundary conditions. These algorithms are based on the Ewald summation formulas, which we combined with the NFFT based fast summation method. Therefore, we obtain the same structure as

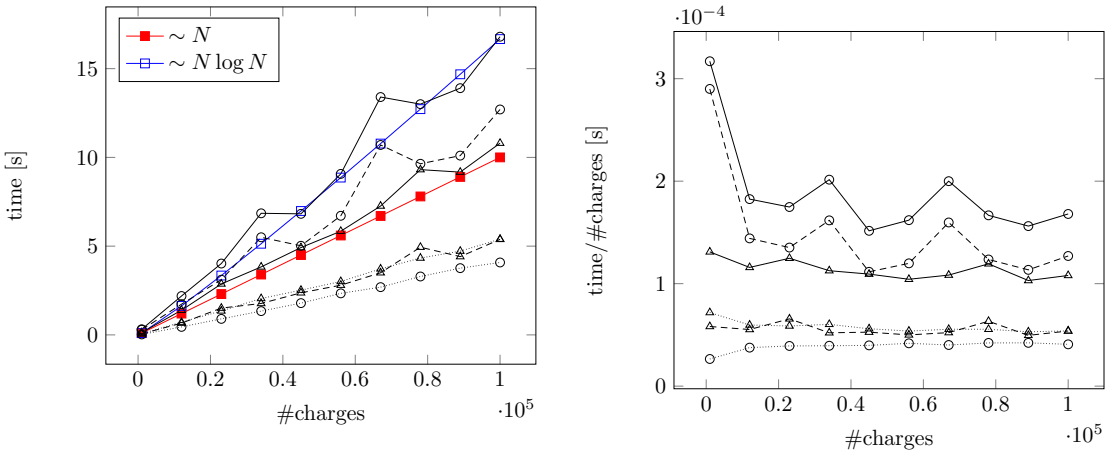

Figure 5.6: Total computation times (solid), as well as computation times of short range parts (dotted), and long range parts (dashed) for the 1d-periodic case (o) and 3d-periodic case (△).
left: Attended times for the total computation. We also plot exemplary behaviors where the runtime grows proportional to N (red ■) and $N \log N$ (blue □).
right: Computation time scaled by the number of particles.
We achieved rms energy errors of the size $\approx 6 \cdot 10^{-10}$ and rms force errors of the size $\approx 5 \cdot 10^{-8}$.

the well known NFFT based methods for open as well as for 3d-periodic boundary conditions. The new algorithms have been implemented as a part of the P^{2}NFFT solver within the ScaFaCoS library [1], which is publicly available.

Beside the well known parameters of the P^{3}M, we introduce the oversampled grid size $\boldsymbol{m}$, and two parameters that characterize the regularization, namely the degree of smoothness p and the regularization grid size P. We give numerical evidence that the error estimates [15] of the P^{3}M still hold for our algorithms, provided that P and p are chosen large enough. Furthermore, we have seen that the accuracy is not sensitive to these two parameters. Already for $p = 10$ we were able to find suitable values for P in order to get close to machine precision. Moreover, choosing P to larger than necessary does not affect the complexity of our algorithm. This is because the same accuracy can be reached for increasing system size at constant P. Since all parameters that influence the complexity can be chosen based on the P^{3}M error estimates, we expect an arithmetic complexity of $\mathcal{O}(N \log N)$. However, the development of exact error estimates is beyond the scope of this paper and subject to future research.

We showed that the proposed methods for mixed periodicity can keep up with the well established algorithms for 3d-periodic boundary conditions (P^{3}M [25]) in terms of accuracy and runtime. Furthermore, our 2d-periodic algorithm can keep up with the spectrally accurate Ewald method [35] but we are able to use a smaller grid in the non-periodic dimension. For 1d-periodic boundary conditions we presented for the first time an efficient Fourier based algorithm tuned to high accuracy.

A further objective might be to derive error estimates, similar to the P^{3}M [30, 15], which allow an automatic tuning of the involved parameters, and to reduce the amount of precomputation steps.

Acknowledgements

We thank the anonymous reviewers for their very helpful suggestions and gratefully acknowledge support by the German Research Foundation (DFG), project PO 711/12-1.

Appendix

A. Proof of Theorem 4.1

In contrast to the case of periodicity in all three dimensions, it can be shown that a convergence factor of the form $\mathrm{e}^{-s\|\boldsymbol{x}_{ij}+L\boldsymbol{n}\|}$ instead of $\mathrm{e}^{-s\|L\boldsymbol{n}\|}$ can be used in order to calculate the spherical limit (4.1). For a proof see [6] or [4]. Thereby, the factor $\mathrm{e}^{-s\|\boldsymbol{x}_{ij}+L\boldsymbol{n}\|}$ can be replaced by $\mathrm{e}^{-s\|\boldsymbol{x}_{ij}+L\boldsymbol{n}\|^2}$. This can be understood easily by taking into consideration the general discussions on convergence factors in [32]. From [32, (2.2)] we see that the two convergence factors mentioned above are both suitable in terms of weighting the single parts of the sum with respect to $\|\boldsymbol{x}_{ij}+L\boldsymbol{n}\|$. As in [38] we apply the convergence factor $\mathrm{e}^{-s\|\boldsymbol{x}_{ij}+L\boldsymbol{n}\|^2}$ for the calculation of the potential (3.1), i.e., we compute the limit

$$\phi^{\mathrm{p2}}(\boldsymbol{x}_j) = \lim_{s\to 0} \sum_{\boldsymbol{n}\in\mathbb{Z}^2\times\{0\}} {\sum_{i=1}^{N}}' \frac{q_i \mathrm{e}^{-s\|\boldsymbol{x}_{ij}+L\boldsymbol{n}\|^2}}{\|\boldsymbol{x}_{ij}+L\boldsymbol{n}\|}.$$

For the calculation of $\phi^{\mathrm{p2}}(\boldsymbol{x}_j)$ we first apply (1.5) for the splitting parameter $\alpha > 0$ and obtain by exploiting (1.6)

$$\phi^{\mathrm{p2}}(\boldsymbol{x}_j) = \phi^{\mathrm{p2,S}}(\boldsymbol{x}_j) + \sum_{\boldsymbol{n}\in\mathbb{Z}^2\times\{0\}} \sum_{i=1}^{N} q_i \frac{\mathrm{erf}(\alpha\|\boldsymbol{x}_{ij}+L\boldsymbol{n}\|)}{\|\boldsymbol{x}_{ij}+L\boldsymbol{n}\|} + \phi^{\mathrm{p2,self}}(\boldsymbol{x}_j).$$

In order to calculate the remaining long range part we define

$$\phi_s(\boldsymbol{x}_j) := \sum_{\boldsymbol{n}\in\mathbb{Z}^2\times\{0\}} \sum_{i=1}^{N} q_i \mathrm{e}^{-s\|\boldsymbol{x}_{ij}+L\boldsymbol{n}\|^2} \frac{\mathrm{erf}(\alpha\|\boldsymbol{x}_{ij}+L\boldsymbol{n}\|)}{\|\boldsymbol{x}_{ij}+L\boldsymbol{n}\|},$$

which is absolutely convergent for all $s > 0$ and uniformly convergent on $s \geq 0$, cf. [32]. Then, we consider the limit $\lim_{s\to 0} \phi_s(\boldsymbol{x}_j)$. In the following, we apply the identity

$$\mathrm{erf}(\alpha\|\boldsymbol{x}_{ij}+L\boldsymbol{n}\|) = \frac{2}{\sqrt{\pi}}\|\boldsymbol{x}_{ij}+L\boldsymbol{n}\| \int_0^{\alpha} \mathrm{e}^{-\|\boldsymbol{x}_{ij}+L\boldsymbol{n}\|^2 z^2} \mathrm{d}z \tag{A.1}$$

in $\phi_s(\boldsymbol{x}_j)$ and use the Poisson summation formula

$$\sum_{\boldsymbol{n}\in\mathbb{Z}^2} \mathrm{e}^{-\beta\|\boldsymbol{x}+L\boldsymbol{n}\|^2} = \frac{1}{L^2} \sum_{\boldsymbol{k}\in\mathbb{Z}^2} \frac{\pi}{\beta} \mathrm{e}^{-\pi^2\|\boldsymbol{k}\|^2/(L^2\beta)} \mathrm{e}^{2\pi\mathrm{i}\boldsymbol{k}\cdot\boldsymbol{x}/L}$$

for a Gaussian kernel in two variables, which is valid for $\beta > 0$ and uniformly convergent on $\mathbb{R}^2$. Applying (A.1) we can write $\phi_s(\boldsymbol{x}_j)$ for $s > 0$ as an absolutely and uniformly convergent

sum of absolutely and uniformly convergent integrals. Thus, we may change the order of summation and integration to get

$$\begin{aligned}\phi_s(\boldsymbol{x}_j) &= \frac{2}{\sqrt{\pi}} \int_0^\alpha \sum_{i=1}^N q_i \mathrm{e}^{-(s+z^2)x_{ij,3}^2} \sum_{\tilde{\boldsymbol{n}}\in\mathbb{Z}^2} \mathrm{e}^{-(s+z^2)\|\tilde{\boldsymbol{x}}_{ij}+L\tilde{\boldsymbol{n}}\|^2} \mathrm{d}z \\ &= \frac{2}{\sqrt{\pi}} \int_0^\alpha \sum_{i=1}^N q_i \mathrm{e}^{-(s+z^2)x_{ij,3}^2} \sum_{\boldsymbol{k}\in\mathbb{Z}^2} \frac{\pi}{L^2(s+z^2)} \mathrm{e}^{\frac{-\pi^2\|\boldsymbol{k}\|^2}{L^2(s+z^2)}} \mathrm{e}^{2\pi\mathrm{i}\boldsymbol{k}\cdot\tilde{\boldsymbol{x}}_{ij}/L} \mathrm{d}z.\end{aligned}$$

As the Fourier series is uniformly convergent and the terms of the sum are continuous functions on $[0,\alpha]$ we obtain

$$\phi_s(\boldsymbol{x}_j) = \frac{2}{\sqrt{\pi}} \sum_{\boldsymbol{k}\in\mathbb{Z}^2} \sum_{i=1}^N q_i \frac{\pi}{L^2} \mathrm{e}^{2\pi\mathrm{i}\boldsymbol{k}\cdot\tilde{\boldsymbol{x}}_{ij}/L} \int_0^\alpha \frac{1}{s+z^2} \mathrm{e}^{\frac{-\pi^2\|\boldsymbol{k}\|^2}{L^2(s+z^2)}} \mathrm{e}^{-x_{ij,3}^2(s+z^2)} \mathrm{d}z. \tag{A.2}$$

In the following we separate the $\boldsymbol{k}=\boldsymbol{0}$ term and consider the sum

$$\frac{2}{\sqrt{\pi}} \sum_{\boldsymbol{k}\in\mathbb{Z}^2\setminus\{\boldsymbol{0}\}} \sum_{i=1}^N q_i \frac{\pi}{L^2} \mathrm{e}^{2\pi\mathrm{i}\boldsymbol{k}\cdot\tilde{\boldsymbol{x}}_{ij}/L} \int_0^\alpha \frac{1}{s+z^2} \mathrm{e}^{\frac{-\pi^2\|\boldsymbol{k}\|^2}{L^2(s+z^2)}} \mathrm{e}^{-x_{ij,3}^2(s+z^2)} \mathrm{d}z.$$

If the limit for $s\to 0$ of each single summand exists, we are allowed to change the order of summation and calculating the limits. In the following, we will show that these limits exist. We have

$$\lim_{s\to 0} \int_0^\alpha \frac{1}{s+z^2} \mathrm{e}^{\frac{-\pi^2\|\boldsymbol{k}\|^2}{L^2(s+z^2)}} \mathrm{e}^{-x_{ij,3}^2(s+z^2)} \mathrm{d}z = \int_0^\alpha \frac{1}{z^2} \mathrm{e}^{\frac{-\pi^2\|\boldsymbol{k}\|^2}{L^2z^2}} \mathrm{e}^{-x_{ij,3}^2z^2} \mathrm{d}z.$$

This can be proved as follows. For $s>0$ we define the function f_s by $f_s(z) := z^2+s$ and set $f(z) := z^2$. Then the convergence $f_s \to f$ is uniform on $[0,\alpha]$. The function

$$h(y) := \begin{cases} \frac{1}{y} \mathrm{e}^{\frac{-\pi^2\|\boldsymbol{k}\|^2}{L^2 y}} \mathrm{e}^{-x_{ij,3}^2 y} & : z \neq 0, \\ 0 & : z = 0 \end{cases}$$

is continuous and, therefore, uniformly continuous on $[0,\alpha]$. Thus, the convergence $h\circ f_s \to h\circ f$ is also uniform on $[0,\alpha]$ and the limit can be applied to the integrand. For the computation of the integral on the right hand side we substitute $y := z^{-1}$ and obtain

$$\begin{aligned}\int_0^\alpha \frac{1}{z^2} \mathrm{e}^{\frac{-\pi^2\|\boldsymbol{k}\|^2}{L^2z^2}} \mathrm{e}^{-x_{ij,3}^2z^2} \mathrm{d}z &= \int_{1/\alpha}^\infty \exp\left(\frac{-\pi^2\|\boldsymbol{k}\|^2y^2}{L^2} - \frac{x_{ij,3}^2}{y^2}\right) \mathrm{d}y \\ &= \int_{1/\alpha}^\infty \exp\left[-\left(\frac{\pi\|\boldsymbol{k}\|y}{L} + \frac{x_{ij,3}}{y}\right)^2 + \frac{2\pi\|\boldsymbol{k}\|x_{ij,3}}{L}\right] \mathrm{d}y \qquad \text{(A.3)} \\ &= \int_{1/\alpha}^\infty \exp\left[-\left(\frac{\pi\|\boldsymbol{k}\|y}{L} - \frac{x_{ij,3}}{y}\right)^2 - \frac{2\pi\|\boldsymbol{k}\|x_{ij,3}}{L}\right] \mathrm{d}y. \qquad \text{(A.4)}\end{aligned}$$

For the substitutions

$$t_1 := \frac{\pi\|\boldsymbol{k}\|y}{L} + \frac{x_{ij,3}}{y} \quad \text{and} \quad t_2 := \frac{\pi\|\boldsymbol{k}\|y}{L} - \frac{x_{ij,3}}{y}$$

we obtain

$$\mathrm{d}t_1 + \mathrm{d}t_2 = \left(\frac{\pi\|\boldsymbol{k}\|}{L} - \frac{x_{ij,3}}{y^2}\right)\mathrm{d}y + \left(\frac{\pi\|\boldsymbol{k}\|}{L} + \frac{x_{ij,3}}{y^2}\right)\mathrm{d}y = \frac{2\pi\|\boldsymbol{k}\|}{L}\mathrm{d}y.$$

Thus, using (A.3) and (A.4), we get

$$\int_0^\alpha \frac{1}{z^2}\mathrm{e}^{\frac{-\pi^2\|\boldsymbol{k}\|^2}{L^2z^2}}\mathrm{e}^{-x_{ij,3}^2z^2}\mathrm{d}z = \frac{L}{2\pi\|\boldsymbol{k}\|}\left[\mathrm{e}^{2\pi\|\boldsymbol{k}\|x_{ij,3}/L}\int_{\frac{\pi\|\boldsymbol{k}\|}{\alpha L}+\alpha x_{ij,3}}^\infty \mathrm{e}^{-t_1^2}\mathrm{d}t_1 \right.$$
$$\left. + \mathrm{e}^{-2\pi\|\boldsymbol{k}\|x_{ij,3}/L}\int_{\frac{\pi\|\boldsymbol{k}\|}{\alpha L}-\alpha x_{ij,3}}^\infty \mathrm{e}^{-t_2^2}\mathrm{d}t_2\right] = \frac{L\sqrt{\pi}}{4\pi}\Theta^{\mathrm{p2}}(\|\boldsymbol{k}\|, x_{ij,3})$$

and, therefore, the limit of $\phi_s(\boldsymbol{x}_j)$ can be written in the form

$$\lim_{s\to 0}\phi_s(\boldsymbol{x}_j) = \phi^{\mathrm{p2,L}}(\boldsymbol{x}_j) + \lim_{s\to 0}\frac{2\sqrt{\pi}}{L^2}\sum_{i=1}^N q_i\mathrm{e}^{-sx_{ij,3}^2}\int_0^\alpha \frac{\mathrm{e}^{-x_{ij,3}^2z^2}}{s+z^2}\mathrm{d}z.$$

Now, we use the substitution $y := \frac{z}{\sqrt{s}}$ and obtain

$$I(s) := \int_0^\alpha \frac{\mathrm{e}^{-x_{ij,3}^2z^2}}{s+z^2}\mathrm{d}z = \int_0^{\frac{\alpha}{\sqrt{s}}} \frac{\mathrm{e}^{-sx_{ij,3}^2z^2}}{\sqrt{s}(1+z^2)}\mathrm{d}z.$$

Replacing the term $f(s) := \mathrm{e}^{-sx_{ij,3}^2z^2}$ by its Taylor representation $f(s) = \sum_{n=0}^\infty (-1)^n(x_{ij,3}z)^{2n}\frac{s^n}{n!}$ we have

$$I(s) = \sum_{n=0}^\infty \frac{(-1)^n x_{ij,3}^{2n}s^n}{n!\sqrt{s}}\int_0^{\frac{\alpha}{\sqrt{s}}}\frac{z^{2n}}{1+z^2}\mathrm{d}z. \tag{A.5}$$

In the following steps we make use of the identity

$$\int_0^\beta \frac{z^{2n}}{1+z^2}\mathrm{d}z = (-1)^n\arctan\beta + (-1)^{n+1}\sum_{k=0}^{n-1}(-1)^k\frac{\beta^{2k+1}}{2k+1}, \tag{A.6}$$

which is valid for $\beta > 0$, $n \in \mathbb{N}_0$ and can easily be verified by induction. Furthermore, we use the Taylor representation

$$\sqrt{\pi}\alpha z\cdot\mathrm{erf}(\alpha z) + \mathrm{e}^{-\alpha^2z^2} = 1 + \sum_{n=0}^\infty \frac{(-1)^n(\alpha z)^{2n+2}}{(n+1)!(2n+1)}$$

holding for $\alpha > 0$ and each $z \in \mathbb{R}$. Applying (A.6) with $\beta = \frac{\alpha}{\sqrt{s}}$ we get

$$\frac{s^n}{\sqrt{s}}\int_0^{\frac{\alpha}{\sqrt{s}}}\frac{z^{2n}}{1+z^2}\mathrm{d}z = \frac{(-1)^n s^n}{\sqrt{s}}\arctan\left(\frac{\alpha}{\sqrt{s}}\right) + (-1)^{n+1}\sum_{k=0}^{n-1}(-1)^k\frac{\alpha^{2k+1}s^n}{(2k+1)s^{k+1}}$$
$$= \begin{cases}\mathcal{O}(\sqrt{s}) + \frac{\alpha^{2n-1}}{(2n-1)} + \mathcal{O}(s) \text{ for } s\to 0 & : n > 0,\\ \frac{1}{\sqrt{s}}\arctan\left(\frac{\alpha}{\sqrt{s}}\right) & : n = 0.\end{cases}$$

Inserting this result into (A.5) we obtain

$$\begin{aligned} I(s) &= \frac{1}{\sqrt{s}} \arctan\left(\tfrac{\alpha}{\sqrt{s}}\right) + \sum_{n=1}^{\infty} \frac{(-1)^n x_{ij}^{2n} \alpha^{2n-1}}{n!(2n-1)} + \mathcal{O}(\sqrt{s}) \\ &= \frac{1}{\sqrt{s}} \arctan\left(\tfrac{\alpha}{\sqrt{s}}\right) + \sum_{n=0}^{\infty} \frac{(-1)^{n+1} x_{ij}^{2n+2} \alpha^{2n+1}}{(n+1)!(2n+1)} + \mathcal{O}(\sqrt{s}) \\ &= \frac{1}{\sqrt{s}} \arctan\left(\tfrac{\alpha}{\sqrt{s}}\right) - \sqrt{\pi} x_{ij,3} \cdot \operatorname{erf}(\alpha x_{ij,3}) - \frac{1}{\alpha} \mathrm{e}^{-\alpha^2 x_{ij,3}^2} + \frac{1}{\alpha} + \mathcal{O}(\sqrt{s}) \end{aligned}$$

and by exploiting the charge neutrality (1.1) we get

$$\begin{aligned} \lim_{s\to 0} \phi_s(\boldsymbol{x}_j) &= \phi^{\mathrm{p2,L}}(\boldsymbol{x}_j) + \lim_{s\to 0} \frac{2\sqrt{\pi}}{L^2} \sum_{i=1}^{N} q_i \mathrm{e}^{-s x_{ij,3}^2} I(s) \\ &= \phi^{\mathrm{p2,L}}(\boldsymbol{x}_j) - \frac{2\sqrt{\pi}}{L^2} \sum_{i=1}^{N} q_i \left(\frac{\mathrm{e}^{-\alpha^2 x_{ij,3}^2}}{\alpha} + \sqrt{\pi} x_{ij,3} \cdot \operatorname{erf}(\alpha x_{ij,3}) \right) \\ &= \phi^{\mathrm{p2,L}}(\boldsymbol{x}_j) + \phi^{\mathrm{p2},\mathbf{0}}(\boldsymbol{x}_j)\,. \end{aligned}$$

■

B. Proof of Theorem 5.1

As in Theorem 4.1 we apply the convergence factor $\mathrm{e}^{-s\|\boldsymbol{x}_{ij}+L\boldsymbol{n}\|^2}$ for the calculation of the potential (5.1). After using the splitting (1.5) we obtain

$$\phi^{\mathrm{p1}}(\boldsymbol{x}_j) = \phi^{\mathrm{p1,S}}(\boldsymbol{x}_j) + \sum_{\boldsymbol{n}\in\mathbb{Z}\times\{0\}^2} \sum_{i=1}^{N} q_i \frac{\operatorname{erf}(\alpha\|\boldsymbol{x}_{ij}+L\boldsymbol{n}\|)}{\|\boldsymbol{x}_{ij}+L\boldsymbol{n}\|} + \phi^{\mathrm{p1,self}}(\boldsymbol{x}_j).$$

We define

$$\phi_s(\boldsymbol{x}_j) := \sum_{\boldsymbol{n}\in\mathbb{Z}\times\{0\}^2} \sum_{i=1}^{N} q_i \mathrm{e}^{-s\|\boldsymbol{x}_{ij}+L\boldsymbol{n}\|^2} \frac{\operatorname{erf}(\alpha\|\boldsymbol{x}_{ij}+L\boldsymbol{n}\|)}{\|\boldsymbol{x}_{ij}+L\boldsymbol{n}\|}$$

and use the Poisson summation formula

$$\sum_{n\in\mathbb{Z}} \mathrm{e}^{-\beta(x+nL)^2} = \frac{1}{L} \sum_{k\in\mathbb{Z}} \sqrt{\frac{\pi}{\beta}} \mathrm{e}^{-\pi^2 k^2/(L^2\beta)} \mathrm{e}^{2\pi \mathrm{i} k x/L}$$

to obtain

$$\phi_s(\boldsymbol{x}_j) = \frac{2}{\sqrt{\pi}} \sum_{k\in\mathbb{Z}} \sum_{i=1}^{N} q_i \frac{\sqrt{\pi}}{L} \mathrm{e}^{2\pi \mathrm{i} k(x_{i,1}-x_{j,1})/L} \int_0^{\alpha} \frac{1}{\sqrt{s+z^2}} \mathrm{e}^{\frac{-\pi^2 k^2}{L^2(s+z^2)}} \mathrm{e}^{-\|\tilde{\boldsymbol{x}}_{ij}\|^2(s+z^2)} \mathrm{d}z,$$

analogously to (A.2). Again, for $k \neq 0$ we compute the limit for $s \to 0$ under the integrals and obtain by similar steps as in the proof of Theorem 4.1

$$\lim_{s\to 0} \phi_s(\boldsymbol{x}_j) = \phi^{\mathrm{p1,L}}(\boldsymbol{x}_j) + \lim_{s\to 0} \frac{2}{L} \sum_{i=1}^{N} q_i \mathrm{e}^{-s\xi_{ij}^2} \int_0^{\alpha} \frac{\mathrm{e}^{-\xi_{ij}^2 z^2}}{\sqrt{s+z^2}} \mathrm{d}z,$$

where we set $\xi_{ij} := \|\tilde{\boldsymbol{x}}_{ij}\|$. In order to compute the remaining limit for $k = 0$ we make use of the substitution $y := \frac{z}{\sqrt{s}}$ again and get

$$I(s) := \int_0^{\alpha} \frac{\mathrm{e}^{-\xi_{ij}^2 z^2}}{\sqrt{s+z^2}} \mathrm{d}z = \int_0^{\frac{\alpha}{\sqrt{s}}} \frac{\mathrm{e}^{-s\xi_{ij}^2 z^2}}{\sqrt{1+z^2}} \mathrm{d}z.$$

Replacing the exponential by its Taylor representation in s we have

$$I(s) = \sum_{n=0}^{\infty} \frac{(-1)^n \xi_{ij}^{2n} s^n}{n!} \int_0^{\frac{\alpha}{\sqrt{s}}} \frac{z^{2n}}{\sqrt{1+z^2}} \mathrm{d}z.$$

In the following, we use that for $\beta > 0$ and $n \in \mathbb{N}$ we have

$$\int_0^{\beta} \frac{x^{2n} \mathrm{d}x}{\sqrt{1+x^2}} = (-1)^n \frac{(2n-1)!!}{(2n)!!} \left(\sqrt{1+\beta^2} \sum_{k=1}^{n} (-1)^k \frac{(2k-2)!!}{(2k-1)!!} \beta^{2k-1} + \ln(\beta + \sqrt{1+\beta^2}) \right).$$

where $(2n)!! := (2n) \cdot (2n-2) \cdot \cdots \cdot 2$ and $(2n-1)!! := (2n-1) \cdot (2n-3) \cdot \cdots \cdot 1$ for $n \in \mathbb{N}$. The proof can be done via induction in n. We get

$$\int_0^{\frac{\alpha}{\sqrt{s}}} \frac{1}{\sqrt{1+z^2}} \mathrm{d}z = \ln\left(\frac{\alpha}{\sqrt{s}} + \frac{\sqrt{s+\alpha^2}}{\sqrt{s}} \right)$$

for $n = 0$ and in the case $n > 0$ we obtain

$$\begin{aligned} s^n \int_0^{\frac{\alpha}{\sqrt{s}}} \frac{z^{2n}}{\sqrt{1+z^2}} \mathrm{d}z &= (-1)^n \frac{\sqrt{s+\alpha^2}}{\sqrt{s}} s^n \frac{(2n-1)!!}{(2n)!!} \sum_{k=1}^{n} (-1)^k \frac{(2k-2)!!}{(2k-1)!!} \frac{\alpha^{2k-1}\sqrt{s}}{s^k} \\ &\quad + (-1)^n s^n \frac{(2n-1)!!}{(2n)!!} \ln\left(\frac{\alpha}{\sqrt{s}} + \frac{\sqrt{s+\alpha^2}}{\sqrt{s}} \right) \\ &= \mathcal{O}(s) + \sqrt{s+\alpha^2} \cdot \frac{\alpha^{2n-1}}{2n} + (-1)^n s^n \frac{(2n-1)!!}{(2n)!!} \ln\left(\frac{\alpha}{\sqrt{s}} + \frac{\sqrt{s+\alpha^2}}{\sqrt{s}} \right) \end{aligned}$$

for $s \to 0$. Applying (5.4), (5.5) as well as the charge neutrality condition (1.1) we get

$$\begin{aligned} \lim_{s\to 0} \phi_s(\boldsymbol{x}_j) &= \phi^{\mathrm{p1,L}}(\boldsymbol{x}_j) + \lim_{s\to 0} \frac{2}{L} \sum_{i=1}^{N} q_i \mathrm{e}^{-s\xi_{ij}^2} I(s), \\ &= \phi^{\mathrm{p1,L}}(\boldsymbol{x}_j) + \frac{2}{L} \sum_{i=1}^{N} q_i \sum_{n=1}^{\infty} \frac{(-1)^n \xi_{ij}^{2n} \alpha^{2n}}{n! 2n} \\ &= \phi^{\mathrm{p1,L}}(\boldsymbol{x}_j) - \frac{1}{L} \sum_{\substack{i=1 \\ \|\tilde{\boldsymbol{x}}_{ij}\| \neq 0}}^{N} q_i \left[\gamma + \Gamma(0, \alpha^2 \|\tilde{\boldsymbol{x}}_{ij}\|^2) + \ln(\alpha^2 \|\tilde{\boldsymbol{x}}_{ij}\|^2) \right]. \end{aligned}$$

■

C. Two point Taylor interpolation

In order to construct the smooth (p-times differentiable) transitions in (4.12) we have to regularize different functions; see also Figure 4.3. Thereby, we know the function values and the derivatives in the boundary points (in the following denoted by a_j and b_j) and compute a regularization (in the following denoted by P). The following theorems give the precise definition of the regularizing functions.

Theorem C.1. *Let an interval $[m-r, m+r], r > 0$, and the interpolation values $a_j = K^{(j)}(m-r)$, $b_j = K^{(j)}(m+r)$, $j = 0, \dots, p-1$, be given. For $y = \frac{x-m}{r}$ the polynomial*

$$\begin{aligned} P(x) &= \sum_{j=0}^{p-1} \sum_{k=0}^{p-1-j} \binom{p-1+k}{k} \frac{1}{j! 2^p 2^k} \left[r^j (1-y)^p (1+y)^{k+j} a_j + (-r)^j (1+y)^p (1-y)^{k+j} b_j \right] \\ &= \sum_{j=0}^{p-1} B(p,j,y) r^j a_j + \sum_{j=0}^{p-1} B(p,j,-y)(-r)^j b_j \end{aligned}$$

of degree $2p-1$ satisfies the interpolation conditions $P^{(j)}(m-r) = a_j, P^{(j)}(m+r) = b_j$, $j = 0, \dots, p-1$. Hereby, the basis polynomials $B(p,j,y)$ are given by

$$B(p,j,y) := \sum_{k=0}^{p-1-j} \binom{p-1+k}{k} \frac{1}{j! 2^p 2^k} (1-y)^p (1+y)^{k+j}.$$

Proof. See [3, Corollary 2.2.6] or [20, Proposition 3.2]. ∎

The following theorem gives the precise definition of the slightly different regularizing functions that are used Section 5.2 for the 1d-periodic case; see also Figure 5.1. It differs form the theorem above such that the function value in the second interpolation point is unknown.

Theorem C.2. *Let an interval $[m-r, m+r], r > 0$, and the interpolation values $a_j = K^{(j)}(m-r)$, $j = 0, \dots, p-1$, and $b_j = K^{(j)}(m+r)$, $j = 1, \dots, p-1$, be given. For $y = \frac{x-m}{r}$ the polynomial*

$$\begin{aligned} Q(x) :=& \sum_{j=0}^{p-2} I(p-1,j,y) r^{j+1} a_{j+1} + \sum_{j=0}^{p-2} I(p-1,j,-y)(-r)^{j+1} b_{j+1} \\ & - \sum_{j=0}^{p-2} I(p-1,j,-1) r^{j+1} a_{j+1} - \sum_{j=0}^{p-2} I(p-1,j,1)(-r)^{j+1} b_{j+1} + a_0 \end{aligned}$$

of degree $2p-2$ satisfies the interpolation conditions $Q^{(j)}(m-r) = a_j, j = 0, \dots, p-1$, and $Q^{(j)}(m+r) = b_j$, $j = 1, \dots, p-1$. Thereby, the polynomials $I(p,j,y)$ are given by

$$I(p,j,y) := \sum_{k=0}^{p-1-j} \binom{p-1+k}{k} \frac{1}{j! 2^p 2^k} \sum_{l=0}^{p} \frac{p!}{(p-l)!} \frac{(k+j)!}{(k+1+j+l)!} (1-y)^{p-l} (1+y)^{k+j+1+l}.$$

Proof. According to Theorem C.1 the polynomial

$$\tilde{P}(x) = \sum_{j=0}^{p-2} B(p-1,j,y) r^j a_{j+1} + \sum_{j=0}^{p-2} B(p-1,j,-y)(-r)^j b_{j+1}$$

satisfies the interpolation conditions $\tilde{P}^{(j)}(m-r) = a_{j+1}, \tilde{P}^{(j)}(m+r) = b_{j+1}$, $j = 0, \ldots, p-2$. For $k, l \in \mathbb{N}$ we obtain by partial integration for l times

$$\int (1-x)^l (1+x)^k \mathrm{d}x = \sum_{j=0}^{l} \frac{l!}{(l-j)!} \frac{k!}{(k+1+j)!} (1-x)^{l-j} (1+x)^{k+1+j} + C, C \in \mathbb{R}$$

and therewith

$$\int B(p,j,y)\mathrm{d}x = rI(p,j,y) + C, C \in \mathbb{R}.$$

Thus, the antiderivatives of $\tilde{P}(x)$ are given by $Q(x) := \tilde{Q}(x) + C$, $C \in \mathbb{R}$ with

$$\tilde{Q}(x) := \sum_{j=0}^{p-2} I(p-1,j,y) r^{j+1} a_{j+1} + \sum_{j=0}^{p-2} I(p-1,j,-y)(-r)^{j+1} b_{j+1}.$$

Finally, we choose the constant $C = a_0 - \tilde{Q}(m-r)$ in order to satisfy $Q(m-r) = a_0$. ■

D. Parameter estimation for 3d-periodic Ewald summation

For sake of simplicity we only consider cubic simulation boxes of length L. We assume that the real space cutoff r_{cut} is chosen such that the short range part (3.3) is computational tractable and we want to tune all other parameters such that the rms energy error $\Delta U_{\mathcal{S}}$ defined in (1.8) is below some prescribed error bound. For uncorrelated particle positions it is well known that the Ewald splitting parameter α and the radial Fourier space cutoff k_{cut} of the classical 3d-periodic Ewald summation can be determined by inversion of the very accurate error estimates given in [30] resulting in

$$\alpha = \frac{1}{r_{\mathrm{cut}}} \sqrt{\mathrm{W}\left(\frac{2}{\Delta U_{\mathcal{S}}} Q \sqrt{\frac{r_{\mathrm{cut}}}{NL^3}}\right)}, \tag{D.1}$$

$$k_{\mathrm{cut}} = \frac{\sqrt{3} L \alpha}{2\pi} \sqrt{\mathrm{W}\left(\frac{4}{3L^2}\left(\frac{2}{N\alpha\pi}\right)^{2/3}\left(Q\frac{2}{\Delta U_{\mathcal{S}}}\right)^{4/3}\right)}. \tag{D.2}$$

Hereby, $Q = \sum_{j=1}^{N} q_j^2$ is the sum of all squared charges, L is the box length and $\mathrm{W}(\cdot)$ is the Lambert-W function defined as the inverse of $f(w) = we^w$. Note that we inserted $\Delta U_{\mathcal{S}}/2$ into the error formulae of [30] in order to guarantee that the sum of the real space and Fourier space error is below the rms energy error $\Delta U_{\mathcal{S}}$. The corresponding size M of a cubic Fourier space grid must be chosen large enough to include all the grid points $\|\boldsymbol{k}\| \leq k_{\mathrm{cut}}$, e.g.,

$$M = 2\lceil k_{\mathrm{cut}} \rceil + 2. \tag{D.3}$$

Although they do not provide any proof, [35] give some numerical evidence that these formulae can also be used in the 2d-periodic case. This encourages us to determine the Ewald splitting parameter α by (D.1) as well as the number of Fourier coefficients corresponding to periodic dimensions by (D.2) and (D.3) for the 2d- and even for the 1d-periodic case.

Since we want to use NFFTs in order to speed up the computation of the Fourier space contribution (3.4), we need to tune the oversampled grid size $\boldsymbol{m}$ and the order of the B-Spline

				radial grid		cubic grid	
N	L	$\boldsymbol{M}$	$\boldsymbol{m}$	$\Delta U_{\mathbb{Z}^3}$	$\Delta F_{\mathbb{Z}^3}$	$\Delta U_{\mathbb{Z}^3}$	$\Delta F_{\mathbb{Z}^3}$
1000	1.0	(26,26,26)	(32,32,32)	9.70e-10	5.28e-08	4.63e-10	3.48e-08
12000	2.29	(54,54,54)	(68,68,68)	9.56e-10	5.22e-08	4.81e-10	3.55e-08
23000	2.84	(66,66,66)	(82,82,82)	9.95e-10	5.38e-08	4.87e-10	3.56e-08
34000	3.24	(74,74,74)	(92,92,92)	9.85e-10	5.32e-08	4.92e-10	3.57e-08
45000	3.56	(82,82,82)	(102,102,102)	9.69e-10	5.25e-08	4.88e-10	3.55e-08
56000	3.83	(88,88,88)	(110,110,110)	9.72e-10	5.30e-08	4.89e-10	3.55e-08
67000	4.06	(92,92,92)	(114,114,114)	9.87e-10	5.31e-08	5.02e-10	3.57e-08
78000	4.27	(98,98,98)	(122,122,122)	9.63e-10	5.48e-08	4.91e-10	3.89e-08
89000	4.46	(102,102,102)	(126,126,126)	9.79e-10	5.83e-08	4.98e-10	4.31e-08
100000	4.64	(106,106,106)	(132,132,132)	9.74e-10	6.24e-08	4.94e-10	4.88e-08

Table D.1: List of parameters and achieved accuracies for NFFT based fast Ewald summation with target accuracy $\Delta U_{\mathbb{Z}^3} = 10^{-9}$, real space cutoff $r_{\text{cut}} = 0.62$, Ewald splitting parameter $\alpha = 7.489225$, and B-spline order 14. The oversampled grid size $\boldsymbol{m}$ and the order of the B-Spline have been tuned only for the smallest test case $N = 1000$. For the larger test cases we set $\boldsymbol{m} \approx 1.23\boldsymbol{M}$.

order such that the NFFT approximation error is not visible anymore in comparison to the truncation error in Fourier space due to k_{cut}. We claim that these two parameters must be tuned only for a small test system. For larger particle numbers the same accuracy can be achieved by keeping the B-Spline order and the vector valued oversampling factor $\boldsymbol{m} \odot \boldsymbol{M}^{-1}$ constant. In Table D.1 we give numerical evidence that this parameter tuning works very well for random particle distribution defined in Example 4.8. In order to highlight the exactness of the predicted accuracy we computed the NFFT on the radial grid $\|\boldsymbol{k}\| \leq k_{\text{cut}}$ and show the corresponding energy error in columns 5. In contrast using the full cubic grid results in an even better accuracy than predicted; see column 7 of Table D.1. For the sake of completeness we also list the force errors for both Fourier space cutoff schemes.

E. Error per particle distribution

In the following we show that choosing an appropriate regularization grid size P results in an equal error distribution over the whole box. Especially, the errors do not increase at the border of the simulation box. Therefore, we investigate the per particle energy and force errors of $N = 1000$ randomly equally distributed particles; see Example 4.8 for definition of the test system. Figure E.1 shows the distribution of the energy error and force errors per particle in dependence on the non-periodic coordinate. Thereby we chose the parameters that have been identified in Example 4.8 for an target accuracy of $\Delta U_{\mathbb{Z}^2\times\{0\}} = 10^{-9}$. We see that our choice of $P = 32$ guarantees an almost equal distribution of the energy errors in the box. However, the error of the forces increases slightly at the border of the simulation box. This is due to the fact that we tuned P only for an optimal energy error. Figure E.2 shows that larger $P = 36$ gives also an equal distribution of the force errors. In contrast, for smaller $P = 28$ the errors increase a lot at the boundary of the simulation box. We observed exactly the same behavior for the two non-periodic dimension in the 1d-periodic case. Furthermore, we observed that the error distribution along periodic dimensions is also equal over the whole

box. In summary we see that choosing the regularization grid size P large enough means increasing P until the boundary effects of the errors disappear.

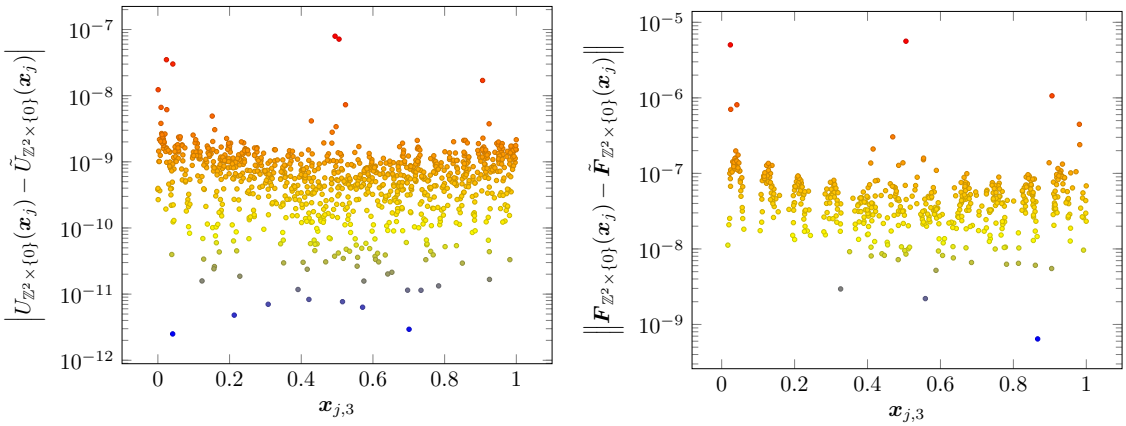

Figure E.1: Energy and force error distribution over $N = 1000$ randomly distributed particles $\boldsymbol{x}_j$ under 2d-periodic boundary conditions. The regularization grid size $P = 32$ was tuned for an optimal energy error.
left: Energy error per particle as function over the non-periodic coordinate $\boldsymbol{x}_{j,3}$.
right: Force error in the third component as function over the non-periodic coordinate $\boldsymbol{x}_{j,3}$ for $P = 32$.

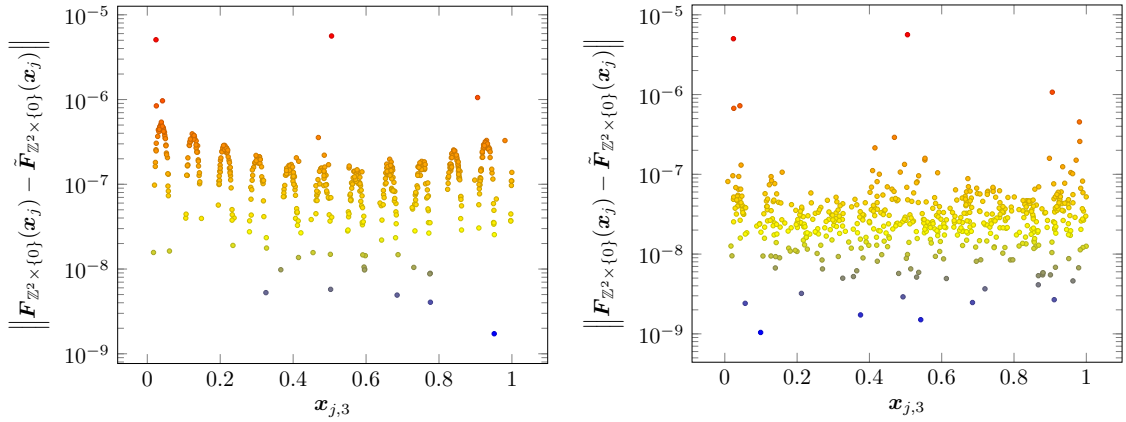

Figure E.2: Force error distribution over $N = 1000$ randomly distributed particles $\boldsymbol{x}_j$ under 2d-periodic boundary conditions.
left: Force error in the third component as function over the non-periodic coordinate $\boldsymbol{x}_{j,3}$ for regularization grid size $P = 28$.
right: Force error in the third component as function over the non-periodic coordinate $\boldsymbol{x}_{j,3}$ for regularization grid size $P = 36$.

References

[1] *ScaFaCoS - Scalable Fast Coloumb Solvers.* http://www.scafacos.de.

[2] M. Abramowitz and I.A. Stegun (eds.): *Handbook of Mathematical Functions.* National Bureau of Standards, Washington, DC, USA, 1972.

[3] R.P. Agarwal and P.J.Y. Wong: *Error inequalities in polynomial interpolation and their applications*, vol. 262 of *Mathematics and its Applications.* Kluwer Academic Publishers Group, Dordrecht, 1993.

[4] A. Arnold: *Berechnung der elektrostatischen Wechselwirkung in 2d+h periodischen Systemen.* Diplomarbeit, Johannes Gutenberg-Universität, Mainz, 2001.

[5] A. Arnold, F. Fahrenberger, C. Holm, O. Lenz, M. Bolten, H. Dachsel, R. Halver, I. Kabadshow, F. Gähler, F. Heber, J. Iseringhausen, M. Hofmann, M. Pippig, D. Potts, and G. Sutmann: *Comparison of scalable fast methods for long-range interactions.* Phys. Rev. E, 88:063308, 2013.

[6] A. Arnold and C. Holm: *MMM2D: A fast and accurate summation method for electrostatic interactions in 2D slab geometries.* Comput. Phys. Commun., 148:327 – 348, 2002.

[7] A. Arnold and C. Holm: *MMM1D: A method for calculating electrostatic interactions in one-dimensional periodic geometries.* J. Chem. Phys., 123:144103, 2005.

[8] A. Arnold, J. de Joannis, and C. Holm: *Electrostatics in periodic slab geometries. I.* J. Chem. Phys., 117:2496, 2002.

[9] G. Beylkin: *On the fast Fourier transform of functions with singularities.* Appl. Comput. Harmon. Anal., 2:363 – 381, 1995.

[10] A. Bródka: *Ewald summation method with electrostatic layer correction for interactions of point dipoles in slab geometry.* Chem. Phys. Lett., 400:62 – 67, 2004.

[11] A. Bródka and P. Sliwinski: *Three-dimensional Ewald method with correction term for a system periodic in one direction.* J. Chem. Phys., 120:5518 – 5523, 2004.

[12] H. Dachsel: *An error-controlled Fast Multipole Method.* J. Chem. Phys., 132(11):119901, 2010.

[13] T. Darden, D. York, and L. Pedersen: *Particle mesh Ewald: An $N\log(N)$ method for Ewald sums in large systems.* J. Chem. Phys., 98:10089–10092, 1993.

[14] M. Deserno and C. Holm: *How to mesh up Ewald sums. I. A theoretical and numerical comparison of various particle mesh routines.* J. Chem. Phys., 109:7678 – 7693, 1998.

[15] M. Deserno and C. Holm: *How to mesh up Ewald sums. II. An accurate error estimate for the Particle-Particle-Particle-Mesh algorithm.* J. Chem. Phys., 109:7694 – 7701, 1998.

[16] Z.H. Duan and R. Krasny: *An Ewald summation based multipole method.* J. Chem. Phys., 113:3492, 2000.

[17] A. Dutt and V. Rokhlin: *Fast Fourier transforms for nonequispaced data.* SIAM J. Sci. Stat. Comput., 14:1368 – 1393, 1993.

[18] U. Essmann, L. Perera, M.L. Berkowitz, T. Darden, H. Lee, and L.G. Pedersen: *A smooth particle mesh Ewald method.* J. Chem. Phys., 103:8577 – 8593, 1995.

[19] P.P. Ewald: *Die Berechnung optischer und elektrostatischer Gitterpotentiale.* Ann. Phys., 369:253–287, 1921.

[20] M. Fenn and G. Steidl: *Fast NFFT based summation of radial functions.* Sampl. Theory Signal Image Process., 3:1 – 28, 2004.

[21] D. Frenkel and B. Smit: *Understanding molecular simulation: From algorithms to applications.* Academic Press, 2002.

[22] L. Greengard and J.Y. Lee: *Accelerating the nonuniform fast Fourier transform.* SIAM Rev., 46:443 – 454, 2004.

[23] A. Grzybowski, E. Gwóźdź, and A. Bródka: *Ewald summation of electrostatic interactions in molecular dynamics of a three-dimensional system with periodicity in two directions.* Phys. Rev. B, 61:6706–6712, 2000.

[24] F.E. Harris: *Incomplete Bessel, generalized incomplete gamma, or leaky aquifer functions.* J. Comput. Appl. Math., 215:260 – 269, 2008.

[25] R.W. Hockney and J.W. Eastwood: *Computer simulation using particles.* Taylor & Francis, Inc., Bristol, PA, USA, 1988.

[26] P.H. Hünenberger: *Lattice-sum methods for computing electrostatic interactions in molecular simulations.* In *Simulation and theory of electrostatic interactions in solution*, vol. 17, pp. 17 – 83. ASCE, 1999.

[27] I. Kabadshow: *Periodic Boundary Conditions and the Error-Controlled Fast Multipole Method.* PhD thesis, Bergische Universität Wuppertal, Jülich, 2012.

[28] I. Kabadshow and H. Dachsel: *The Error-Controlled Fast Multipole Method for Open and Periodic Boundary Conditions.* In G. Sutmann, P. Gibbon, and T. Lippert (eds.): *Fast Methods for Long-Range Interactions in Complex Systems*, IAS-Series, pp. 85 – 113, Jülich, 2011. Forschungszentrum Jülich.

[29] J. Keiner, S. Kunis, and D. Potts: *Using NFFT3 - a software library for various nonequispaced fast Fourier transforms.* ACM Trans. Math. Software, 36:Article 19, 1 – 30, 2009.

[30] J. Kolafa and J.W. Perram: *Cutoff errors in the Ewald summation formulae for point charge systems.* Molecular Simulation, 9(5):351 – 368, 1992.

[31] K.N. Kudin and G.E. Scuseria: *Revisiting infinite lattice sums with the periodic fast multipole method.* J. Chem. Phys., 121(7):2886 – 2890, 2004.

[32] S.W. de Leeuw, J.W. Perram, and E.R. Smith: *Simulation of electrostatic systems in periodic boundary conditions. I. Lattice sums and dielectric constants.* Proc. Roy. Soc. London Ser. A, 373:27 – 56, 1980.

[33] D. Lindbo: *Fast Ewald Methods and Topics in Fluid Interface Simulation.* PhD thesis, KTH, School of Computer Science and Communication (CSC), Numerical Analysis, NA, 2011.

[34] D. Lindbo and A.K. Tornberg: *Spectral accuracy in fast Ewald-based methods for particle simulations.* J. Comput. Phys., 230:8744 – 8761, 2011.

[35] D. Lindbo and A.K. Tornberg: *Fast and spectrally accurate Ewald summation for 2-periodic electrostatic systems.* J. Chem. Phys., 136:164111, 2012.

[36] P. Minary, J.A. Morrone, D.A. Yarne, M.E. Tuckerman, and G.J. Martyna: *Long range interactions on wires: a reciprocal space based formalism.* J. Chem. Phys., 121:11949 – 11956., 2004.

[37] P. Minary, M.E. Tuckerman, K.A. Pihakari, and G.J. Martyna: *A new reciprocal space based treatment of long range interactions on surfaces.* J. Chem. Phys., 116:5351 – 5362, 2002.

[38] F. Nestler: *Approximationsverfahren zur schnellen Energieberechnung in Partikelsystemen.* Diplomarbeit, Fakultät für Mathematik, Technische Universität Chemnitz, 2012.

[39] F. Nestler and D. Potts: *Fast Ewald summation under 2d- and 1d-periodic boundary conditions based on NFFTs.* Proceedings of the 10th International Conference on Sampling Theory and Applications, 2013.

[40] M. Pippig: *PFFT - An extension of FFTW to massively parallel architectures.* SIAM J. Sci. Comput., 35:C213 – C236, 2013.

[41] M. Pippig and D. Potts: *Particle simulation based on nonequispaced fast Fourier transforms.* In G. Sutmann, P. Gibbon, and T. Lippert (eds.): *Fast Methods for Long-Range Interactions in Complex Systems*, IAS-Series, pp. 131 – 158, Jülich, 2011. Forschungszentrum Jülich.

[42] M. Pippig and D. Potts: *Parallel three-dimensional nonequispaced fast Fourier transforms and their application to particle simulation.* SIAM J. Sci. Comput., 35:C411 – C437, 2013.

[43] M. Porto: *Ewald summation of electrostatic interactions of systems with finite extent in two of three dimensions.* J. Phys. A, 33:6211 – 6218, 2000.

[44] D. Potts and G. Steidl: *Fast summation at nonequispaced knots by NFFTs.* SIAM J. Sci. Comput., 24:2013 – 2037, 2003.

[45] D. Potts, G. Steidl, and A. Nieslony: *Fast convolution with radial kernels at nonequispaced knots.* Numer. Math., 98:329 – 351, 2004.

[46] D. Potts, G. Steidl, and M. Tasche: *Fast Fourier transforms for nonequispaced data: A tutorial.* In J.J. Benedetto and P.J.S.G. Ferreira (eds.): *Modern Sampling Theory: Mathematics and Applications*, pp. 247 – 270, Boston, MA, USA, 2001. Birkhäuser.

[47] R.M. Slevinsky and H. Safouhi: *A recursive algorithm for the G transformation and accurate computation of incomplete Bessel functions.* Appl. Numer. Math., 60:1411 – 1417, 2010.

[48] G. Steidl: *A note on fast Fourier transforms for nonequispaced grids.* Adv. Comput. Math., 9:337 – 353, 1998.

[49] M.E. Tuckerman, P. Minary, K. Pihakari, and G.J. Martyna: *A new reciprocal space based method for treating long range interactions in ab initio and force-field based calculations for surfaces, wires, and clusters.* In *Computational methods for macromolecules: challenges and applications (New York, 2000)*, vol. 24 of *Lect. Notes Comput. Sci. Eng.*, pp. 381 – 410. Springer, Berlin, 2002.

[50] A.F. Ware: *Fast approximate Fourier transforms for irregularly spaced data.* SIAM Rev., 40:838 – 856, 1998.

[51] A.H. Widmann and D.B. Adolf: *A comparison of Ewald summation techniques for planar surfaces.* Comput. Phys. Commun., 107:167 – 186, 1997.

[52] I.C. Yeh and M.L. Berkowitz: *Ewald summation for systems with slab geometry.* J. Chem. Phys., 111(7):3155 – 3162, 1999.